LBL-30487

Lawrence Berkeley Laboratory
UNIVERSITY OF CALIFORNIA

Physics Division

Mathematics Department

Three Dimensional Vortex Methods for the Analysis of Wave Propagation on Vortex Filaments

A. Qi
(Ph.D. Thesis)

March 1991

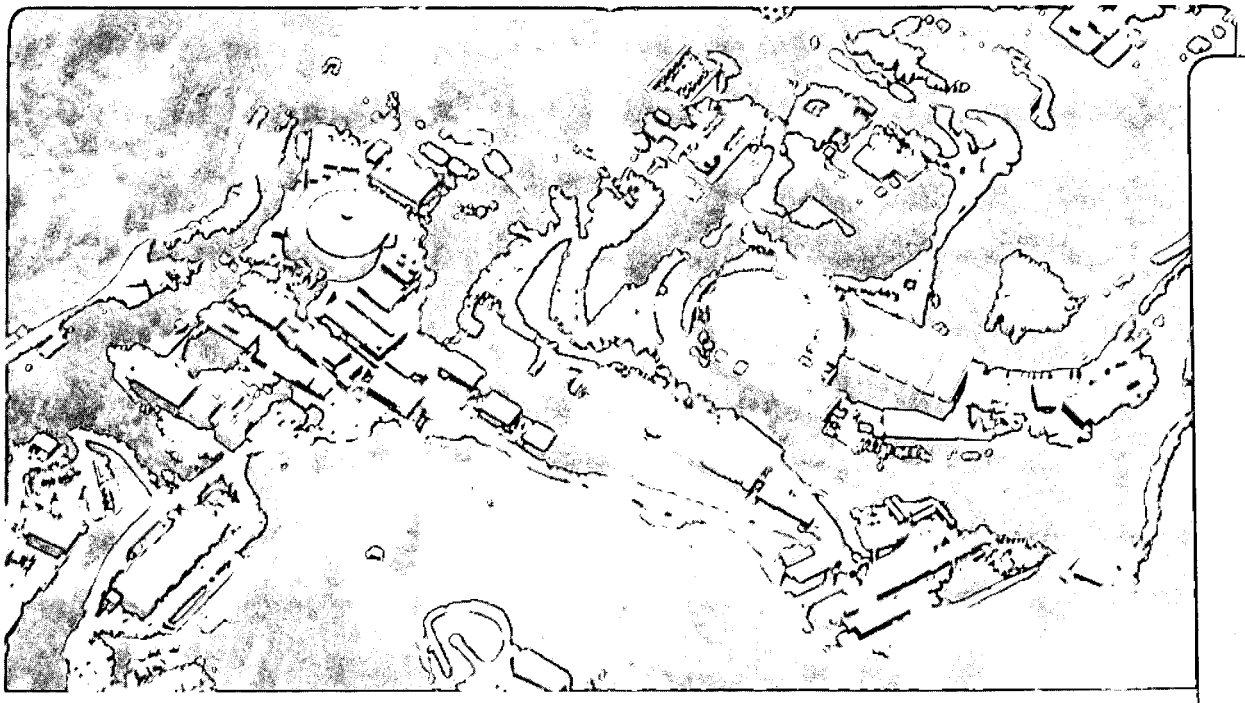

Prepared for the U.S. Department of Energy under Contract Number DE-AC03-76SF00098

DISCLAIMER

LBL-30487

THREE DIMENSIONAL VORTEX METHODS FOR THE ANALYSIS OF WAVE PROPAGATION ON VORTEX FILAMENTS*

Anmin Qi

Department of Mathematics
and
Lawrence Berkeley Laboratory
University of California
Berkeley, CA 94720

March 1991

Ph.D. Thesis

* This work was supported in part by the Applied Mathematical Sciences subprogram of the Office of Energy Research, U.S. Department of Energy, under contract DE-AC03-76SF-00098.

Acknowledgements

I would like to thank my advisor, Alexandre Chorin, for his encouragement, advice and care. Without his mathematical guidance and kind help, it would have been impossible for me to complete my graduate study at Berkeley.

I also wish to thank Ole Hald for his careful reading of the first draft and important suggestions for improvement of this thesis.

I would like to thank James Sethian for his reading of this thesis, and Stanley Berger for serving as the outside reader. I have benefited from conversation with Ding-Gwo Long.

I would like to acknowledge Paul Concus for assistance in using the computing facilities of the Lawrence Berkeley Laboratory of the University of California, and Ms. Valerie Heatlie for assistance in using facilities of the Lawrence Berkeley Laboratory of the University of California.

In addition, I wish to thank all of those at Berkeley who have helped me during the years of my graduate study.

Finally, I am grateful to my wife Lisa for her support, patience, understanding and caring. I wish her the best for her future doctoral work.

Contents

List of Figures

List of Tables

[21, 24, 29, 30, 31, 32, 33, 45, 46, 54, 63, 64, 65]. There are very well developed theoretical analyses by Hald & Del Prete [41], Hald [37, 38, 39, 40], Beale & Majda [7, 8, 9, 10], Beale [5, 6], Anderson & Greengard [1], Perlman [58], Goodman [34], Chang [14], and Roberts [60] for both two- and three-dimensional methods. In three-dimensional space, however, there are some difficulties in simulating the motion of vortex tubes by these methods due to lack of connectivity between blobs.

The three-dimensional vortex filament methods overcome the difficulties that appear in three-dimensional vortex blob methods. The essential idea, as described in Chorin [15, 16, 17], is to chop a vortex tube or filament into a finite number of segments that are short, thin, circular cylinders with their axes tangential at a point to the vorticity vector. We evaluate the velocity at both ends of a segment just as for a vortex blob in vortex blob methods. The connected segments remain connected. From Kelvin's circulation theorem and Stokes' theorem, the circulation around the filament remains constant in our computation. Several authors have employed this type of method to investigate various complex flows (see del Prete [28], Chorin [16, 17], Leonard [54, 55], Winckelmans [72], and Knio & Ghoniem [49]). There are also some theoretical analysis for this type of methods (Greengard [35]).

We try to understand vortex tube stretching from the study of wave propagation along a vortex tube by the self-induced velocity. Vortex filament methods are a proper numerical tool for this study. Therefore, we will focus our attention on vortex filament methods. The effects of numerical parameters, the choices of core functions, and numerical methods for solving the time evolution ordinary differential equation on accuracy and stability of the vortex filament methods are investigated in order to distinguish physical vortex stretching from the stretching caused by numerical instability. We also examine the conserved quantities such as kinetic energy, linear impulse, and total vorticity for various numerical parameters, core functions, and time integration methods.

A controllable single smooth initial wave datum is important for the study of wave propagation along a vortex tube. A solitary wave solution for Localized Induction Approximation (LIA) meets such a requirement. The so-called LIA was introduced to study a very thin vortex filament (see Arms & Hama [3], Hama [42, 43],

and Buttke [12]). In the study of LIA, Betchov [11] derived the so-called intrinsic equation and discovered the helicoid wave on a thin vortex filament by solving this equation. Later, Hasimoto [44] proved that the intrinsic equation can be reduced to a nonlinear Schrödinger equation and gave an analytic soliton solution for this equation. However, a vortex evolving according to the Betchov intrinsic equation does not stretch or contract [12] whereas study on three-dimensional vortex dynamics shows that vortex stretching is a common phenomenon. We like to know whether a solitary wave, with velocity induced by the Biot-Savart law, can propagate in a vortex tube for a long time without stretching. If there is a stretching in a vortex tube evolution, what causes the stretching?

Recently, Chorin [18, 20, 21, 22, 23] has studied vorticity/energy relations. His studies suggest that the folding of vortex lines or the development of hairpin structures in turbulent flow are required by energy conservation. To examine this idea it is critical to compute energy correctly. There are two parts in the computed energy: one is called the interaction energy, the other is called the self-energy. Chorin [18, 20, 21] computed the first part by a discretization of a formula due to Lamb [52]. The second part is computed by scaling laws developed by Chorin [18, 19, 20, 22, 23, 24]. We will examine these computations and use them to check our vortex method computation.

For convergence of numerical scheme and physical validity, we use several filaments to simulate part of a "fat" vortex tube. Some techniques to treat the truncated ends of a part of a vortex tube will be given in this thesis.

The thesis is organized as follows:

In Chapter 2, we review the physical background and the derivation of vortex filament methods. The details of the computational scheme are given.

In Chapter 3, we summarize results of the LIA study of a thin vortex filament. Derivations of the intrinsic equations and of Hasimoto's solution are reviewed. The equivalence of the Betchov intrinsic equation and the nonlinear Schrödinger equation is proved.

In Chapter 4, following Chorin's work [18, 19, 20, 21, 22, 23, 24], we study the conservation of energy and the scaling laws for self-energy. For constant core

function, we derive a new formula for computing self-energy. We also study certain properties of this new formula. The numerical schemes for other diagnostics, such as total vorticity and linear impulse, are given in this chapter.

In Chapter 5, we study the calculation on a part of a vortex tube. The treatments at truncated ends are given.

In Chapter 6, we present the numerical results with initial solitary wave data. We study the effects of the numerical methods for solving the time evolution ordinary differential equation, the core functions, core size, the time tolerance control constant, number of filaments used to simulate a vortex tube, the distance between filaments, the pattern of placement of filaments, and the circulation of each filament on the accuracy of computational results and on vortex stretching (both numerical and physical). We also study the effect of torsion of the initial solitary wave data on vortex stretching. We attempt to determine how vortex stretching starts and whether a solitary wave can propagate for a long time in a vortex tube with velocity induced by the Biot-Savart law. We will show that core size and torsion of perturbation wave are the two most sensitive factors in studying vortex stretching: a small torsion of wave will cause a discontinuity on the velocity component in the direction of the wave propagation. The long-time propagation of a wave of constant shape on a vortex tube will be discussed. Results suggest that the long-time propagation of a wave of constant shape on a vortex tube is possible.

Chapter 2

Physical Background and Numerical Schemes

2.1 Physical Background

We consider unbounded, incompressible, inviscid fluid flows. The motion of such flows is described by Euler's equations

$$\frac{D\mathbf{u}}{Dt} = \frac{\partial \mathbf{u}}{\partial t} + (\mathbf{u} \cdot \nabla)\mathbf{u} = -\nabla P \tag{2.1}$$

$$\nabla \cdot \mathbf{u} = 0 \tag{2.2}$$

where $\mathbf{u}(\mathbf{x}, t) = (u, v, w)$ is the velocity field, $\mathbf{x} = (x, y, z)$ is the position, t is time, $\nabla = (\partial/\partial x, \partial/\partial y, \partial/\partial z)$ is the gradient operator, and P is pressure. Conservation of mass and incompressibility give equation (2.2). Equations (2.1) express the conservation of momentum for inviscid fluid of constant density. (See Chorin & Marsden [27, p. 18] or Batchelor [4, p. 75] for details of the derivation of these equations.)

Define the vorticity $\boldsymbol{\omega}$ as the curl of velocity, i.e.

$$\boldsymbol{\omega} = \nabla \times \mathbf{u} \tag{2.3}$$

We can write equations (2.1) in terms of vorticity by taking the curl of equations (2.1),

$$\frac{\partial \boldsymbol{\omega}}{\partial t} + \nabla \times ((\mathbf{u} \cdot \nabla)\mathbf{u}) = 0 \tag{2.4}$$

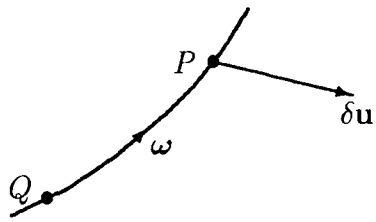

Figure 2.1. Portion of a vortex line.

Note that $\nabla \times \nabla P = 0$ for any scalar function P. The second term in the left side of equation (2.4) can be written as follows,

$$\nabla \times [(\mathbf{u} \cdot \nabla)\mathbf{u}] = (\mathbf{u} \cdot \nabla)\boldsymbol{\omega} - (\boldsymbol{\omega} \cdot \nabla)\mathbf{u} + (\nabla \cdot \mathbf{u})\boldsymbol{\omega} = (\mathbf{u} \cdot \nabla)\boldsymbol{\omega} - (\boldsymbol{\omega} \cdot \nabla)\mathbf{u} \qquad (2.5)$$

The last equality holds by equation (2.2). Substituting equation (2.5) into equation (2.4), we have the *vorticity transport equation*

$$\frac{\partial \boldsymbol{\omega}}{\partial t} + (\mathbf{u} \cdot \nabla)\boldsymbol{\omega} = (\boldsymbol{\omega} \cdot \nabla)\mathbf{u} \qquad (2.6)$$

where $(\mathbf{u} \cdot \nabla)\boldsymbol{\omega}$ is the convective term for fluid.

Comparing equations (2.6) with the evolution equations for a material line element $\delta\mathbf{l}$ given by Batchelor [4, p. 133]

$$\frac{\partial \delta\mathbf{l}}{\partial t} + (\mathbf{u} \cdot \nabla)\delta\mathbf{l} = (\delta\mathbf{l} \cdot \nabla)\mathbf{u} \qquad (2.7)$$

we see that vortex lines move as material lines, where a vortex line is defined as a line in the fluid whose tangent is everywhere parallel to the vorticity vector. In a fluid, a material line consists of the same fluid particles and move with them in a fluid. The term $(\boldsymbol{\omega} \cdot \nabla)\mathbf{u}$ corresponds to the changes in the vortex lines that come partly from rigid rotation of the line element due to the component of $\delta\mathbf{u}$ normal to $\boldsymbol{\omega}$ and partly from the stretching or the contraction of the line element due to the component of $\delta\mathbf{u}$ parallel to $\boldsymbol{\omega}$, where $\delta\mathbf{u}$ is the velocity of the fluid at a point Q relative to that at a neighboring point P, both Q and P being on the vortex line (see Figure 2.1). In

two-dimensional incompressible, inviscid flow, this term vanishes. Therefore, vortex lines in two-dimensional inviscid flow do not stretch.

For any well-defined integrable function $\theta(\mathbf{x}, t)$, we know

$$\frac{d}{dt}\int_Q^P \theta d\mathbf{l} = \int_Q^P \frac{D\theta}{Dt} d\mathbf{l} + \int_Q^P \theta(d\mathbf{l}\cdot\nabla)\mathbf{u} \tag{2.8}$$

where the integration is along a material curve from point P to Q. (See Batchelor [4, p. 133] for a detailed derivation of equation (2.8).)

Vortex lines through every point of a given closed curve C_t, where t represents the curve moving with the fluid, form a tube called a vortex tube. We define the circulation of a vortex tube as

$$\Gamma = \oint_{C_t} \mathbf{u}\cdot d\mathbf{l} \tag{2.9}$$

Take the derivative of Γ with respect to time,

$$\begin{aligned}\frac{d}{dt}\Gamma &= \frac{d}{dt}\oint_{C_t}\mathbf{u}\cdot d\mathbf{l}\\ &= \oint_{C_t}(\frac{D\mathbf{u}}{Dt})\cdot d\mathbf{l} + \oint_{C_t}\mathbf{u}\cdot((d\mathbf{l}\cdot\nabla)\mathbf{u})\\ &= -\oint_{C_t}\nabla P\cdot d\mathbf{l} + \oint_{C_t}\mathbf{F}\cdot d\mathbf{l}\end{aligned} \tag{2.10}$$

where

$$\mathbf{F} = \begin{pmatrix}\mathbf{u}\cdot\partial_x\mathbf{u}\\ \mathbf{u}\cdot\partial_y\mathbf{u}\\ \mathbf{u}\cdot\partial_z\mathbf{u}\end{pmatrix}$$

A simple computation shows that $\mathbf{F}$ is curl free; i.e.,

$$\nabla\times\mathbf{F} = 0$$

Therefore, by Stokes' theorem we have

$$\frac{d}{dt}\Gamma = 0 \tag{2.11}$$

i.e., the circulation of a vortex tube of inviscid flow is constant in time. This is the well-known Kelvin circulation theorem [47].

By Stokes' theorem, the circulation can be written as

$$\Gamma = \int_{S_t} \boldsymbol{\omega} \cdot d\mathbf{A} \tag{2.12}$$

where $d\mathbf{A} = \mathbf{n}\mathrm{dA}$ is an element of the open surface S_t bounded by the closed curve C_t.

Consider a piece of vortex tube with two end cross-section faces S_1 and S_2 and the surface of the tube S_t. Denote the boundaries of S_1 and S_2 as C_1 and C_2, respectively. Let W_t be the region of this piece of tube with boundary $\Sigma = S_1 \cup S_2 \cup S_t$. By Gauss' theorem and the fact $\nabla \cdot \boldsymbol{\omega} = 0$,

$$0 = \int_{W_t} \nabla \cdot \boldsymbol{\omega} dV = \int_{\Sigma} \boldsymbol{\omega} \cdot d\mathbf{A} = \int_{S_1 \cup S_2} \boldsymbol{\omega} \cdot d\mathbf{A} + \int_{S_t} \boldsymbol{\omega} \cdot d\mathbf{A}$$

$$\int_{S_t} \boldsymbol{\omega} \cdot d\mathbf{A} = 0$$

since $\boldsymbol{\omega} \cdot \mathbf{n} = 0$.

Thus,

$$0 = \int_{S_1 \cup S_2} \boldsymbol{\omega} \cdot d\mathbf{A} = \int_{S_1} \boldsymbol{\omega} \cdot d\mathbf{A} + \int_{S_2} \boldsymbol{\omega} \cdot d\mathbf{A} = \int_{C_1} \mathbf{u} \cdot d\mathbf{s} - \int_{C_2} \mathbf{u} \cdot d\mathbf{s} \tag{2.13}$$

The last equality holds by Stokes' theorem and consideration of the normal directions of S_1 and S_2. Equation (2.13) shows that the circulation of a vortex tube is the same for any curve encircling the vortex tube that is the statement of Helmhotz' theorem (see Chorin & Marsden [27, p. 36]. We call the circulation of a vortex tube the strength of the tube.

From equations (2.2) and (2.3), we set

$$\mathbf{u} = \nabla \times \boldsymbol{\Psi} \tag{2.14}$$

where $\boldsymbol{\Psi}$ is called a vector potential to be determined. Thus

$$\boldsymbol{\omega} = \nabla \times \mathbf{u} = \nabla \times (\nabla \times \boldsymbol{\Psi}) = -\nabla^2 \boldsymbol{\Psi} + \nabla(\nabla \cdot \boldsymbol{\Psi}) \tag{2.15}$$

If we assume that $\boldsymbol{\Psi}$ is divergence free, i.e. $\nabla \cdot \boldsymbol{\Psi} = 0$, then

$$\boldsymbol{\omega} = -\nabla^2 \boldsymbol{\Psi} \tag{2.16}$$

The solution of equation (2.16) in terms of $\boldsymbol{\omega}$ is

$$\boldsymbol{\Psi}(\mathbf{x},t) = G * \boldsymbol{\omega} = \int G(\mathbf{x}-\mathbf{x}')\boldsymbol{\omega}(\mathbf{x}')d\mathbf{x}' \tag{2.17}$$

where the volume integral is taken over the region occupied by the fluid, $\mathbf{x}'$ is the position of the volume element $d\mathbf{x}'$, and $G(\mathbf{x}) = 1/(4\pi r)$ is the fundamental solution for the Laplace operator, where $r = |\mathbf{x}|$ and $*$ denotes convolution. One can easily check that the $\boldsymbol{\Psi}$ expressed by equation (2.17) is divergence free. Taking curl of $\boldsymbol{\Psi}$, we find

$$\mathbf{u} = \nabla \times \boldsymbol{\Psi} = \nabla \times (G * \boldsymbol{\omega}) = \int K(\mathbf{x}-\mathbf{x}') \times \boldsymbol{\omega}(\mathbf{x}')d\mathbf{x}' \tag{2.18}$$

where

$$K(\mathbf{x}) = \frac{\partial G}{\partial r}(|\mathbf{x}|)\frac{\mathbf{x}}{|\mathbf{x}|} = -\frac{1}{4\pi}\frac{\mathbf{x}}{r^3}$$

is known as a kernel. We write

$$\mathcal{K}(\mathbf{x}) = K(\mathbf{x})\times = -\frac{1}{4\pi r^3}\begin{pmatrix} 0 & -z & y \\ z & 0 & -x \\ -y & x & 0 \end{pmatrix}$$

then

$$\mathbf{u} = \mathcal{K} * \boldsymbol{\omega} \tag{2.19}$$

A singular filament C is a curve on which the vorticity is concentrated with zero vorticity elsewhere in the fluid. We denote its strength Γ—the circulation number. Let vector $\delta\mathbf{l}$ represent a material line element determined by the equation

$$\frac{d\delta\mathbf{l}}{dt} = \delta\mathbf{l} \cdot \nabla\mathbf{u} + o(|\delta\mathbf{l}|)$$

We have

$$\int_{\delta V} \boldsymbol{\omega} dV = \Gamma\ \delta\mathbf{l} \tag{2.20}$$

where δV is a nearly cylindrical piece of element on the filament curve with negligible cross-section diameter. Thus equation (2.18) becomes, at time t and position $\mathbf{x}$,

$$\mathbf{u}(\mathbf{x},t) = \Gamma \int_C K(\mathbf{x}-\mathbf{x}') \times d\mathbf{l}(\mathbf{x}') = -\frac{\Gamma}{4\pi}\int_C \frac{(\mathbf{x}-\mathbf{x}') \times d\mathbf{l}(\mathbf{x}')}{|\mathbf{x}-\mathbf{x}'|^3} \tag{2.21}$$

Equation (2.21) is the well-known Biot-Savart law. Notice that equation (2.21) diverges with rate $1/|\mathbf{x}-\mathbf{x}'|^2$ if $\mathbf{x}$ is a point on curve C (see Batchelor [4, p. 94]). Moreover, it will be shown in the next chapter that a singular filament with nonzero curvature has infinite self-induced velocity.

2.2 The Smoothed Kernel

The difficulties arising from equation (2.21) for a singular filament force us to find a way to smooth out the singularity in this equation. Following Beale & Majda [10] (who have followed an idea of Hald [37] for two-dimensional vortex methods), we replace the kernel $\mathcal{K}$ by $\mathcal{K}_\sigma = \mathcal{K} * \psi_\sigma$, $\psi_\sigma(\mathbf{x}) = \sigma^{-3}\,\psi(\frac{\mathbf{x}}{\sigma})$, where σ is a parameter to be chosen. We assume that ψ satisfies the conditions

(i) ψ is smooth and rapidly decreasing; i.e.,

$$|D^\beta \psi(\mathbf{x})| \le C_{\beta j}(1+|\mathbf{x}|^2)^{-j} \tag{2.22}$$

for every muti-index β and every integer j;

(ii)

$$\int \psi(\mathbf{x})\, d\mathbf{x} = 1 \tag{2.23}$$

(iii)

$$\int \mathbf{x}^\beta \psi(\mathbf{x})\, d\mathbf{x} = 0 \quad 1 \le |\beta| \le m-1 \tag{2.24}$$

m is an integer.

The functions ψ_σ are called core functions or cutoff functions; parameter σ is known as core size or cutoff size.

Condition (i) implies that the ψ and its Fourier transform are smooth and rapidly decreasing. Condition (iii) always holds for $\psi = \psi(r)$, $r = |\mathbf{x}|$ with m even.

Recall equation (2.18), and let $G_\sigma = G * \psi_\sigma$. Then

$$(\mathcal{K}_\sigma * \boldsymbol{\omega})(\mathbf{x}) = \int \frac{\partial G_\sigma}{\partial r}(|\mathbf{x}-\mathbf{x}'|)\frac{\mathbf{x}-\mathbf{x}'}{|\mathbf{x}-\mathbf{x}'|} \times \boldsymbol{\omega}(\mathbf{x}')d\mathbf{x}'$$

i.e.,

$$K_\sigma(\mathbf{x}) = \frac{\partial G_\sigma}{\partial r}(|\mathbf{x}|)\frac{\mathbf{x}}{|\mathbf{x}|} \tag{2.25}$$

To find a simple expression for K_σ, let us consider $\sigma = 1$ and assume

$$\frac{\partial G_1}{\partial r} = -\frac{f(r)}{4\pi r^2}$$

We try to find the relation between f and ψ. We expect

$$\frac{\partial G_1}{\partial r} \sim \frac{\partial G}{\partial r} = -\frac{1}{4\pi r^2}, \quad as \quad r \to \infty \tag{2.26}$$

Then

$$-\psi = \nabla^2 G_1 = r^{-2} D_r\{r^2 D_r G_1\} = -\frac{f'(r)}{4\pi r^2}$$

i.e.,

$$\psi = \frac{f'(r)}{4\pi r^2} \tag{2.27}$$

To have conditions (i)–(iii) hold for ψ, f must satisfy

(1) $f(r)/r^3$ is a smooth function of r^2

(2) $f(r) \to 1$ as $r \to \infty$

(3) $\int_0^\infty f'(r) r^{2k} dr = 0 \quad 2 \le 2k \le m-2$

(4) $|D^j f(r)| \le C_j r^{-l-j}, \quad r \ge 1$, for each $j \ge 1$ and a fixed $l \ge m+1$

Choosing f that satisfies the above requirements, we get

$$\frac{\partial G_\sigma}{\partial r} = -\frac{f(r/\sigma)}{4\pi r^2} \tag{2.28}$$

Therefore,

$$K_\sigma(\mathbf{x}) = -\frac{1}{4\pi r^3} f(r/\sigma)\mathbf{x} \tag{2.29}$$

There are some explicit expressions for f and ψ:

$$\begin{aligned}
&for\ m=2, \quad f(r) = 1 - e^{-r^3} && \psi(r) = \tfrac{3}{4\pi} e^{-r^3} \\
&\qquad\qquad f(r) = \tanh r^3 && \psi(r) = \tfrac{3}{4\pi} \mathrm{sech}^2 r^3 \\
&for\ m=4, \quad f_4(r) = f(r) + \tfrac{1}{2} r f'(r) && \psi^{(4)} = \tfrac{1}{8\pi r^2}[3f'(r) + r f''(r)]
\end{aligned}$$

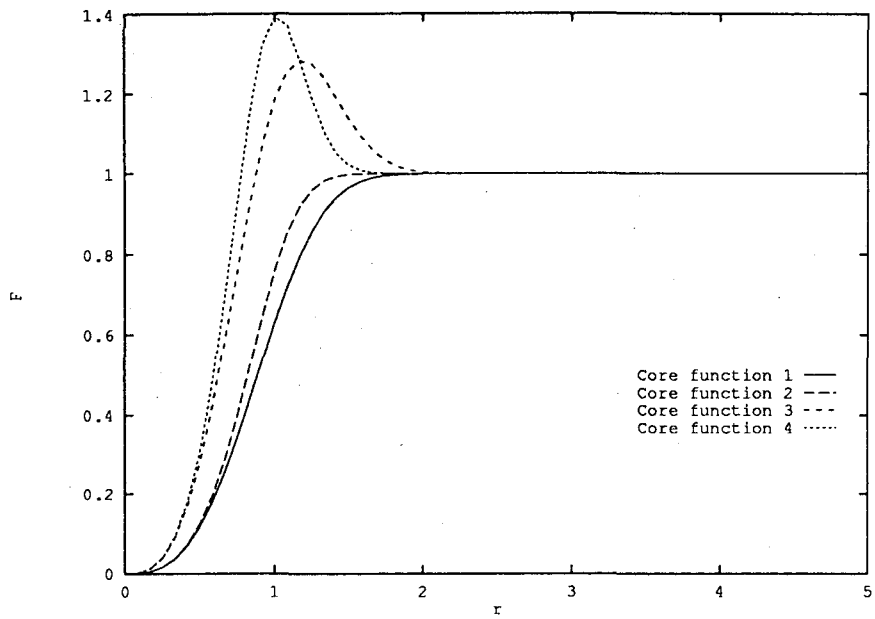

Figure 2.2. Four core functions.

where $f(r)$ is a function with $m = 2$. (See Beale & Majda [10].) We plot the following four core functions in Figure 2.2:

Core function 1 for $1 - e^{-r^3}$
Core function 2 for $\tanh r^3$
Core function 3 for $1 + (-1 + \frac{3}{2}r^3)e^{-r^3}$
Core function 4 for $\tanh r^3 + \frac{3}{2}r^3 \mathrm{sech}^2 r^3$

Replace K with K_σ in equation (2.21). We find

$$\mathbf{u}_\sigma(\mathbf{x},t) = \Gamma \int_C K_\sigma(\mathbf{x}-\mathbf{x}') \times d\mathbf{l}(\mathbf{x}') = -\frac{\Gamma}{4\pi}\int_C f(\frac{|\mathbf{x}-\mathbf{x}'|}{\sigma})\frac{(\mathbf{x}-\mathbf{x}')\times d\mathbf{l}(\mathbf{x}')}{|\mathbf{x}-\mathbf{x}'|^3} \quad (2.30)$$

Let us try to get equation (2.30) from

$$\mathbf{u}_\sigma = \mathcal{K}_\sigma * \boldsymbol{\omega}$$

By the property of convolution,

$$\mathcal{K}_\sigma * \boldsymbol{\omega} = (\mathcal{K} * \psi_\sigma) * \boldsymbol{\omega} = \mathcal{K} * (\psi_\sigma * \boldsymbol{\omega}) = \mathcal{K} * \boldsymbol{\omega}_\sigma \quad (2.31)$$

where

$$\omega_\sigma = \psi_\sigma * \omega = \int_{R^3} \psi_\sigma(\mathbf{x} - \mathbf{x}')\omega(\mathbf{x}')d\mathbf{x}' \tag{2.32}$$

Note that we must perform this operation with caution since not all conditions required in the distribution theory (see, e.g., Rudin [61]) hold here. Nevertheless, this operation is valid here subject to a nonregular approach of proof (see Hald [40]), which is not a topic of this thesis. Thus, the cross section of the filament with vorticity ω_σ does not vanish, and the radius of the cross section is determined by σ. Remember that

$$\psi_\sigma(\mathbf{x}) \to \delta(\mathbf{x}) \quad as\ \sigma \to 0$$

where the scalar function $\delta(\mathbf{x})$ is the so-called Dirac-function. We can write

$$\omega(\mathbf{x}) = \int_{R^3} \delta(\mathbf{x} - \mathbf{x}')\omega(\mathbf{x}')d\mathbf{x}' \tag{2.33}$$

for a singular filament.

By Helmholtz' theorem, the direction and the magnitude of ω in a material element with volume δV change with time in the same way as the direction and magnitude of the vector $\delta\mathbf{l}$ representing a material line element that at $t = 0$ was chosen to be parallel to the local vorticity; i.e.,

$$\frac{\omega(t)}{|\omega(0)|} = \frac{\delta\mathbf{l}(t)}{|\delta\mathbf{l}(0)|}$$

Recall equation (2.20), $\omega(0)\delta V \approx \Gamma\delta\mathbf{l}(0)$. Therefore,

$$\begin{aligned} \mathbf{u}_\sigma(t) &= \mathcal{K}_\sigma(t) * \omega(t) = \int K_\sigma(\mathbf{x}(t) - \mathbf{x}'(t)) \times \omega(\mathbf{x}'(t))d\mathbf{x}'(t) \\ &= \Gamma \int_C K_\sigma(\mathbf{x}(t) - \mathbf{x}'(t)) \times d\mathbf{l}(t) \end{aligned} \tag{2.34}$$

This is equation (2.30). As we can see, this approach gives some indication of physical meaning of ψ_σ and σ.

Now we can start to construct our numerical scheme.

2.3 Vortex Filament Methods

Let us consider first the evolution of an isolated thin tube of vorticity, or vortex filament with strength Γ. We divide this filament into small pieces or segments.

For the jth segment, the two ends are points $\mathbf{x}_j$ and $\mathbf{x}_{j+1}$. Let $\delta\mathbf{l}_j = \mathbf{x}_{j+1} - \mathbf{x}_j$ denote a vector element of length of jth vortex segment that lies in the volume element δV_j. Thus equation (2.30) can be written as

$$\mathbf{u}_\sigma(\mathbf{x},t) = -\frac{\Gamma}{4\pi}\sum_{j=1}^{\infty}\int_{\delta\mathbf{l}_j}\frac{(\mathbf{x}-\mathbf{x}')\times d\mathbf{l}(\mathbf{x}')}{|\mathbf{x}-\mathbf{x}'|^3}f(\frac{|\mathbf{x}-\mathbf{x}'|}{\sigma}) \tag{2.35}$$

Notice that we can only carry out computation for the filament with finite length in reality. This is no problem for the periodic case, but one must be careful for the nonperiodic situation.

We require $|\delta\mathbf{l}_j| \leq h$ for all j where h is a predetermined small number. Thus

$$\int_{\delta\mathbf{l}_j}\frac{(\mathbf{x}-\mathbf{x}')\times d\mathbf{l}(\mathbf{x}')}{|\mathbf{x}-\mathbf{x}'|^3}f(\frac{|\mathbf{x}-\mathbf{x}'|}{\sigma}) \approx \frac{\mathbf{r}_j\times\delta\mathbf{l}_j}{r_j^3}f(\frac{r_j}{\sigma}) \tag{2.36}$$

where

$$\begin{aligned}\mathbf{r}_j &= \mathbf{x} - \tfrac{1}{2}(\mathbf{x}_{j+1}+\mathbf{x}_j)\\ r_j &= |\mathbf{r}_j|\end{aligned}$$

Insert equation (2.36) into equation (2.35),

$$\mathbf{u}_\sigma(\mathbf{x},t) = -\frac{\Gamma}{4\pi}\sum_{j=1}^{N}\frac{\mathbf{r}_j\times\delta\mathbf{l}_j}{r_j^3}f(\frac{r_j}{\sigma}) \tag{2.37}$$

Knowing $\mathbf{u}_\sigma$, solving the ordinary differential equations

$$\frac{d\mathbf{x}}{dt} = \mathbf{u}_\sigma(\mathbf{x},t) \tag{2.38}$$

we can determine the position for $\mathbf{x}_j$ at the next time step $t+\Delta t$. There are various numerical methods for solving equation (2.38), we have used the first-order Euler's method, the second-order Heun's method, and the fourth-order Runge-Kutta method in our study. The algorithms are

Euler's method

$$\mathbf{x}_i(t+\Delta t) = \mathbf{x}_i(t) + \Delta t\mathbf{u}_\sigma(\mathbf{x}_i,t)$$

Modified trapezoidal method (or second-order Heun's method)

$$\begin{aligned}\mathbf{x}_i^* &= \mathbf{x}_i(t) + \Delta t\mathbf{u}_\sigma(\mathbf{x}_i,t)\\ \mathbf{x}_i(t+\Delta t) &= \mathbf{x}_i(t) + \tfrac{1}{2}\Delta t(\mathbf{u}_\sigma(\mathbf{x}_i,t) + \mathbf{u}(\mathbf{x}_i^*,t))\end{aligned}$$

Fourth-order Runge-Kutta method

$$\begin{aligned}
\mathbf{x}_i^{(1)} &= \mathbf{x}_i(t) + \tfrac{\Delta t}{2}\mathbf{u}_\sigma(\mathbf{x}_i, t) \\
\mathbf{x}_i^{(2)} &= \mathbf{x}_i(t) + \tfrac{\Delta t}{2}\mathbf{u}_\sigma(\mathbf{x}_i^{(1)}, t + \tfrac{\Delta t}{2}) \\
\mathbf{x}_i^{(3)} &= \mathbf{x}_i(t) + \Delta t\mathbf{u}_\sigma(\mathbf{x}_i^{(2)}, t + \tfrac{\Delta t}{2}) \\
\mathbf{x}_i(t+\Delta t) &= \mathbf{x}_i(t) + \tfrac{\Delta t}{6}[\mathbf{u}_\sigma(\mathbf{x}_i, t) + 2\mathbf{u}_\sigma(\mathbf{x}_i^{(1)}, t + \tfrac{\Delta t}{2}) \\
&\qquad + 2\mathbf{u}_\sigma(\mathbf{x}_i^{(2)}, t + \tfrac{\Delta t}{2}) + \mathbf{u}_\sigma(\mathbf{x}_i^{(3)}, t + \Delta t)]
\end{aligned}$$

As we mentioned on page 6 in Section 2.1, the filament stretches as the flow evolves; thus $\delta\mathbf{l}_j$ and the amount of vorticity carried by this vortex element grow. If $|\delta\mathbf{l}_j| > h$, we split this segment into two from the middle of $\delta\mathbf{l}_j$ with length $|\delta\mathbf{l}_j|/2$ to maintain the partition fine enough for accurate computation.

We also need to control our time step Δt since velocity $\mathbf{u}_\sigma$ could change dramatically for the change of curvature, as explained in Section 2.1. The requirement for the choice of Δt at step n is given by

$$\Delta t \max_j |\mathbf{u}_j^n| \leq C \tag{2.39}$$

where C is a given constant, $\mathbf{u}_j^n = \mathbf{u}_\sigma(\mathbf{x}_j(t^n), t^n)$, and t^n is the time at step n.

From the consideration of accuracy of the scheme, we require $\sigma = h^q$, $0 < q < 1$, or simply $\sigma/h > 1$ (see Beale & Majda [8, 9], Anderson & Greengard [1], and Greengard [35]).

For the scheme given above, we take the cutoff parameter σ as constant for the whole filament. It is also possible to have $\sigma = \sigma(s,t)$; i.e., we can choose σ_j for the jth segment and let each σ_j vary to conserve volume of the corresponding segment. I.e.,

$$\sigma_j^2(t+\Delta t)|\delta\mathbf{l}_j(t+\Delta t)| = \sigma_j^2(t)|\delta\mathbf{l}_j(t)| \tag{2.40}$$

We can also attempt to conserve volume by varying σ at each time step such that

$$\sigma^2(t+\Delta t)\sum_j |\delta\mathbf{l}_j(t+\Delta t)| = \sigma^2(t)\sum_j |\delta\mathbf{l}_j(t)| \tag{2.41}$$

From equation (2.33), the vorticity distribution for a singular filament can be written as

$$\omega(\mathbf{x}, t) = \sum_j \int_{\delta V_j} \delta(\mathbf{x} - \mathbf{x}'(t))\omega(\mathbf{x}'(t))d\mathbf{x}'(t) \tag{2.42}$$

and the vorticity distribution for the corresponding nonsigular thin filament is

$$\begin{aligned}\boldsymbol{\omega}_\sigma(\mathbf{x},t) &= \sum_j \int_{\delta V_j} \psi_\sigma(\mathbf{x}-\mathbf{x}'(t))\boldsymbol{\omega}(\mathbf{x}'(t))d\mathbf{x}'(t) \\ &= \Gamma \sum_j \int_{\delta \mathbf{l}_j} \psi_\sigma(\mathbf{x}-\mathbf{x}'(t))d\mathbf{l}(t) \\ &\approx \Gamma \sum_j \psi_\sigma(\mathbf{r}_j(t))\delta\mathbf{l}_j(t) \end{aligned} \tag{2.43}$$

This is approximately equal to the velocity field described by equation (2.37).

From equation (2.43),

$$\boldsymbol{\omega}_\sigma(\mathbf{x},0) = \Gamma \sum_j \psi_\sigma(\mathbf{r}_j(0))\delta\mathbf{l}_j(0) \tag{2.44}$$

Thus the initial value needed to start our computation is given as the initial vorticity distribution.

So far, we have completed the description of algorithms of the vortex filament methods for an isolated thin filament. In real flow, we must use several filaments to simulate a thick vortex tube. The first reason is that ψ_σ is an approximation of the Dirac-function, and the approximation will be inaccurate if we take σ too large. Secondly, the cross section of a numerical filament is always a disc, whereas this is not true in real flow. The cross section of a real vortex filament or tube should be deformed as the flow evolves, and the deformation may be seen by using several filaments to simulate a vortex tube. (See Widnall [69], Widnall *et al.* [70], Widnall & Tsai [71], and Knio & Ghoniem [49].)

For several filaments, e.g. M filaments, we can modify equation (2.34) as follows:

$$\mathbf{u}_\sigma(\mathbf{x},t) = \sum_{m=1}^{M} \Gamma^{(m)} \int_{C_m} K_{\sigma_m}(\mathbf{x}(t)-\mathbf{x}'(t)) \times d\mathbf{l}(t) \tag{2.45}$$

Notice that for different numbers of filaments, the circulation and core size may be chosen to be different. Equation (2.37) can be modified as follows:

$$\mathbf{u}_\sigma(\mathbf{x},t) = -\frac{1}{4\pi} \sum_{m=1}^{M} \Gamma^{(m)} \sum_{j=1}^{\infty} \frac{\mathbf{r}_j^{(m)} \times \delta\mathbf{l}_j^{(m)}}{(r_j^{(m)})^3} f(\frac{r_j^{(m)}}{\sigma}) \tag{2.46}$$

where $\sigma = \sigma_m$ if $\mathbf{x}$ is not on any given filamnet and $\sigma = (\frac{\sigma_m^2+\sigma_l^2}{2})^{1/2}$ or $\sigma = (\sigma_m\sigma_l)^{1/2}$ if $\mathbf{x}$ is on the lth filament; σ_m may also be varied with time or with arclength and time to conserve volume.

Chapter 3

The Self-Induction Approximation

3.1 LIA and Betchov Equation

In this chapter, we follow Betchov [11], Hasimoto [44], and Buttke [12] to find the velocity induced by a filament itself near a point O on the filament. Parametrize the vortex line (filament) by arclength s; i.e., $\mathbf{r} = \mathbf{r}(s)$, and assume $s = 0$ at the point O. Take the derivative of $\mathbf{r}$,

$$\frac{d\mathbf{r}}{ds} = (\frac{dx}{ds}, \frac{dy}{ds}, \frac{dz}{ds}) = \mathbf{t}$$

where $\mathbf{t}$ is the unit tangent vector. Define the curvature κ of the filament by

$$\frac{d\mathbf{t}}{ds} = \kappa\mathbf{n}$$

i.e.,

$$\kappa = |\frac{d\mathbf{t}}{ds}|$$

where $\mathbf{n}$ is the unit normal vector. Define the unit binormal vector $\mathbf{b} = \mathbf{t} \times \mathbf{n}$. The unit vectors $\mathbf{t}, \mathbf{n}$, and $\mathbf{b}$ form an orthonormal coordinate system at all points along the curve $\mathbf{r}$(s). At $s = 0$, we denote these coordinate vectors as $\mathbf{t}_0 = \mathbf{t}(0)$, $\mathbf{n}_0 = \mathbf{n}(0)$, and $\mathbf{b}_0 = \mathbf{b}(0)$. Let $\mathbf{r}_0 = \mathbf{r}(0)$, for some small positive value L, $-L < s < L$,

$$\mathbf{r}(s) = \mathbf{r}(0) + s\frac{d\mathbf{r}}{ds}(0) + \frac{s^2}{2}\frac{d^2\mathbf{r}}{ds^2}(0) + \frac{s^3}{3!}\frac{d^3\mathbf{r}}{ds^3}(0) + O(s^4)$$

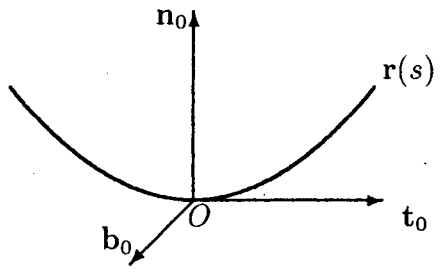

Figure 3.1. The curve $\mathbf{r}(s)$ near point O in Frenet-Serret coordinate system.

$$\begin{aligned} &= \mathbf{r}_0 + s\mathbf{t}_0 + \frac{s^2}{2}\mathbf{t}_0' + \frac{s^3}{3!}\mathbf{t}_0'' + O(s^4) \qquad (3.1) \\ &= \mathbf{r}_0 + s\mathbf{t}_0 + \frac{\kappa s^2}{2}\mathbf{n}_0 + \frac{s^3}{3!}\mathbf{t}_0'' + O(s^4) \end{aligned}$$

Thus a curve near O lies roughly on the $\mathbf{t}$-$\mathbf{n}$ plane, with no component along the binormal if we drop the terms with order equal to or higher than s^3 (see Figure 3.1). Similarly,

$$\mathbf{t}(s) = \mathbf{t}_0 + \kappa s\mathbf{n}_0 + \frac{s^2}{2}\mathbf{t}_0'' + O(s^3)$$

Pick a point $\mathbf{x}$ near O but off the curve $\mathbf{r}(s)$ to be $\mathbf{x} = y\mathbf{n}_0 + z\mathbf{b}_0$. Note that the variable $\mathbf{x}'$ in equation (2.21) is actually $\mathbf{r}$ here, and $d\mathbf{l}(\mathbf{x}') = \mathbf{t}(s)ds$; take the point O as origin in Cartesian coordinates, and, after dropping terms of order equal to or higher than s^3, we find

$$(\mathbf{x} - \mathbf{x}') \times \mathbf{t} \approx -y\mathbf{t}_0 + z\mathbf{n}_0 - z\kappa s\mathbf{t}_0 + \frac{ys^2}{2}(\mathbf{n}_0 \times \mathbf{t}_0'') + \frac{zs^2}{2}(\mathbf{b}_0 \times \mathbf{t}_0'') - \frac{\kappa s^2}{2}\mathbf{b}_0$$

$$|\mathbf{x} - \mathbf{x}'|^2 \approx y^2 + z^2 + s^2(1 - y\kappa) = \varrho^2 + s^2(1 - y\kappa)$$

where $\varrho^2 = y^2 + z^2$. Let $y = \varrho\, cos\phi$ and $z = \varrho\, sin\phi$; then the integrand of equation (2.21) can be written approximately as

$$\frac{(\mathbf{b}_0 cos\phi - \mathbf{n}_0 sin\phi)\varrho^{-1} + \mathbf{t}_0\kappa\zeta sin\phi + \mathbf{b}_0\frac{\kappa\zeta^2}{2} - \frac{\varrho\zeta^2}{2}[(\mathbf{n}_0 \times \mathbf{t}_0'')cos\phi + (\mathbf{b}_0 \times \mathbf{t}_0'')sin\phi]}{[1 + \zeta^2(1 - \varrho\kappa cos\phi)]^{\frac{3}{2}}}$$

where $\zeta = s/\varrho$. As $\varrho \to 0$,

$$\frac{\varrho\zeta^2}{2}[(\mathbf{n}_0 \times \mathbf{t}_0'')cos\phi + (\mathbf{b}_0 \times \mathbf{t}_0'')sin\phi] \to 0$$

$$1 + \zeta^2(1 - \varrho\kappa cos\phi) \approx 1 + \zeta^2$$

Because $\frac{\zeta}{(1+\zeta^2)^{\frac{3}{2}}}$ is an odd function

$$\int_{-L/\varrho}^{L/\varrho} \frac{\zeta}{(1+\zeta^2)^{\frac{3}{2}}} d\zeta = 0$$

We ignore the contribution to the velocity at O arising from parts of the filament outside the range $|s| < L$ since this part of velocity is bounded in magnitude. Then

$$\begin{aligned} \mathbf{u}(\mathbf{x},t) &\approx \frac{\Gamma}{4\pi}\int_{-L/\varrho}^{L/\varrho} \frac{(\mathbf{b}_0\cos\phi - \mathbf{n}_0\sin\phi)\varrho^{-1} + \mathbf{b}_0\frac{\kappa\zeta^2}{2}}{(1+\zeta^2)^{\frac{3}{2}}} d\zeta \\ &\sim \frac{\Gamma}{2\pi\varrho}(\mathbf{b}_0\cos\phi - \mathbf{n}_0\sin\phi) + \mathbf{b}_0\frac{\Gamma\kappa}{4\pi}\ln\frac{L}{\varrho} + O(1) \end{aligned} \tag{3.2}$$

for $\frac{L}{\varrho} \to \infty$.

The first term represents the circular motion around a straight filament, and the second term gives the velocity depending on curvature κ of the filament. After eliminating the first term, we have

$$\frac{\partial \mathbf{x}}{\partial t} = \mathbf{b}_0\frac{\Gamma\kappa}{4\pi}\ln\frac{L}{\varrho} \tag{3.3}$$

This is called the self-induction approximation or localized induction approximation (LIA). For nonzero curvature,

$$\frac{\partial \mathbf{x}}{\partial t} \to \infty, \quad as \ \frac{L}{\varrho} \to \infty$$

If we consider $\frac{\Gamma}{4\pi}\log\frac{L}{\varrho}$ as a constant, we can write equation (3.3) as

$$\frac{\partial \mathbf{x}}{\partial t} = (\frac{\Gamma}{4\pi}\ln\frac{L}{\varrho})\mathbf{t}_0 \times \frac{d\mathbf{t}_0}{ds} \tag{3.4}$$

since $\kappa\mathbf{b}_0 = \mathbf{t}_0 \times (\kappa\mathbf{n}_0) = \mathbf{t}_0 \times \frac{d\mathbf{t}_0}{ds}$. Let $\hat{t} = t\frac{\Gamma}{4\pi}\log\frac{L}{\varrho}$. We find

$$\frac{\partial \mathbf{x}}{\partial \hat{t}} = \mathbf{t}_0 \times \frac{d\mathbf{t}_0}{ds} = \kappa\mathbf{b}_0$$

After dropping the "hat" and subscript, we get

$$\frac{\partial \mathbf{x}}{\partial t} = \mathbf{t} \times \frac{d\mathbf{t}}{ds} = \kappa\mathbf{b} \tag{3.5}$$

We designate $' \equiv \frac{\partial}{\partial s}$ and $\dot{} \equiv \frac{\partial}{\partial t}$. Thus equation(3.5) can be written as

$$\dot{\mathbf{x}} = \mathbf{t} \times \mathbf{t}' = \kappa \mathbf{b} \tag{3.6}$$

Since $\mathbf{x}' = \mathbf{t}$, and $\mathbf{x}'' = \mathbf{t}' = \kappa \mathbf{n}$, then

$$\mathbf{x}''' = \mathbf{t}'' = \kappa' \mathbf{n} + \kappa(\tau \mathbf{b} - \kappa \mathbf{t}) = -\kappa^2 \mathbf{t} + \kappa\tau \mathbf{b} + \kappa' \mathbf{n}$$

where τ is the torsion of the curve defined by

$$\tau = -\mathbf{b}' \cdot \mathbf{n} \tag{3.7}$$

Since $\mathbf{t} \cdot \mathbf{n} = 0$,

$$0 = \mathbf{t}' \cdot \mathbf{n} + \mathbf{t} \cdot \mathbf{n}' = \kappa + \mathbf{t} \cdot \mathbf{n}'$$

that is,

$$\mathbf{t} \cdot \mathbf{n}' = -\kappa$$

From $\mathbf{b} \cdot \mathbf{n} = 0$, we get

$$0 = \mathbf{b}' \cdot \mathbf{n} + \mathbf{b} \cdot \mathbf{n}' = -\tau + \mathbf{b} \cdot \mathbf{n}'$$

that is,

$$\mathbf{b} \cdot \mathbf{n}' = \tau$$

Therefore

$$\mathbf{n}' = < \mathbf{t} \cdot \mathbf{n}' > \mathbf{t} + < \mathbf{n} \cdot \mathbf{n}' > \mathbf{n} + < \mathbf{b} \cdot \mathbf{n}' > \mathbf{b} = -\kappa \mathbf{t} + \tau \mathbf{b} \tag{3.8}$$

where we use the fact that $\mathbf{n} \cdot \mathbf{n}' = 0$. From $\mathbf{t} \cdot \mathbf{b} = 0$, we find

$$0 = \mathbf{t}' \cdot \mathbf{b} + \mathbf{t} \cdot \mathbf{b}' = \kappa \mathbf{n} \cdot \mathbf{b} + \mathbf{t} \cdot \mathbf{b}' = \mathbf{t} \cdot \mathbf{b}'$$

With $-\tau = \mathbf{n} \cdot \mathbf{b}'$, and remembering that $\mathbf{b} \cdot \mathbf{b}' = 0$, we get

$$\mathbf{b}' = -\tau \mathbf{n} \tag{3.9}$$

We have the well-known Serret-Frenet equations, which consist of equations (3.8) and (3.9) and

$$\mathbf{t}' = \kappa \mathbf{n} \tag{3.10}$$

If we take the derivative with respect to s for equation (3.6),

$$\dot{\mathbf{t}} = (\dot{\mathbf{x}})' = \kappa'\mathbf{b} + \kappa\mathbf{b}' = \kappa'\mathbf{b} - \kappa\tau\mathbf{n}$$

By the definition of κ,

$$\kappa^2 = \mathbf{t}' \cdot \mathbf{t}'$$

Thus,

$$\begin{aligned}
\frac{\partial \kappa^2}{\partial t} &= 2\mathbf{t}' \cdot \dot{\mathbf{t}}' = 2\mathbf{t}' \cdot (\kappa'\mathbf{b} - \kappa\tau\mathbf{n})' \\
&= 2\mathbf{t}' \cdot (\kappa''\mathbf{b} + \kappa'\mathbf{b}' - \kappa'\tau\mathbf{n} - \kappa\tau'\mathbf{n} - \kappa\tau\mathbf{n}') \\
&= 2\kappa\mathbf{n} \cdot [\kappa''\mathbf{b} - \kappa'\tau\mathbf{n} - \kappa'\tau\mathbf{n} - \kappa\tau'\mathbf{n} - \kappa\tau(\tau\mathbf{b} - \kappa\mathbf{t})] \\
&= 2\kappa(-2\kappa'\tau - \kappa\tau') \\
&= -2(\kappa^2)'\tau - 2\kappa^2\tau' \\
&= -2\frac{\partial(\kappa^2\tau)}{\partial s}
\end{aligned}$$

that is,

$$\frac{\partial \kappa^2}{\partial t} = -2\frac{\partial(\kappa^2\tau)}{\partial s} \tag{3.11}$$

or

$$\frac{\partial \kappa}{\partial t} = -2\kappa'\tau - \kappa\tau' \tag{3.12}$$

Equation (3.11) is *the first intrinsic equation*, derived first by Betchov [11].

Now let us derive *the second intrinsic equation*, also due to Betchov. Start from the formula $\kappa^2\tau = \mathbf{t} \cdot (\mathbf{t}' \times \mathbf{t}'')$. Thus,

$$\frac{\partial \kappa^2\tau}{\partial t} = \dot{\mathbf{t}} \cdot (\mathbf{t}' \times \mathbf{t}'') + \mathbf{t} \cdot (\dot{\mathbf{t}}' \times \mathbf{t}'') + \mathbf{t} \cdot (\mathbf{t}' \times \dot{\mathbf{t}}'')$$

Considering

$$\begin{aligned}
\dot{\mathbf{t}} &= \kappa'\mathbf{b} - \kappa\tau\mathbf{n} \\
\dot{\mathbf{t}}' &= \kappa^2\tau\mathbf{t} - (2\kappa'\tau + \kappa\tau')\mathbf{n} + (\kappa'' - \kappa\tau^2)\mathbf{b} \\
\dot{\mathbf{t}}'' &= (4\kappa'\kappa\tau + 2\kappa^2\tau')\mathbf{t} + (\kappa^3\tau + \kappa\tau^3 - 3\kappa''\tau - 3\kappa'\tau' - \kappa\tau'')\mathbf{n} + (\kappa''' - 3\kappa'\tau^2 - 3\kappa\tau\tau')\mathbf{b}
\end{aligned}$$

we find

$$\begin{aligned}
\mathbf{t}' \times \mathbf{t}'' &= \kappa^2\tau\mathbf{t} + \kappa^3\mathbf{b} \\
\dot{\mathbf{t}}' \times \mathbf{t}'' &= -(\kappa\kappa'\tau^2 + \kappa^2\tau\tau' + \kappa'\kappa'')\mathbf{t} - \kappa^2\kappa''\mathbf{n} - (\kappa^2\kappa'\tau + \kappa^3\tau')\mathbf{b} \\
\mathbf{t}' \times \dot{\mathbf{t}}'' &= \kappa(\kappa''' - 3\kappa'\tau^2 - 3\kappa\tau\tau')\mathbf{t} - \kappa(4\kappa\kappa'\tau + 2\kappa^2\tau')\mathbf{b}
\end{aligned}$$

Thus

$$\begin{aligned}
\frac{\partial\kappa^2\tau}{\partial t} &= \kappa^3\kappa' - \kappa\kappa'\tau^2 - \kappa^2\tau\tau' - \kappa'\kappa'' + \kappa\kappa''' - 3\kappa\kappa'\tau^2 - 3\kappa^2\tau\tau' \\
&= \kappa\kappa''' - \kappa'\kappa'' + \kappa^3\kappa' - 4\kappa\kappa'\tau^2 - 4\kappa^2\tau\tau' \\
&= \frac{1}{2}(\kappa^2)''' + \frac{9}{4}(\kappa^4)' - 2[\kappa^4 + \kappa^2\tau^2 + (\kappa')^2]' \\
&= \frac{1}{2}(\kappa^2)''' - 2[-\frac{1}{8}\kappa^4 + \kappa^2\tau^2 + (\kappa')^2]' \\
&= \frac{1}{2}[(\kappa^2)'' + \frac{1}{2}\kappa^4 - 4\kappa^2\tau^2 - 4(\kappa')^2]' \\
&= [\kappa\kappa'' - (\kappa')^2 - 2\kappa^2\tau^2 + \frac{1}{4}\kappa^4]' \qquad (3.13)
\end{aligned}$$

On the other hand, using equation (3.11), we find

$$\begin{aligned}
\frac{\partial\kappa^2\tau}{\partial t} &= \frac{\partial\kappa^2}{\partial t}\tau + \kappa^2\frac{\partial\tau}{\partial t} \\
&= -2\frac{\partial\kappa^2\tau}{\partial s}\tau + \kappa^2\frac{\partial\tau}{\partial t} \\
&= -2((\kappa^2)'\tau + \kappa^2\tau')\tau + \kappa^2\frac{\partial\tau}{\partial t} \qquad (3.14)
\end{aligned}$$

If we combine equations (3.13) and (3.14)

$$-2((\kappa^2)'\tau + \kappa^2\tau')\tau + \kappa^2\frac{\partial\tau}{\partial t} = \frac{1}{2}[(\kappa^2)'' + \frac{1}{2}\kappa^4 - 4(\kappa')^2]' - 2((\kappa^2)'\tau^2 + 2\kappa^2\tau\tau')$$

that is,

$$\begin{aligned}
\kappa^2(2\tau\tau' + \frac{\partial\tau}{\partial t}) &= \frac{1}{2}[(\kappa^2)'' + \frac{1}{2}\kappa^4 - 4(\kappa')^2]' \\
&= \frac{1}{2}[(\kappa^2)''' + \frac{1}{2}(\kappa^4)' - 4((\kappa')^2)']
\end{aligned}$$

The second intrinsic equation is

$$2\tau\tau' + \frac{\partial\tau}{\partial t} = \frac{1}{2}[\frac{(\kappa^2)'''}{\kappa^2} + \frac{1}{2}\frac{(\kappa^4)'}{\kappa^2} - 4\frac{((\kappa')^2)'}{\kappa^2}] = \frac{\kappa'''}{\kappa} - \frac{\kappa'\kappa''}{\kappa^2} + \kappa\kappa' \qquad (3.15)$$

or

$$\frac{\partial \tau}{\partial t} = (\frac{\kappa''}{\kappa} - \tau^2 + \frac{1}{2}\kappa^2)' \tag{3.16}$$

Let us seek some special exact solutions for equations (3.16) and (3.12). We consider only the case where torsion τ = constant and assume $\kappa' \neq 0$ in this thesis. Thus equation (3.16) becomes

$$(\frac{2\kappa''}{\kappa} + \kappa^2)' = 0$$

Integrating this equation, we find

$$\frac{2\kappa''}{\kappa} + \kappa^2 = \frac{A}{2}$$

where A is an integral constant that may depend on t. It is equivalent to

$$4[(\kappa')^2]' + (\kappa^4)' - A(\kappa^2)' = 0$$

or

$$[4(\kappa')^2 + \kappa^4 - A\kappa^2]' = 0$$

Integrating the above equation again, we get

$$2(\kappa')^2 + \kappa^4 - A\kappa^2 = C$$

where C is a constant. It can be written as

$$\pm\frac{2\kappa'}{(C + A\kappa^2 - \kappa^4)^{1/2}} = 1$$

Integrating the positive branch, we find

$$s - f(t) = \int_{s_0}^{s} \frac{2\kappa' d\zeta}{(C + A\kappa^2 - \kappa^4)^{1/2}} = \int_{\kappa(s_0)}^{\kappa(s)} \frac{2dk}{(C + Ak^2 - k^4)^{1/2}}$$

Let us assume $C = 0$; then

$$s - f(t) = -\frac{2}{A^{1/2}} \ln \frac{A^{1/2} + \sqrt{A - \kappa^2}}{\kappa}$$

Let $\beta = \frac{A^{1/2}}{2}$; then

$$\kappa(s,t) = 2\beta \mathrm{sech}\{\beta[s - f(t)]\} \tag{3.17}$$

Taking the derivatives of equation (3.17), we find

$$\begin{aligned}\frac{\partial\kappa}{\partial t} &= -2\beta^2\dot{f}\tanh\{\beta[s-f(t)]\}\mathrm{sech}\{\beta[s-f(t)]\} \\ \frac{\partial\kappa}{\partial s} &= -2\beta^2\tanh\{\beta[s-f(t)]\}\mathrm{sech}\{\beta[s-f(t)]\}\end{aligned}$$

From equation (3.12) and τ = constant, we get

$$\frac{\partial\kappa}{\partial t} = -2\kappa'\tau$$

Thus,

$$\dot{f} = 2\tau$$

Integrating the above, we find

$$f(t) = 2\tau(t - t_0)$$

Let $t_0 = 0$ and $2\tau = c$. We finally get

$$\kappa(s,t) = 2\beta\mathrm{sech}[\beta(s-ct)] \tag{3.18}$$

We will see in the following section that the intrinsic equations (3.12) and (3.16) are equivalent to the nonlinear Schrödinger equation.

3.2 Nonlinear Schrödinger equation and Hasimoto Solitary Wave

Hasimoto [44, 1972] reduced the self-induction approximation [equation (3.5)] to the nonlinear Schrödinger equation

$$\frac{1}{i}\frac{\partial\psi}{\partial t} = \frac{\partial^2\psi}{\partial s^2} + \frac{1}{2}\psi(|\psi|^2 + A) \tag{3.19}$$

by the following transformation

$$\psi = \kappa\exp(i\int_0^s \tau d\zeta) \tag{3.20}$$

The detailed derivation can also been found in the book by Lamb [51].

In this section, we prove that the nonlinear Schrödinger equation is actually equivalent to the Betchov intrinsic equations.

To show this, we integrate the second intrinsic equation (3.16) with respect to s

$$\int_0^s \dot{\tau} d\zeta = \frac{\kappa''}{\kappa} - \tau^2 + \frac{1}{2}\kappa^2 + \frac{1}{2}A$$

where $A = A(t)$. We can write this equation as

$$\kappa \int_0^s \dot{\tau} d\zeta = \kappa'' - \kappa\tau^2 + \frac{1}{2}\kappa^3 + \frac{1}{2}\kappa A \tag{3.21}$$

With the help of the first intrinsic equation (3.12), we find

$$\dot{\kappa} + i\kappa \int_0^s \dot{\tau} d\zeta = -(2\kappa'\tau + \kappa\tau') + i(\kappa'' - \kappa\tau^2 + \frac{1}{2}\kappa^3 + \frac{1}{2}\kappa A)$$

or

$$\frac{1}{i}(\dot{\kappa} + i\kappa \int_0^s \dot{\tau} d\zeta) = i2\kappa'\tau + i\kappa\tau' + \kappa'' - \kappa\tau^2 + \frac{1}{2}\kappa^3 + \frac{1}{2}\kappa A \tag{3.22}$$

We multiply both sides of equation (3.22) by $\exp(i\int_0^s \tau d\zeta)$. Then

$$\begin{aligned}
\frac{1}{i}\frac{\partial}{\partial t}[\kappa \exp(i\int_0^s \tau d\zeta)] &= (\kappa'' + i\kappa\tau' + i\kappa'\tau)\exp(i\int_0^s \tau d\zeta) \\
&\quad +(\kappa' + i\kappa\tau)i\tau \exp(i\int_0^s \tau d\zeta) \\
&\quad +\frac{1}{2}(\kappa^2 + A)\kappa \exp(i\int_0^s \tau d\zeta) \\
&= \frac{\partial^2}{\partial s^2}[\kappa \exp(i\int_0^s \tau d\zeta)] \\
&\quad +\frac{1}{2}(\kappa^2 + A)\kappa \exp(i\int_0^s \tau d\zeta)
\end{aligned} \tag{3.23}$$

Using the transformation [equation (3.20)], we get the nonlinear Schrödinger equation (3.19). Note that every step is reversible. Thus the nonlinear Schrödinger equation is equivalent to the Betchov intrinsic equations.

To eliminate A from equation (3.19), let

$$\Psi = \Psi(s,t) = \psi(s,t)\exp[-\frac{i}{2}\int_0^t A(\zeta)d\zeta]$$

Then

$$\frac{1}{i}\frac{\partial \Psi}{\partial t} = \frac{\partial^2 \Psi}{\partial s^2} + \frac{1}{2}\Psi|\Psi|^2 \tag{3.24}$$

We want to determine the actual shape of the curve that has curvature given by equation (3.18) with constant torsion τ. This has been done by Hasimoto [44].

From equation (3.9),

$$\mathbf{b}'' = -\tau\mathbf{n}'$$

From equation (3.8),

$$\tau\mathbf{n}' = -\kappa\tau\mathbf{t} + \tau^2\mathbf{b}$$

Thus,

$$-\mathbf{b}'' = -\kappa\tau\mathbf{t} + \tau^2\mathbf{b}$$

that is,

$$\tau\mathbf{t} = \frac{1}{\kappa}(\mathbf{b}'' + \tau^2\mathbf{b})$$

Taking the derivative with respect to s, we find

$$\tau\mathbf{t}' = [\frac{1}{\kappa}(\mathbf{b}'' + \tau^2\mathbf{b})]'$$

By equation (3.10),

$$0 = \tau(\mathbf{t}' - \kappa\mathbf{n}) = [\frac{1}{\kappa}(\mathbf{b}'' + \tau^2\mathbf{b})]' + \kappa\mathbf{b}'$$

that is,

$$[\frac{1}{2\beta}\cosh\beta\xi(\mathbf{b}'' + \tau^2\mathbf{b})]' + 2\beta\,\mathrm{sech}\beta\xi\mathbf{b}' = 0 \tag{3.25}$$

where $\xi = s - ct$. Equation (3.25) can be written as

$$\frac{d^3\mathbf{b}}{d\eta^3} + \tanh\eta\frac{d^2\mathbf{b}}{d\eta^2} + (T^2 + 4\mathrm{sech}^2\eta)\frac{d\mathbf{b}}{d\eta} + T^2\tanh\eta\mathbf{b} = 0 \tag{3.26}$$

where $\eta = \beta\xi$ and $T = \tau/\beta$.

Define

$$\mathbf{B} = \frac{d\mathbf{b}}{d\eta} + \tanh\eta\mathbf{b} \tag{3.27}$$

We can transform equation (3.26) to

$$\frac{d^2\mathbf{B}}{d\eta^2} + (T^2 + 2\mathrm{sech}^2\eta)\mathbf{B} = 0 \tag{3.28}$$

which has the trivial solution $\mathbf{B} = 0$ and two linear independent solutions

$$\mathbf{B}_\pm = (\tanh\eta \mp iT)e^{\pm iT\eta}\mathbf{e}_\pm$$

where $\mathbf{e}_-$ and $\mathbf{e}_+$ are constant vectors. The corresponding solutions of equation (3.27) are

$$\mathbf{b}_0 = \mathbf{e}_0 \operatorname{sech}\eta \tag{3.29}$$

$$\mathbf{b}_\pm = \mathbf{e}_\pm (1 - T^2 \mp 2iT\tanh\eta) e^{\pm iT\eta} \tag{3.30}$$

where $\mathbf{e}_0$ is a constant vector.

To have real $\mathbf{b}$ with $|\mathbf{b}| = 1$ satisfying the condition that the filament parallel to the x-axis at infinity, we choose the linear combination of $\mathbf{b}_0$, $\mathbf{b}_+$, and $\mathbf{b}_-$ as

$$\begin{aligned}
\mathbf{b} &= \begin{pmatrix} 2\mu \\ 0 \\ 0 \end{pmatrix} \operatorname{sech}\eta + \mu \begin{pmatrix} 0 \\ \frac{i}{2} \\ \frac{1}{2} \end{pmatrix} (1 - T^2 - 2iT\tanh\eta)\, e^{i\Theta} \\
&\quad + \mu \begin{pmatrix} 0 \\ -\frac{i}{2} \\ \frac{1}{2} \end{pmatrix} (1 - T^2 + 2iT\tanh\eta)\, e^{i\Theta} \\
&= \begin{pmatrix} 2\,\mu \operatorname{sech}\eta \\ \mu[2T\tanh\eta\cos\Theta - (1 - T^2)\sin\Theta] \\ \mu[2T\tanh\eta\sin\Theta + (1 - T^2)\cos\Theta] \end{pmatrix}
\end{aligned} \tag{3.31}$$

where $\mu = \frac{1}{1+T^2}$ and $\Theta = T\eta + \sigma(t)$. The function $\sigma(t)$ is determined by equation (3.5). Use the Serret-Frenet equations (3.8) and (3.9) and $\mathbf{x}' = \mathbf{t}$,

$$\mathbf{n} = \begin{pmatrix} 2\mu\operatorname{sech}\eta\tanh\eta \\ -(1 - 2\mu\tanh^2\eta)\cos\Theta + 2\mu T\tanh\eta\sin\Theta \\ -(1 - 2\mu\tanh^2\eta)\sin\Theta - 2\mu T\tanh\eta\cos\Theta \end{pmatrix} \tag{3.32}$$

$$\mathbf{t} = \begin{pmatrix} 1 - 2\mu\operatorname{sech}^2\eta \\ -2\mu\operatorname{sech}\eta\,[\tanh\eta\cos\Theta + T\sin\Theta] \\ -2\mu\operatorname{sech}\eta\,[\tanh\eta\sin\Theta - T\cos\Theta] \end{pmatrix} \tag{3.33}$$

and

$$\mathbf{x} = \begin{pmatrix} s - 2\frac{\mu}{\beta}\tanh\eta \\ 2\frac{\mu}{\beta}\operatorname{sech}\eta\cos\Theta \\ 2\frac{\mu}{\beta}\operatorname{sech}\eta\sin\Theta \end{pmatrix} \tag{3.34}$$

If we substitute equations (3.18), (3.31), and (3.34) into equation (3.5), we get

$$\frac{d\sigma(t)}{dt} = \beta^2 - \tau^2 \tag{3.35}$$

Integrating equation (3.35) and defining $\sigma(0) = 0$, we find

$$\sigma(t) = (\beta^2 - \tau^2)t \tag{3.36}$$

There is a solitary wave moving along the curve given by equation (3.34). Figure 3.2 shows that the $|\nu|$ determines the amplitude of curvature κ and increasing $|\tau|$ will increase the speed of wave and decrease the amplitude of the wave. In a real-time scale, the soliton speed along the x-axis is $\frac{\nu\tau\Gamma}{2\pi}[\ln(\frac{2L}{\varrho}) - 1]$. For $\tau = 0$, the soliton speed on the x-axis should be zero, but the velocity components in both the y and z directions are not zero; thus the soliton shape changes with time such that the solitary wave oscillates along the x-direction (Figure 3.3).

3.3 Comments on the LIA

The localized-induction approximation ignores several important aspects of the dynamics of real concentrated vortices (see Aref & Flinchem [2] and Leibovich & Ma [53]).

First, vorticity stretching is absent in this approximation (see Buttke [12]). However, numerical simulation shows that stretching must happen for a thin filament in incompressible fluids. Several authors have made new asymptotic equations to capture the stretching phenomenon for the motion of a thin filament (see Aref & Flinchem [2], Klein & Majda [48], and Callegari & Ting [13]).

The second defect is that the deformation of the vortex core is not represented since we have assumed that the term $\frac{\Gamma}{4\pi}\ln\frac{L}{\varrho}$ is constant. Also, the values of L and ϱ can not be determined *a priori*, although the correct time scaling depends on these values for equation (3.3).

As we have said, this approximation is local. It totally ignores the interaction between filaments and between two portions of a filament approaching each other closely.

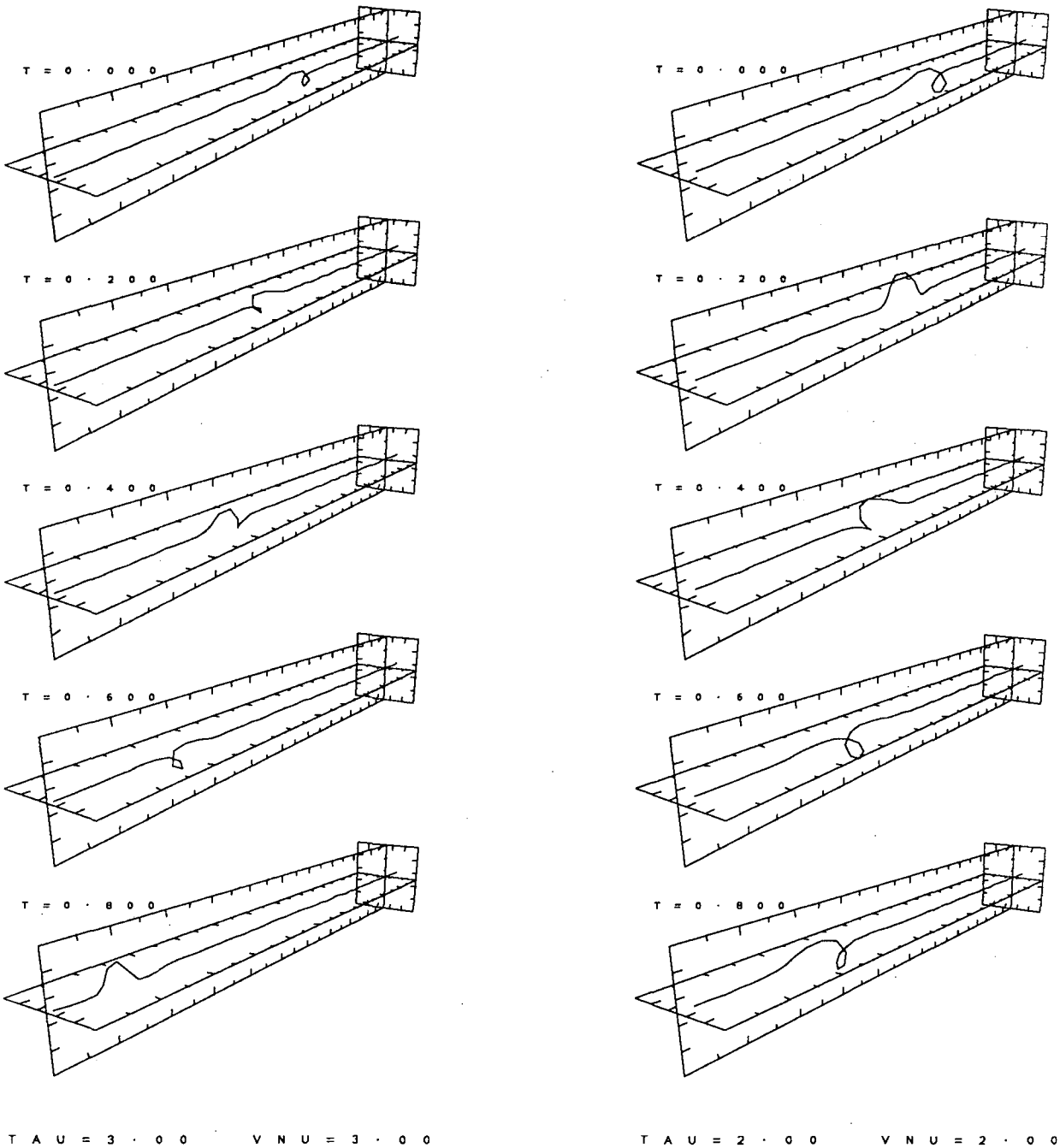

Figure 3.2. Perspective views of a solitary wave moving along a filament. The parameters $\tau = 3.0$ and $\nu = 3.0$ are for the left figures; $\tau = 2.0$ and $\nu = 2.0$ are for the right figures.

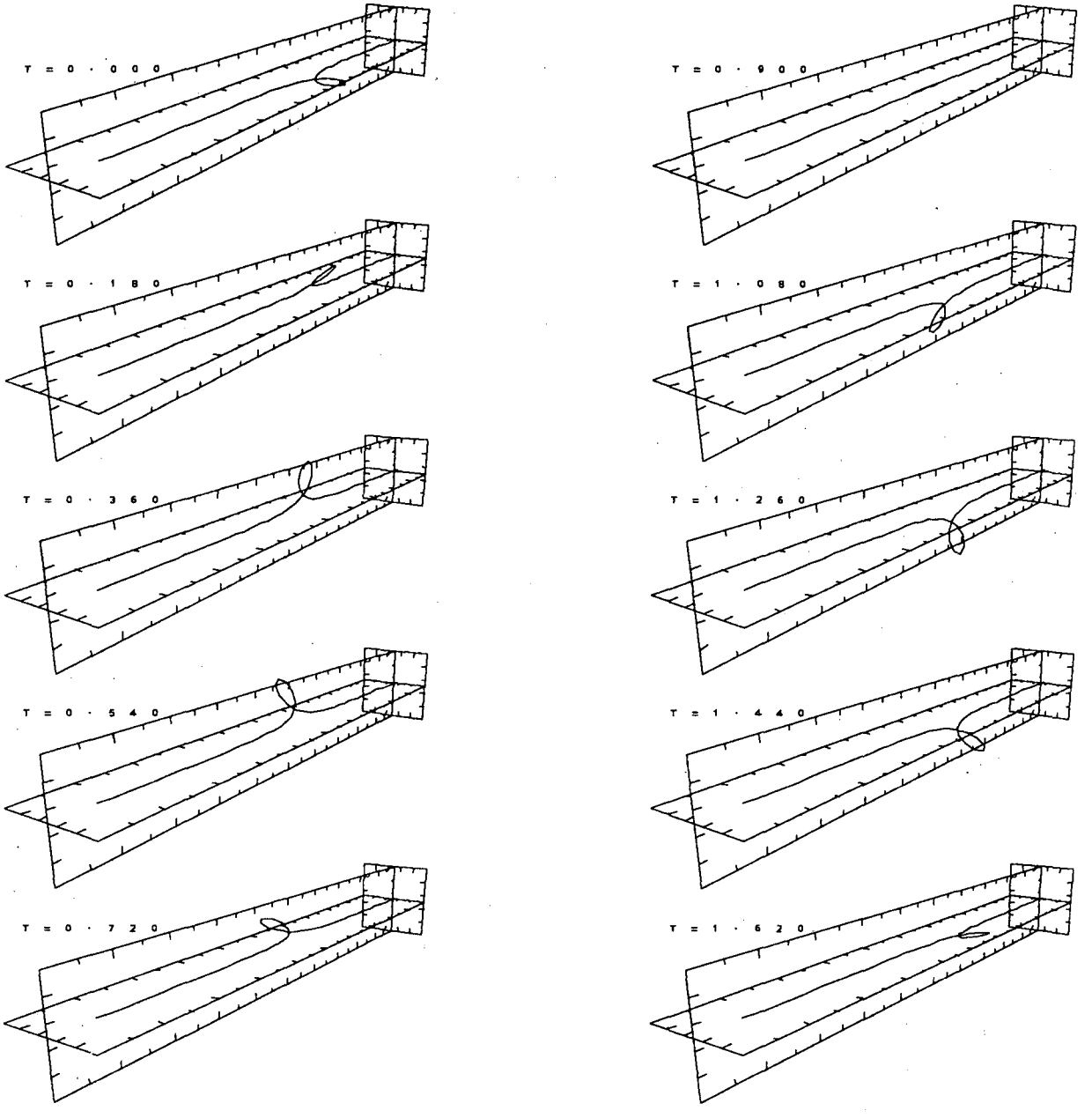

Figure 3.3. Perspective views of a solitary wave motion with $\tau = 0$.

Chapter 4

Energy Conservation and Other Diagnostics

4.1 Some Invariants of Euler's Equations

We use several invariants of Euler's equations to check the validity of our numerical schemes. They are the total vorticity Ω, linear impulse $\mathbf{I}$, and kinetic energy E of a vortex system defined by

$$\Omega = \int \omega dV \tag{4.1}$$

$$\mathbf{I} = \frac{1}{2}\int \mathbf{x} \times \omega dV \tag{4.2}$$

$$E = \frac{1}{2}\int \mathbf{u} \cdot \mathbf{u} dV \tag{4.3}$$

where we have assumed that the density is one.

For an unbounded flow with zero velocity and zero vorticity at infinity, for example, the closed ring, the total vorticity Ω is zero. The linear impulse $\mathbf{I}$ is independent of time. To see this, we write the vorticity transport equation (2.6) as

$$\frac{\partial \omega}{\partial t} = (\omega \cdot \nabla)\mathbf{u} - (\mathbf{u} \cdot \nabla)\omega = \nabla \times (\mathbf{u} \times \omega) \tag{4.4}$$

where we have used the facts that $\nabla \cdot \mathbf{u} = 0$ and $\nabla \cdot \omega = 0$ and the vector identity

$$\nabla \times (\mathbf{v} \times \mathbf{w}) = (\mathbf{w} \cdot \nabla)\mathbf{v} - \mathbf{w}(\nabla \cdot \mathbf{v}) - (\mathbf{v} \cdot \nabla)\mathbf{w} + \mathbf{v}(\nabla \cdot \mathbf{w})$$

Note that the integrating region is fixed in this case. Thus

$$\frac{d\mathbf{I}}{dt} = \frac{1}{2}\int \mathbf{x} \times \frac{\partial \boldsymbol{\omega}}{\partial t} dV = \frac{1}{2}\int \mathbf{x} \times [\nabla \times (\mathbf{u} \times \boldsymbol{\omega})] dV$$

Expanding the integrand, performing integration by parts, and using the fact that $\mathbf{u}$ and $\boldsymbol{\omega}$ vanish at infinity, we find

$$\frac{d\mathbf{I}}{dt} = \int \mathbf{u} \times \boldsymbol{\omega} dV \tag{4.5}$$

A simple computation shows

$$\begin{aligned} \mathbf{u} \times \boldsymbol{\omega} &= \frac{1}{2}\nabla(\mathbf{u} \cdot \mathbf{u}) - (\mathbf{u} \cdot \nabla)\mathbf{u} \\ &= \frac{1}{2}\nabla(\mathbf{u} \cdot \mathbf{u}) - \frac{\partial(u\mathbf{u})}{\partial x} - \frac{\partial(v\mathbf{u})}{\partial y} - \frac{\partial(w\mathbf{u})}{\partial z} \end{aligned} \tag{4.6}$$

where the last equality holds, since $\nabla \cdot \mathbf{u} = 0$. Thus the integral of equation (4.5) can be transformed to a surface integral that is zero because $\mathbf{u} = 0$ at infinity.

The kinetic energy is also conserved. By Euler's equations (2.1) and (2.2) and the same argument as above,

$$\begin{aligned} \frac{dE}{dt} &= \int \mathbf{u} \cdot \frac{\partial \mathbf{u}}{\partial t} dV = -\int \mathbf{u} \cdot [\nabla P + (\mathbf{u} \cdot \nabla)\mathbf{u}] dV \\ &= -\int \nabla \cdot [(\frac{1}{2}\mathbf{u} \cdot \mathbf{u} + P)\mathbf{u}] dV = 0 \end{aligned}$$

It is possible to find an expression for the total kinetic energy in terms of the vorticity distribution. Let $\boldsymbol{\Psi}$ be the function defined by the expression $\mathbf{u} = \nabla \times \boldsymbol{\Psi}$, with the constraint $\nabla \cdot \boldsymbol{\Psi} = 0$, as in Chapter 2. From the vector identity

$$(\nabla \times \boldsymbol{\Psi}) \cdot \mathbf{u} = \boldsymbol{\Psi} \cdot (\nabla \times \mathbf{u}) - \nabla \cdot (\mathbf{u} \times \boldsymbol{\Psi}) = \boldsymbol{\Psi} \cdot \boldsymbol{\omega} - \nabla \cdot (\mathbf{u} \times \boldsymbol{\Psi})$$

we get

$$E = \frac{1}{2}\int \boldsymbol{\Psi} \cdot \boldsymbol{\omega} dV - \frac{1}{2}\int \nabla \cdot (\mathbf{u} \times \boldsymbol{\Psi}) dV \tag{4.7}$$

The second integral vanishes by the same argument as before. Thus

$$E = \frac{1}{2}\int \boldsymbol{\Psi} \cdot \boldsymbol{\omega} dV \tag{4.8}$$

By equation (2.17),

$$E = \frac{1}{8\pi}\int\int \frac{\boldsymbol{\omega} \cdot \boldsymbol{\omega}'}{r} dV(\mathbf{x}) dV(\mathbf{x}') \tag{4.9}$$

This expression is also called the *Lamb integral* [52].

4.2 Numerical Diagnostics

We call the conserved quantities such as kinetic energy, linear impulse, and total vorticity the diagnostics of our numerical scheme because a good numerical scheme for solving the Euler's equation in unbounded region should preserve these quantities. The discretizations of these diagnostics are based on the same theoretical analysis used to obtain the schemes for vortex filament methods in Chapter 2. We adopt the same notations used in Chapter 2. Then, for a single filament,

$$\begin{aligned} \Omega &= \int_{W_t} \omega dV = \Gamma \int_{C_t} d\mathbf{l}(\mathbf{x}) \\ &= \Gamma \sum_{j=1}^{N} \int_{\delta \mathbf{l}_j} d\mathbf{l}(\mathbf{x}) \approx \Gamma \sum_{j=1}^{N} \delta \mathbf{l}_j \qquad (4.10) \\ \mathbf{I} &= \frac{1}{2} \int_{W_t} \mathbf{x} \times \omega dV = \frac{\Gamma}{2} \int_{C_t} \mathbf{x} \times d\mathbf{l} \\ &= \frac{\Gamma}{2} \sum_{j=1}^{N} \int_{\delta \mathbf{l}_j} \mathbf{x} \times d\mathbf{l} \approx \frac{\Gamma}{2} \sum_{j=1}^{N} \mathbf{a}_j \times \delta \mathbf{l}_j \qquad (4.11) \end{aligned}$$

where $\mathbf{a}_j = (\mathbf{x}_{j+1} + \mathbf{x}_j)/2$.

Similarly, for M filaments,

$$\Omega \approx \sum_{m=1}^{M} \Gamma^{(m)} \sum_{j=1}^{N_m} \delta \mathbf{l}_j^{(m)} \qquad (4.12)$$

$$\mathbf{I} \approx \frac{1}{2} \sum_{m=1}^{M} \Gamma^{(m)} \sum_{j=1}^{N} \mathbf{a}_j^{(m)} \times \delta \mathbf{l}_j^{(m)} \qquad (4.13)$$

where $\mathbf{a}_j^{(m)} = (\mathbf{x}_{j+1}^{(m)} + \mathbf{x}_j^{(m)})/2$.

The energy computation is a little more complicated. From equation (4.9),

$$\begin{aligned} E &= \frac{1}{8\pi} \int_V \int_V \frac{\omega(\mathbf{x}) \cdot \omega(\mathbf{x}')}{|\mathbf{x} - \mathbf{x}'|} dV(\mathbf{x}) dV(\mathbf{x}') \\ &= \frac{1}{8\pi} \sum_{i=1}^{N} \sum_{j=1}^{N} \int_{\delta V_i} \int_{\delta V_j} \frac{\omega(\mathbf{x}) \cdot \omega(\mathbf{x}')}{|\mathbf{x} - \mathbf{x}'|} dV(\mathbf{x}) dV(\mathbf{x}') \\ &= \sum_{i=1}^{N} \sum_{j \neq i} E_{ij} + \sum_{i=1}^{N} E_{ii} \qquad (4.14) \end{aligned}$$

where

$$E_{ij} = \frac{1}{8\pi} \int_{\delta V_i} \int_{\delta V_j} \frac{\omega(\mathbf{x}) \cdot \omega(\mathbf{x}')}{|\mathbf{x} - \mathbf{x}'|} dV(\mathbf{x}) dV(\mathbf{x}')$$

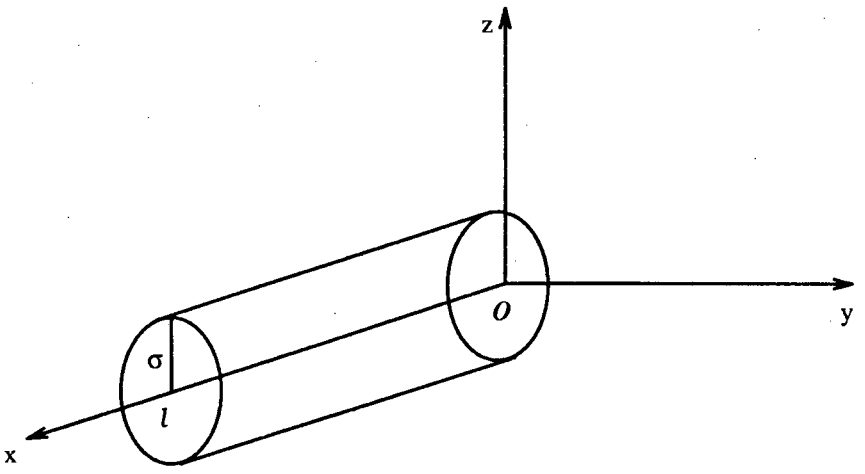

Figure 4.1. A piece of a cylindrical vortex tube.

Now we see that the total kinetic energy in a considered region consists of two parts. One is the sum of E_{ii}, the *self-energy*, denoted by E_s; the other consists of the remaining terms, the *exchange energy*, denoted by E_e.

For these terms E_{ij} in E_e, $i \neq j$, under the more restrictive condition:

$$\max(|\delta \mathbf{l}_i|, |\delta \mathbf{l}_j|) \ll r_{ij}$$

where r_{ij} is the distance between the midpoints of two segments $\delta \mathbf{l}_i$ and $\delta \mathbf{l}_j$. We may approximate E_{ij} as usual,

$$E_{ij} = \frac{\Gamma_i \Gamma_j}{8\pi} \int_{\delta \mathbf{l}_i} \int_{\delta \mathbf{l}_j} \frac{d\mathbf{l}_i \cdot d\mathbf{l}_j}{|\mathbf{x} - \mathbf{x}'|} \approx \frac{\Gamma_i \Gamma_j}{8\pi} \frac{\delta \mathbf{l}_i \cdot \delta \mathbf{l}_j}{r_{ij}} \tag{4.15}$$

However, it is clear that the terms E_{ii} in E_s can not be approximated so simply, and E_{ii} is also too large to be ignored. Chorin resolved this difficulty by using a scaling property of E_{ii} [18, 19, 20, 21, 22, 23, 24, 26].

4.3 Scaling Property and Computation of Self-Energy

To derive the scaling property of self-energy, we consider a piece of a cylindrical vortex tube with height ℓ and cross-section radius σ lying on the coordinate

system given by Figure 4.1. We denote the total kinetic energy in this piece as $E(\sigma, \ell)$; i.e.,

$$E(\sigma,\ell) = \frac{1}{8\pi}\int_{-\sigma}^{\sigma} dy \int_{-\sqrt{\sigma^2-y^2}}^{\sqrt{\sigma^2-y^2}} dz \int_0^{\ell} dx \int_{-\sigma}^{\sigma} dy' \int_{-\sqrt{\sigma^2-y'^2}}^{\sqrt{\sigma^2-y'^2}} dz' \int_0^{\ell} dx' \frac{\boldsymbol{\omega}(\mathbf{x})\cdot\boldsymbol{\omega}(\mathbf{x}')}{|\mathbf{x}-\mathbf{x}'|} \tag{4.16}$$

Clearly, the vorticity $\boldsymbol{\omega}$ depends on the radius σ and can be written as $\boldsymbol{\omega}_\sigma = (\xi_\sigma, 0, 0)$ in the given coordinate system. We will assume that the circulation $\boldsymbol{\omega}_\sigma \cdot \mathbf{n}A(\sigma) = \xi_\sigma A(\sigma)$ is fixed, where $A(\sigma) = \pi\sigma^2$ (one will see the justification later); that is, for a real parameter $\epsilon > 0$,

$$\xi_{\epsilon\sigma}(\epsilon\mathbf{x})A(\epsilon\sigma) = \xi_\sigma(\mathbf{x})A(\sigma)$$

or

$$\xi_{\epsilon\sigma}(\epsilon\mathbf{x}) = \frac{1}{\epsilon^2}\xi_\sigma(\mathbf{x}) \tag{4.17}$$

Thus, let $\mathbf{x} = \epsilon\tilde{\mathbf{x}}$ and $\mathbf{x}' = \epsilon\tilde{\mathbf{x}}'$,

$$\begin{aligned}
E(\epsilon\sigma,\epsilon\ell) &= \frac{1}{8\pi}\int_{-\epsilon\sigma}^{\epsilon\sigma} dy \int_{-\sqrt{\epsilon^2\sigma^2-y^2}}^{\sqrt{\epsilon^2\sigma^2-y^2}} dz \int_0^{\epsilon\ell} dx \int_{-\epsilon\sigma}^{\epsilon\sigma} dy' \int_{-\sqrt{\epsilon^2\sigma^2-y'^2}}^{\sqrt{\epsilon^2\sigma^2-y'^2}} dz' \int_0^{\epsilon\ell} dx' \frac{\boldsymbol{\omega}_{\epsilon\sigma}(\mathbf{x})\cdot\boldsymbol{\omega}_{\epsilon\sigma}(\mathbf{x}')}{|\mathbf{x}-\mathbf{x}'|} \\
&= \frac{\epsilon^5}{8\pi}\int_{-\sigma}^{\sigma} d\tilde{y} \int_{-\sqrt{\sigma^2-\tilde{y}^2}}^{\sqrt{\sigma^2-\tilde{y}^2}} d\tilde{z} \int_0^{\ell} d\tilde{x} \int_{-\sigma}^{\sigma} d\tilde{y}' \int_{-\sqrt{\sigma^2-\tilde{y}'^2}}^{\sqrt{\sigma^2-\tilde{y}'^2}} d\tilde{z}' \int_0^{\ell} d\tilde{x}' \frac{\boldsymbol{\omega}_{\epsilon\sigma}(\epsilon\tilde{\mathbf{x}})\cdot\boldsymbol{\omega}_{\epsilon\sigma}(\epsilon\tilde{\mathbf{x}}')}{|\tilde{\mathbf{x}}-\tilde{\mathbf{x}}'|} \\
&= \frac{\epsilon^5}{8\pi}\int_{-\sigma}^{\sigma} dy \int_{-\sqrt{\sigma^2-y^2}}^{\sqrt{\sigma^2-y^2}} dz \int_0^{\ell} dx \int_{-\sigma}^{\sigma} dy' \int_{-\sqrt{\sigma^2-y'^2}}^{\sqrt{\sigma^2-y'^2}} dz' \int_0^{\ell} dx' \frac{\boldsymbol{\omega}_\sigma(\mathbf{x})\cdot\boldsymbol{\omega}_\sigma(\mathbf{x}')}{\epsilon^4|\mathbf{x}-\mathbf{x}'|} \\
&= \epsilon E(\sigma,\ell)
\end{aligned}$$

That is,

$$E(\epsilon\sigma,\epsilon\ell) = \epsilon E(\sigma,\ell) \tag{4.18}$$

Let $\epsilon = \frac{1}{\sigma}$; we then find

$$E(\sigma,\ell) = \sigma E(1,\ell/\sigma) = \sigma T(\ell/\sigma) \tag{4.19}$$

where $T(\ell) = E(1,\ell)$ is a single variable function.

To study the properties of $T(\ell)$, we assume that the vorticity $\boldsymbol{\omega}_\sigma$ is constant in space and time, e.g., $\boldsymbol{\omega}_\sigma(\mathbf{x})\cdot\boldsymbol{\omega}_\sigma(\mathbf{x}') = C(\sigma)$. Then

$$T(\ell) = \frac{C(1)}{8\pi}\int_{S(1)}\int dydz \int_{S(1)}\int dy'dz' \int_0^{\ell} dx \int_0^{\ell} dx' \frac{1}{\sqrt{(x'-x)^2+(y'-y)^2+(z'-z)^2}}$$

where $S(\sigma) = \{(y,z) : y^2 + z^2 \le \sigma^2\}$. Since

$$\begin{aligned}
&\int_0^\ell dx \int_0^\ell dx' \frac{1}{\sqrt{(x'-x)^2 + (y'-y)^2 + (z'-z)^2}} \\
&= 2\ell \ln\left[\ell + \sqrt{\ell^2 + (y'-y)^2 + (z'-z)^2}\right] \\
&\quad -2\sqrt{\ell^2 + (y'-y)^2 + (z'-z)^2} \\
&\quad +2\sqrt{(y'-y)^2 + (z'-z)^2} \\
&\quad -\ell \ln[(y'-y)^2 + (z'-z)^2]
\end{aligned}$$

Let $y = \rho\cos\theta$, $z = \rho\sin\theta$, $y' = \rho'\cos\theta'$, and $z' = \rho'\sin\theta'$. Then

$$\begin{aligned}
T(\ell) &= \frac{C(1)}{8\pi} \int_0^{2\pi}\int_0^{2\pi} d\theta d\theta' \int_0^1\int_0^1 d\rho d\rho' \rho\rho' \\
&\quad \cdot \Big\{ 2\ell \cdot \ln\left[\ell + \sqrt{\ell^2 + \rho^2 + \rho'^2 - 2\rho\rho'\cos(\theta-\theta')}\right] \\
&\quad -2\sqrt{\ell^2 + \rho^2 + \rho'^2 - 2\rho\rho'\cos(\theta-\theta')} \\
&\quad -\ell \ln[\rho^2 + \rho'^2 - 2\rho\rho'\cos(\theta-\theta')] \\
&\quad +2\sqrt{\rho^2 + \rho'^2 - 2\rho\rho'\cos(\theta-\theta')} \Big\}
\end{aligned} \tag{4.20}$$

Let us look at the asymptotical behavior of $T(\ell)$. For $\ell \to +\infty$,

$$\begin{aligned}
\lim_{\ell\to+\infty} \frac{T(\ell)}{\ell\ln\ell} &= \frac{C(1)}{4\pi} \int_0^{2\pi}\int_0^{2\pi} d\theta d\theta' \int_0^1\int_0^1 d\rho d\rho' \rho\rho' \\
&\quad \cdot \left\{ \lim_{\ell\to+\infty} \frac{\ln\left[\ell + \sqrt{\ell^2 + \rho^2 + \rho'^2 - 2\rho\rho'\cos(\theta-\theta')}\right]}{\ln\ell} \right\} \\
&= \frac{C(1)}{4\pi} \int_0^{2\pi}\int_0^{2\pi} d\theta d\theta' \int_0^1\int_0^1 d\rho d\rho' \rho\rho' \cdot 1 \\
&= \frac{\pi C(1)}{4}
\end{aligned}$$

That is,

$$T(\ell) \sim constant \cdot \ell\ln\ell \quad for \ \ \ell \to +\infty \tag{4.21}$$

To find the asymptotical formula of $T(\ell)$ for $\ell \to 0$, we take the derivative of $T(\ell)$,

$$\begin{aligned}
\frac{dT}{d\ell} &= \frac{C(1)}{8\pi} \int_0^{2\pi}\int_0^{2\pi} d\theta d\theta' \int_0^1\int_0^1 d\rho d\rho' \rho\rho' \\
&\quad \cdot \Big\{ 2\ln\left[\ell + \sqrt{\ell^2 + \rho^2 + \rho'^2 - 2\rho\rho'\cos(\theta-\theta')}\right] \\
&\quad -\ln\left[\rho^2 + \rho'^2 - 2\rho\rho'\cos(\theta-\theta')\right] \Big\}
\end{aligned}$$

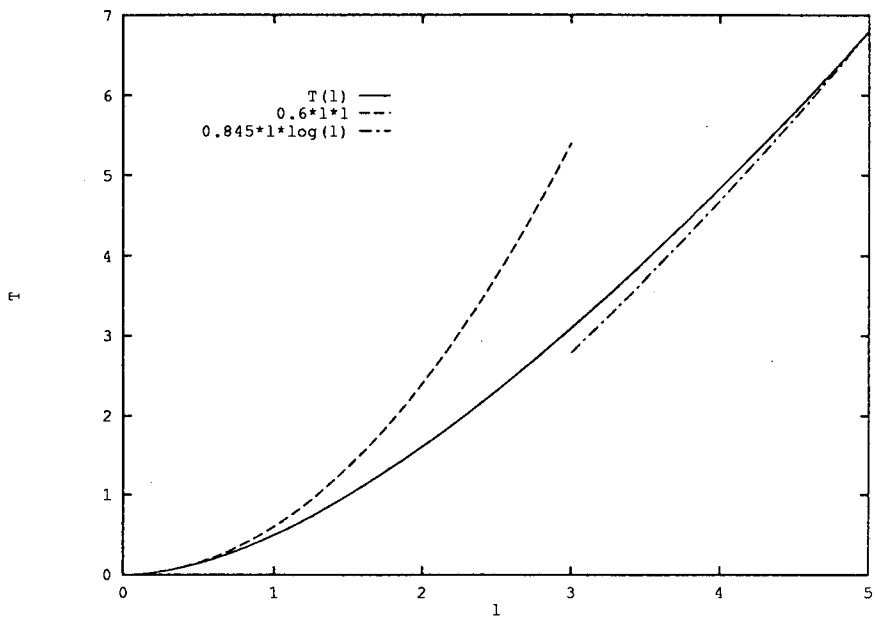

Figure 4.2. Asymptotical properties of $T(\ell)$ with $C(1) = 1$.

Then

$$\begin{aligned}
\lim_{\ell \to 0} \frac{dT}{d\ell} &= 0 \\
\lim_{\ell \to 0} \frac{1}{\ell} \frac{dT}{d\ell} &= \frac{C(1)}{4\pi} \int_0^{2\pi} \int_0^{2\pi} d\theta d\theta' \int_0^1 \int_0^1 d\rho d\rho' \frac{\rho\rho'}{\sqrt{\rho^2 + \rho'^2 - 2\rho\rho' \cos(\theta - \theta')}}
\end{aligned}$$

Thus,

$$T(\ell) \sim constant \cdot \ell^2 \quad for \ \ \ell \to 0 \tag{4.22}$$

Figure 4.2 shows the asymptotical properties of $T(\ell)$, where $C(1) = 1$. For $\ell \to 0$, the asymptotical function is $0.6\,\ell^2$. For $\ell \to \infty$ the asymptotical function is $0.845\,\ell \ln \ell$.

Now the question is how to compute $T(\ell)$. Once we find a way to compute $T(\ell)$, we can make a data base and use interpolation and equation (4.19) to compute $E(\sigma, \ell)$ for any given σ and ℓ. Since the vorticity $\boldsymbol{\omega}$ depends on core structure, we should not assume $\boldsymbol{\omega}$ to be a constant vector. We must evaluate $T(\ell)$ from equation (4.16). Therefore we need to compute $\boldsymbol{\omega}_\sigma$ first. From equations (2.43) and (2.27) and the definition of $\psi_\sigma(\mathbf{x})$ at page 10 Chapter 2,

$$\boldsymbol{\omega}_\sigma(\mathbf{x}, t) = \frac{\Gamma}{4\pi} \int_{C_t} \frac{f'(\frac{r}{\sigma}) d\mathbf{l}(\mathbf{x}')}{\sigma r^2}$$

$$
\begin{aligned}
&= \frac{\Gamma}{4\pi\sigma}\sum_{j=1}^{N}\int_{\delta\mathbf{l}_j}\frac{f'(\frac{r}{\sigma})d\mathbf{l}(\mathbf{x}')}{r^2} \\
&\approx \frac{\Gamma}{4\pi\sigma}\sum_{j=1}^{N}\frac{f'(\frac{a_j}{\sigma})\delta\mathbf{l}_j}{a_j^2}
\end{aligned}
\tag{4.23}
$$

where $r = |\mathbf{x} - \mathbf{x}'|$ and $a_j^2 = |\frac{\mathbf{x}_{j+1}+\mathbf{x}_j}{2} - \mathbf{x}|^2$. From the first equality, we can see that

$$\boldsymbol{\omega}_{\epsilon\sigma}(\epsilon\mathbf{x}, t) = \frac{1}{\epsilon^2}\boldsymbol{\omega}_{\sigma}(\mathbf{x}, t)$$

which justifies the assumption of equation (4.17). From equation (4.23),

$$
\begin{aligned}
T(\ell) \approx \frac{\Gamma^2}{128\pi^3}\int_0^{2\pi}d\theta\int_0^1 d\rho\int_0^{\ell}dz\int_0^{2\pi}d\theta'\int_0^1 d\rho'\int_0^{\ell}dz' \\
\frac{\rho\rho'\sum_{i=1}^{N}\sum_{j=1}^{N}\frac{f'(a_i)f'(a_j')\delta\mathbf{l}_i\cdot\delta\mathbf{l}_j}{a_i^2 a_j'^2}}{\sqrt{\rho^2+\rho'^2-2\rho\rho'\cos(\theta-\theta')+(z-z')^2}}
\end{aligned}
\tag{4.24}
$$

Using standard integration schemes such as the trapezoidal sum and Gaussian integration methods (see, for example, Stoer & Bulirsch [68, pp. 121, 142]), we can easily generate a data base for various core functions. The self-energy can be computed as

$$E_s = \sum_{i=1}^{N}\sigma_i T(\ell_i/\sigma_i) \tag{4.25}$$

where $\ell_i = |\delta\mathbf{l}_i|$.

In Figure 4.3, We plot the $T(\ell)$s for the four core functions given in Chapter 2, where the label in the picture is defined as follows:

Core function 1 is $1 - e^{-r^3}$
Core function 2 is $\tanh r^3$
Core function 3 is $1 + (-1 + \frac{3}{2}r^3)e^{-r^3}$
Core function 4 is $\tanh r^3 + \frac{3}{2}r^3\mathrm{sech}^2 r^3$

In the future, the kinetic energy is given by the approximate expression

$$E = E_e + E_s$$

where $E_e = \sum_{i=1}^{N}\sum_{j\neq i}E_{ij}$, $E_{ij} = \frac{\Gamma_i\Gamma_j}{8\pi}\frac{\delta\mathbf{l}_i\cdot\delta\mathbf{l}_j}{r_{ij}}$ and E_s is given by equation (4.25).

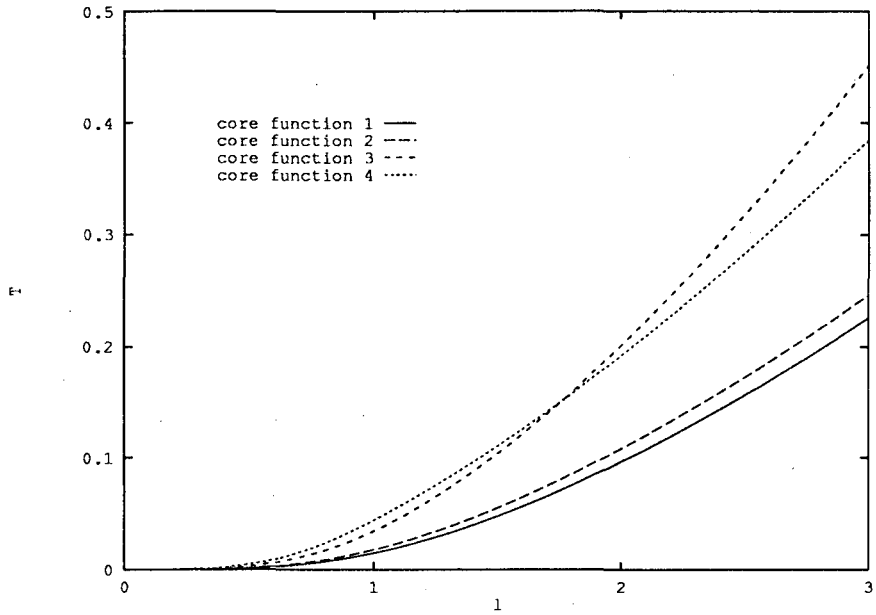

Figure 4.3. $T(\ell)$s corresponding to four core functions.

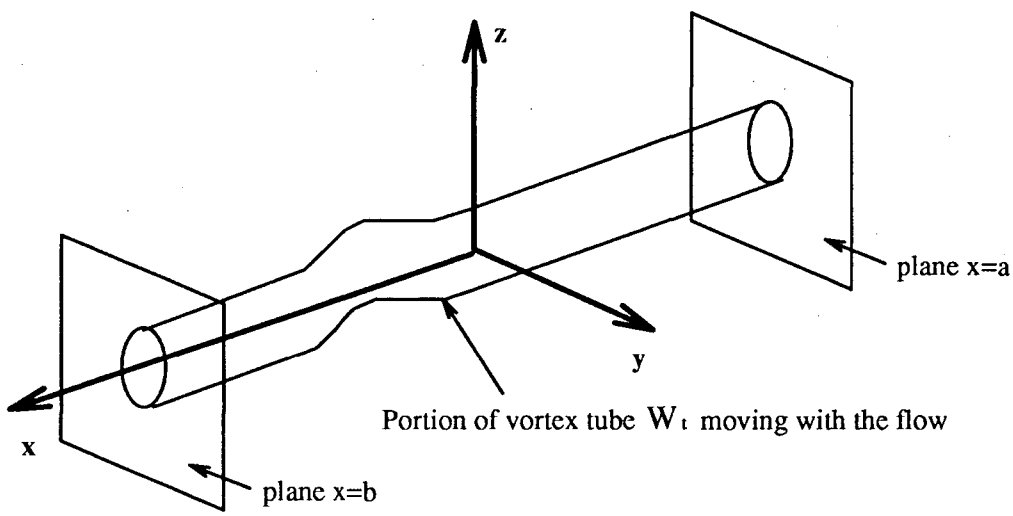

Figure 4.4. A portion of a vortex tube.

4.4 The Limitations of the Diagnostics

We studied the invariants of Euler's equations such as kinetic energy, total vorticity, and linear impulse. We also derived the numerical schemes for computing these invariants. It is important to note that all the derivation in previous sections in this chapter is carried out in whole three-dimensional space $\mathbf{R}^3$. However, in our study, we often take only a portion of space, for example, the x direction bounded and the y and z directions unbounded, for an unbounded flow (see Figure 4.4). The chosen portion moves with the flow. We therefore designate the volume of that portion as

$$W_t = \{(x, y, z,) : \ a(t) \leq x \leq b(t), \ -\infty < y, z < +\infty\}.$$

It is of practical interest to know whether the quantities discussed in previous sections are conserved in the restricted circumstance.

It is clear that the total vorticity in the given portion W_t does not vanish. However, the total vorticity in the given portion W_t is independent of time,

$$\begin{aligned} \frac{d}{dt}\int_{W_t} \boldsymbol{\omega} dV &= \frac{d}{dt}\int_{W_t} \nabla \times \mathbf{u} dV = \int_{W_t} \nabla \times \frac{D\mathbf{u}}{Dt} dV \\ &= -\int_{W_t} \nabla \times (\nabla P) dV = 0 \end{aligned}$$

where we have used Euler's equations (2.1) and (2.2).

Generally, in the restricted region W_t, the kinetic energy is not conserved, and equation (4.9) is not equivalent to equation (4.3) due to the nonvanishing boundary terms. We denote $\mathbf{u} = (u, v, w)^t$, $\boldsymbol{\omega} = (\xi, \zeta, \gamma)^t$, and $\boldsymbol{\Psi} = (\alpha, \beta, \eta)^t$. Let us compute dE/dt on W_t,

$$\begin{aligned} \frac{dE}{dt} &= \int_{W_t} \frac{D}{Dt}(\mathbf{u} \cdot \mathbf{u}) dV \\ &= \frac{1}{2}\int_{W_t} \mathbf{u} \cdot \frac{D\mathbf{u}}{Dt} dV \\ &= -\frac{1}{2}\int_{W_t} \mathbf{u} \cdot \nabla P dV \\ &= -\frac{1}{2}\int_{W_t} \nabla(\mathbf{u}P) dV \\ &= -\frac{1}{2}\int_{\mathbf{R}^2} [(uP)|_{x=a}^{x=b}] dA(y, z) \end{aligned}$$

where $\mathbf{u} = (u, v, w)$ and we used the fact that

$$\mathbf{u} \cdot \nabla P = \nabla(\mathbf{u}P) - (\nabla \cdot \mathbf{u})P = \nabla(\mathbf{u}P)$$

since $\nabla \cdot \mathbf{u} = 0$. The last surface integration does not vanish unless $\mathbf{u} = 0$ or $P = 0$ at both planes $x = a$ and $x = b$. Therefore the kinetic energy E in the restricted region W_t is not conserved generally. The second term of equation (4.7) can not be eliminated generally on the restricted portion W_t because

$$\int_{W_t} \nabla \cdot (\mathbf{u} \times \boldsymbol{\Psi}) = \int_{\mathbf{R}^2} [(v\eta - w\beta)|_{x=a}^{x=b}] dA(y, z)$$

Thus, on the restricted portion W_t, equation (4.9) is not equivalent to equation (4.3) generally.

The linear impulse in the restricted region W_t is also not conserved generally. Let us compute $d\mathbf{I}/dt$,

$$\frac{d\mathbf{I}}{dt} = \int_{W_t} \frac{D}{Dt}(\mathbf{x} \times \boldsymbol{\omega}) dV = \int_{W_t} (\mathbf{u} \times \boldsymbol{\omega} + \mathbf{x} \times \frac{D\boldsymbol{\omega}}{Dt}) dV$$

where

$$\begin{aligned} \int_{W_t} \mathbf{u} \times \boldsymbol{\omega} dV &= \int_{W_t} [\frac{1}{2}\nabla(\mathbf{u} \cdot \mathbf{u}) - \frac{\partial(u\mathbf{u})}{\partial x} - \frac{\partial(v\mathbf{u})}{\partial y} - \frac{\partial(w\mathbf{u})}{\partial z}] dV \\ &= \begin{pmatrix} \frac{1}{2}\int_{\mathbf{R}^2}[(v^2 + w^2 - u^2)|_{x=a}^{x=b}] dA(y, z) \\ -\int_{\mathbf{R}^2}[(uv)|_{x=a}^{x=b}] dA(y, z) \\ -\int_{\mathbf{R}^2}[(uw)|_{x=a}^{x=b}] dA(y, z) \end{pmatrix} \end{aligned}$$

and

$$\int_{W_t} \mathbf{x} \times \frac{D\boldsymbol{\omega}}{Dt} dV = \int_{W_t} \mathbf{x} \times (\boldsymbol{\omega} \cdot \nabla)\mathbf{u} dV$$

Both the surface integration and the integration $\int_{W_t} \mathbf{x} \times (\boldsymbol{\omega} \cdot \nabla)\mathbf{u} dV$ do not vanish generally. Therefore, $d\mathbf{I}/dt \neq 0$; that is, the linear impulse in the restricted region W_t is not conserved.

For a straight filament lying on, or parallel to, the x-axis with the velocity field induced by itself, the discussion about kinetic energy and linear impulse in previous sections is valid for the portion within the region W_t. In this case, $y =$ constant, $z =$ constant, $u = 0$, $\zeta = 0$, and $\gamma = 0$. Thus $v_x = 0$ and $w_x = 0$ from

the definition of $\boldsymbol{\omega}$ and $\beta = 0$, $\eta = 0$ by equation (2.17). With these facts and the assumption that $\mathbf{u}$ and $\boldsymbol{\omega}$ vanish at infinity, we can eliminate all of the boundary terms generated in our calculation as well as the integration $\int_{W_t} \mathbf{x} \times (\boldsymbol{\omega} \cdot \nabla)\mathbf{u} dV$.

This argument explains that in our numerical computation the kinetic energy E can remain constant as long as the perturbation waves stay far from the steady boundaries and start to vary once the boundaries are affected by perturbation waves.

From the analysis given in this section, in the computation of a portion of a vortex tube moving with the flow, we know that the total vorticity remains a good diagnostic of a numerical algorithm; the kinetic energy can be used as a diagnostic of a numerical algorithm only if there is no perturbation near the boundaries of the considered region on the vortex tube, and the linear impulse cannot be used as a diagnostic of a numerical algorithm because any perturbation on the vortex tube in the considered region will change the linear impulse.

Chapter 5

Calculations on Part of a Vortex Tube

It is often convenient to calculate part of a (possibly infinitly long) vortex tube. To do this, we must truncate the uncomputed tails of the vortex tube. This Chapter discusses how this can be done.

Consider first a straight vortex tube. Assume that the tube consists of a bundle of straight parallel filaments with equal circulation. To simplify the discussion, we assume that the straight filaments are parallel to the x-axis. Thus a plane perpendicular to these filaments should be parallel to the y-z plane. Denote a plane parallel to the y-z plane and passing through the point $(x, 0, 0)$ on the x-axis by P_x. Thus P_0 is the y-z plane. We define the velocity center $C_v(x)$ on the plane P_x as the point where the y-z component of velocity is zero, as shown in Figure 5.2. There may be several velocity centers. For simplicity, we consider only the pattern of the velocity distribution shown in Figure 5.2. Thus, there is only one velocity center on a given plane P_x. Let C_v be a curve consisting of all $C_v(x)$, see Figure 5.1.

The filaments away from the center curve C_v will rotate around the C_v. We can also see that the rotation speed at various points (x, y, z) changes according to the values of the y and z coordinates. For an infinitly long straight vortex tube, the velocity distribution on the plane P_x with a different x is the same. Thus, all points on the same straight filament should rotate with the same speed around the velocity

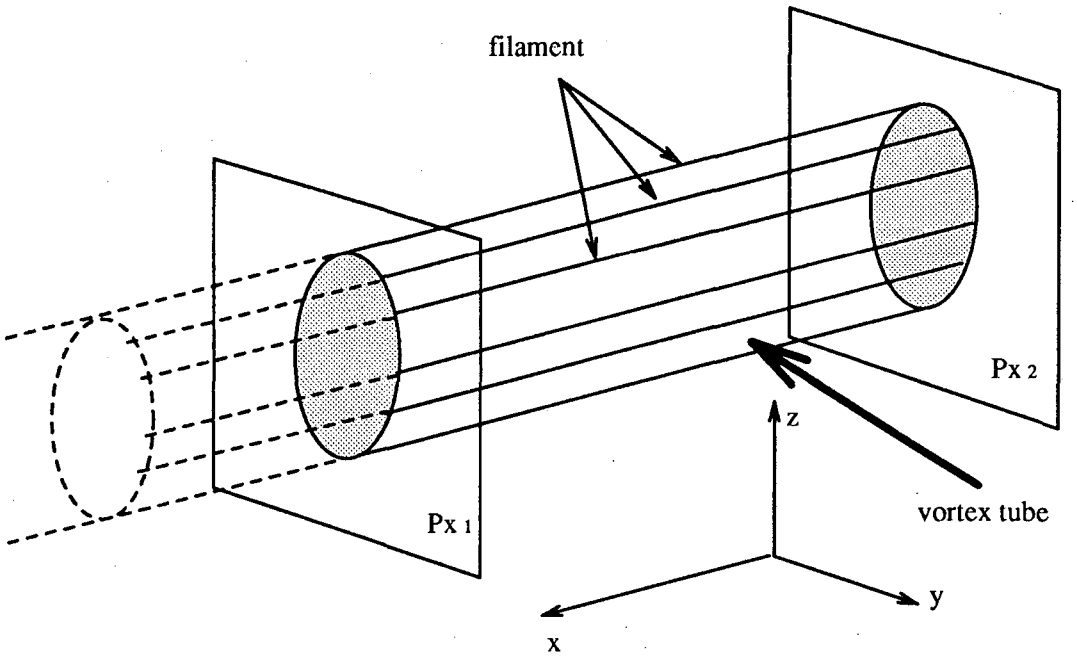

Figure 5.1. A finite part of an infinitly long vortex tube.

center curve C_v. Without proper treatment at the truncated ends, a computational result of part of a vortex tube will not preserve the above property due to the loss of the appropriate contribution from the truncated parts during the computation. Near the truncated ends, the computed velocity magnitude will be quite different from the velocity magnitude induced by whole vortex tube. Consequently, the points on the same straight filament will rotate with different speeds. A physically unreasonable twisting of filaments will start at the truncated ends and quickly spread to the middle parts.

The way to eliminate this physically unreasonable twisting of filaments is to recover the correct velocity intensity near the truncated ends. We have used two ways to do so in our computation: (1) treat the data periodically, which is a conventional method of dealing with this kind of situation, and (2) extend each filament with straight lines at both ends. Both of the methods are simple to implement in the computation. Both methods require extension on both ends. The extension on each end is equivalent to adding the terms into the summation in equation (2.46). For the first method, we copy the computed part at each end and connect it to the previous

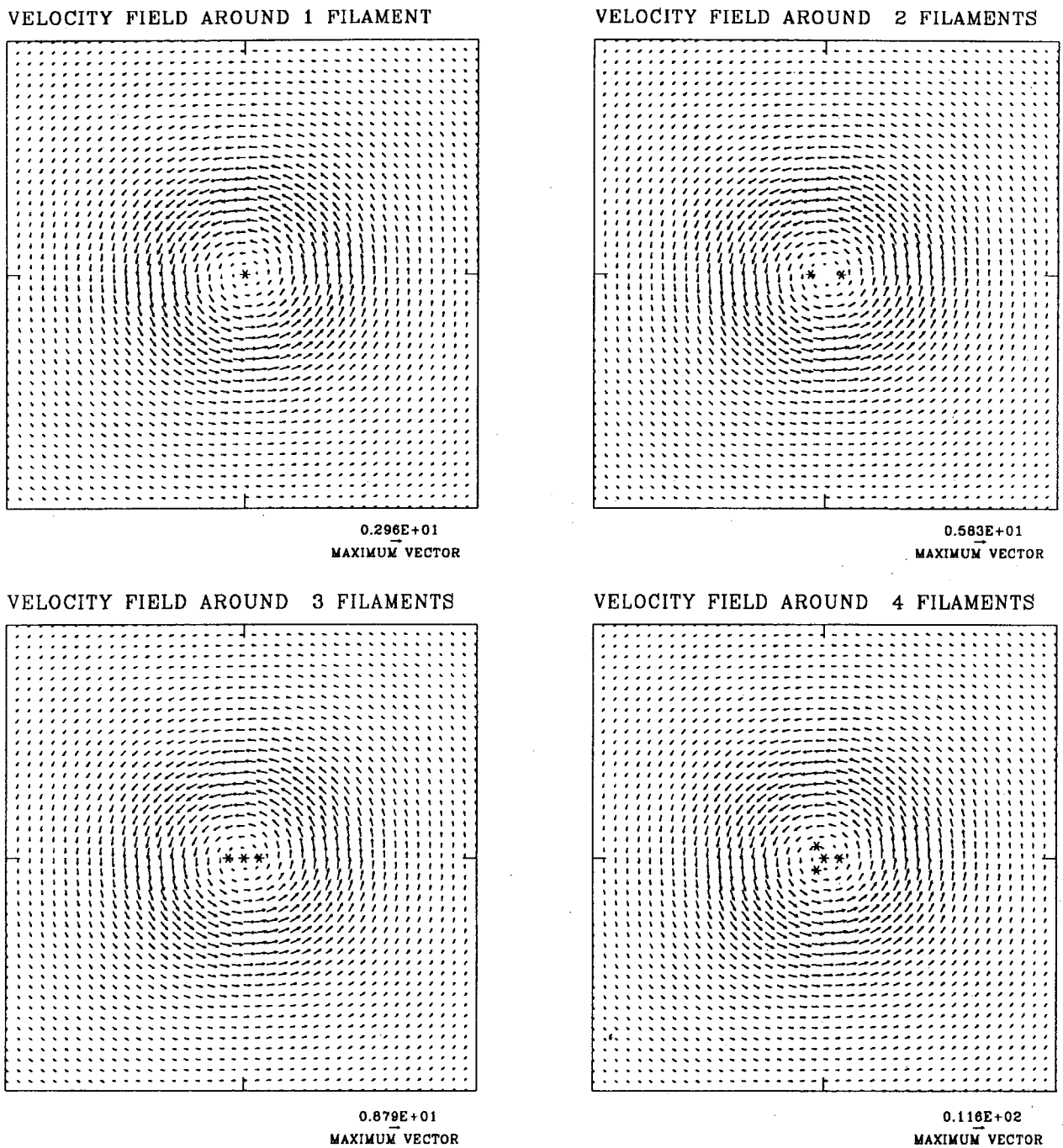

Figure 5.2. Cross-section velocity fields around various numbers of filaments. The symbol "*" indicates the position at which a filament crosses the section plane.

part. In the second method, for each filament, at each end, we copy the end segment N times and connect them to each other at the end. With both treatments, the three-dimensional vortex filament method scheme [equation (2.46)] can be modified as follows:

$$\mathbf{u}_\sigma(\mathbf{x},t) = -\frac{1}{4\pi}\sum_{m=1}^{M}\Gamma^{(m)}\sum_{j=1}^{N_m}\left[\frac{\mathbf{r}_j^{(m)}\times\delta\mathbf{l}_j^{(m)}}{(r_j^{(m)})^3}f(\frac{r_j^{(m)}}{\sigma})+\frac{\tilde{\mathbf{r}}_j^{(m)}\times\delta\mathbf{l}_j^{(m)}}{(\tilde{r}_j^{(m)})^3}f(\frac{\tilde{r}_j^{(m)}}{\sigma})+\frac{\bar{\mathbf{r}}_j^{(m)}\times\delta\mathbf{l}_j^{(m)}}{(\bar{r}_j^{(m)})^3}f(\frac{\bar{r}_j^{(m)}}{\sigma})\right]$$

where

$$\begin{aligned}
\mathbf{r}_j &= \mathbf{x}-\tfrac{1}{2}(\mathbf{x}_{j+1}+\mathbf{x}_j)\\
\tilde{\mathbf{r}}_j &= \mathbf{x}-\tfrac{1}{2}(\tilde{\mathbf{x}}_{j+1}+\tilde{\mathbf{x}}_j)\\
\bar{\mathbf{r}}_j &= \mathbf{x}-\tfrac{1}{2}(\bar{\mathbf{x}}_{j+1}+\bar{\mathbf{x}}_j)\\
r_j &= |\mathbf{r}_j|\\
\tilde{r}_j &= |\tilde{\mathbf{r}}_j|\\
\bar{r}_j &= |\bar{\mathbf{r}}_j|
\end{aligned}$$

For the periodic treatment,

$$\tilde{\mathbf{x}}_j = \begin{pmatrix} x_{N+1}+x_j-x_1 \\ y_j \\ z_j \end{pmatrix} \qquad \bar{\mathbf{x}}_j = \begin{pmatrix} x_1-(x_{N+1}-x_j) \\ y_j \\ z_j \end{pmatrix}$$

For the straight line extension,

$$\tilde{\mathbf{x}}_j = \begin{pmatrix} 2\tilde{x}_{j-1}-\tilde{x}_{j-2} \\ y_{N+1} \\ z_{N+1} \end{pmatrix} \qquad \bar{\mathbf{x}}_j = \begin{pmatrix} 2\bar{x}_{j-1}-\bar{x}_{j-2} \\ y_{N+1} \\ z_{N+1} \end{pmatrix}$$

where $\tilde{x}_1 = x_{N+1}$, $\tilde{x}_2 = 2x_{N+1}-x_N$, $\bar{x}_1 = x_1$, and $\bar{x}_2 = 2x_1 - x_2$. One should modify the scheme of straight line extension to deal with the situation of perturbed waves passing through the truncated ends. We suggest that in a computation, one follow the wave shape of interest, add new segments (or new grid) at the forward truncated end, and drop segments at the opposite end. We may call this a moving Lagrangian grid method. With this method, we can study the long-time behavior of a wave with limited computer memory space. The theoretical validity of this method is based on the observation that the behavior of a wave in a part of a vortex tube is governed mainly by this part of the vortex tube as long as the wave stays in the middle of the part and the truncated ends have been treated appropriately.

Chapter 6

Numerical Results

6.1 Goal and Experimental Design

We present our numerical results in this chapter. Our goal is to answer the following questions:

A. What are the effects on the accuracy of our vortex filament scheme of the choices of the numerical methods for solving the time evolution ordinary differential equation, the core functions, and the parameters?

B. What are the main factors causing numerical and physical vortex stretching?

Solitary wave propagation along a vortex tube is the physical-model problem we study here to provide answers for the above questions. Besides, solitary wave propagation along a vortex tube is an interesting research subject in itself. In particular, we would like also to know

C. Can a solitary wave propagate along a vortex tube for a long time?

The numerical and physical factors we are going to examine are the following:

1. the numerical method we choose to solve the time evolution ordinary differential equation;

2. the core function we construct to approximate the singular Biot-Savart kernel;

3. the core size σ defined at page 10, Chapter 2;

4. the time tolerance control constant C;

5. the number of filaments we use to simulate a vortex tube;

6. the distance between filaments;

7. the placement partten of filaments used to simulate a vortex tube;

8. the circulation Γ defined in equation (2.9); and

9. the torsion τ of the initial solitary wave data generated by equation (3.34).

In the list, the numerical method solving the time evolution ordinary differential equation, the core function, the time tolerance control constant C, and the number of filaments in the simulation of a vortex tube are clearly numerical factors. The accuracy of our results and the efficiency of our computation depend on these factors. The circulation Γ and the torsion τ of the initial solitary wave data are physical factors chosen in accordance with the physical phenomenon we attempt to simulate. The core size, the distance between filaments, and the placement partten of filaments have both numerical and physical significance, which we will explain in later sections.

To answer question **A**, we must examine the sensitivity of our numerical algorithm to the factors 1–8 listed above. In a computational result, a vortex tube stretching can be caused by either the computational inaccuracy or physical nature, or both. We will try to distinguish the different causes of the vortex stretching appearing in our results whenever it is possible. The answers to questions **A** to **B** will help us to answer question **C**.

In our vortex filament method, we split a segment in two if the length of this segment is larger than a predetermined positive number. When a filament starts stretching, the total arclength of the filament will grow very quickly. Thus, the number of segments for the filament grows quickly. Therefore, the total arclength is a direct measurement of vortex stretching. The total arclength is proportional to the total number of segments. Both numerical inaccuracy and the physical nature

of the vorticity field can cause vortex stretching in our numerical result. A vortex dynamic system is a highly unstable physical system. The numerical errors often introduce high-frequency perturbation waves with small torsion. Such waves easily cause violent stretching, as we will explain in a later section. This type of stretching is numerical stretching. The distinction between physical stretching and numerical stretching is not always possible. We usually must look at the geometric pattern of a perturbation wave and the location of the appearance of the wave to decide whether the perturbation wave is caused by numerical error or by physical instability and thus distinguish physical stretching from numerical stretching.

Computer memory limits the maximum number of segments per filament. If the number of segments for any filament exceeds the maximum value, our computation is stopped at that step. Thus, the smaller the number of steps for which our computation can be carried out, the more stretching we get for the simulated vortex tube. If a computation can be carried out till the allowed maximum step, then the total number of segments at that step reflects the stretching of the simulated vortex tube; the larger number of total segments implies more stretching in the computation.

The elapsed time is an indicator of the efficiency of our computation and a diagnostic of the accuracy of the computational results, because the slower growth of the elapsed time usually means that the time tolerance of each step is too small and thus may be not efficient. The rapid growth of the elapsed time means that the time tolerance of each step is large and may therefore cause inaccuracy.

The kinetic energy, total vorticity, and linear impulse are conserved quantities in an unbounded region for the Euler equations. Thus, in an unbounded region, a variation from the initial value of each of these quantities indicates error. However, as we have explained in the last section of Chapter 4, in the computation of a portion of a vortex tube, the case in which we are interested for all computations in this Chapter, the kinetic energy is approximately conserved only if perturbation waves are far from the truncated ends and linear impulse is not conserved at all as long as there are perturbations in the computed portion of a vortex tube. The total vorticity is conserved in all cases. Therefore, a variation from the initial value of the total vorticity indicates error. If the kinetic energy is conserved, we can be sure that our

computational results are accurate, but a variation of kinetic energy in the data does not necessaryly mean that the result is bad (inaccurate). We should not use linear impulse as a diagnostic of our numerical schemes in this case.

Therefore, we use the following quantities to measure the accuracy and the vortex stretching of our computational results:

1. the number of time steps in a computation;
2. the number of segments at the last computational step;
3. the total arclength at the last computational step;
4. the elapsed time, i.e., the accumulated sum of the time tolerances for each computational step from the beginning to the last step;
5. the total kinetic energy; and
6. the total vorticity.

In each numerical experiment, we generate vortex filament curves from equation (3.34) with predetermined parameters. Thus, there is a solitary wave in each initial vortex filament curve. Each curve approaches at infinity a line parallel to the x-axis. Therefore, we should see the solitary wave in each filament propagating along the x-axis. There are three parameters that may change the shape of the initial curve: (1) the torsion τ, (2) the parameter ν, and (3) the initial time parameter t_0, which merely determines the position of the initial solitary wave. The significance of the first two parameters has been explained in Section 2 of Chapter 3. In our computation, we record the measurements described above and the propagation behavior of the initial solitary wave for various combinations of the investigated factors. We will use tables to display the results in terms of the first four measurements: the total number of computational steps, the total number of segments at the last computational step, the total arclength at the last computational step, and the elapsed time. We will give figures to illustrate three measurements if needed. Finally, we will analyze the results obtained and try to find answers for our questions.

6.2 Numerical Factors

In this section we examine the factors that affect the accuracy of our computation and try to find a reasonable combination of choices of the factors that can give accurate results. The stretching now is a measurement of accuracy of our computation; that is, more stretching indicates more error in computation because these examined factors have no physical significance. These factors are the number of filaments used to simulate a vortex tube, the numerical method for solving the time evolution ordinary differential equation, the core function, and the time tolerance control constant C.

We start the discussion with the number of filaments used to simulate a vortex tube. In Chapter 3, we derived the solitary wave solution for the localized induction approximation of a thin vortex tube. To understand a wave motion in an inviscid incompressible flow, we would like to determine the propagation behavior of the solitary wave in the velocity field induced by a thin vortex tube governed by the Biot-Savart law. A single filament can be viewed as a thin vortex tube. However, the lack of change of core structure in the cross section of a filament makes the simulation of a thin vortex tube by a single filament physically unreasonable, because the shape of a vortex tube core is not preserved (see [56, 57, 59, 49]). Moreover, for a "fat" vortex tube, it is unreasonable to approximate the tube by one filament with large core size because, mathematically, it is unreasonable to approximate the singular kernel $K(\mathbf{x})$ given at Chapter 2 by the smoothed one $K_\sigma(\mathbf{x})$ with large σ— the core size. The convergence theory shows that to have a better approximation for a vortex method, one should choose the time tolerance and the spatial-mesh size as a function of the gradients of vorticity. The bigger the gradients of the vorticity, the smaller the time tolerance and the spatial mesh size. The several filament simulation of a vortex tube seems a good way to solve these problems. Note that when we increase the number of filaments, we should decrease the circulation of each filament to preserve the total circulation of the simulated vortex tube. Nevertheless, the one filament simulations of a thin vortex tube give us some useful information on vortex stretching and how vortex filament methods respond to various parameters. Our

Table 6.1. The total number of computational steps, the total number of segments at the last computational step, the total arclength at the last computational step, and the elapsed time for various core functions and numerical schemes for solving ODE with one filament.

1 filament with core size $\sigma = 0.4$, $t_0 = -0.1$, $C = 0.05$, $\Gamma = 5.0$ and periodic treatment at truncated ends					
Methods	**Core**	**Steps**	**At the Last Step**		
			No. Seg.	**Time**	**Arclength**
Euler	1	200	752	3.83	23.74
	2	200	804	3.44	26.25
	3	157	993	2.10	34.05
	4	124	979	1.79	34.30
Heun	1	200	416	5.32	10.84
	2	200	408	4.68	10.75
	3	200	588	3.02	18.58
	4	200	547	2.90	17.31
RK4	1	200	422	5.68	10.76
	2	200	406	4.70	10.69
	3	200	521	3.08	16.30
	4	200	503	2.92	15.23

studies of vortex filament methods and vortex stretching begin with the one filament simulations of a thin vortex tube; therefore, we should provide the data of the one filament simulations of a thin vortex tube.

Theoretically, computational accuracy will increase as a vortex tube is simulated with an increasing number of filaments. However the simulations of our physical-model problem require long filaments and, therefore, many segments for each filament and long time computations to obtain enough information to understand the questions raised at beginning of this Chapter. The cost of computation and the capacity of current computer memories do not permit us to simulate a vortex tube with many filaments. We will provide results of one filament simulations and three or four filament simulations for some of the following computational experiments.

In this section, all initial data for our computation are generated by equation (2.33) with $\tau = 3.0, \nu = 2.0$. The length ds of each segment is 0.04 initially. A segment must split in two if its length is longer than 0.05. The computation is terminated if there is a filament with more than 1000 segments.

We examine the following numerical methods for solving the time evolution ordinary differential equation: (1) the first-order Euler's method, (2) the second-order modified trapezoidal method (the second-order Heun's method), and (3) the fourth order Runge-Kutta method (RK4). These schemes are given on page 14, Chapter 2. The core functions we examine are the following:

$$\begin{aligned}
&\text{Core } 1: \quad 1 - e^{-r^3};\\
&\text{Core } 2: \quad \tanh r^3;\\
&\text{Core } 3: \quad 1 + (-1 + \tfrac{3}{2}r^3)e^{-r^3};\\
&\text{Core } 4: \quad \tanh r^3 + \tfrac{3}{2}r^3 \operatorname{sech}^2 r^3.
\end{aligned}$$

We make runs with each numerical method and each core function for one filament. In Table 6.1, we list the total number of computational steps, the total number of segments at the last computational step, the total arclength at the last computational step, and the elapsed time. In Table 6.2, we list the results from the runs with the second-order Heun's method and the fourth-order Runge-Kutta method and for several core functions for three filaments. We also give, in Table 6.2, the comparison results for two treatments of the truncated ends: periodicity and straight line extension.

From Table 6.1 we can see that the vortex filament method is much less accurate with the first-order Euler method for solving the time evolution ordinary differential equation than with the other two methods. Therefore, we did not make runs for three filaments with the Euler method solving the time evolution ordinary differential equation. There is no great difference between the second-order modified trapezoidal method and the fourth-order Runge-Kutta method. We will use the fourth-order Runge-Kutta method for the rest of our runs in this Chapter.

Both Table 6.1 and Table 6.2 show that the various core functions produce different results. We can not really see, however, which core function gives us a more

Table 6.2. The total number of computational steps, the total number of segments at the last computational step, the total arclength at the last computational step, and the elapsed time for various core functions, numerical schemes for solving the time evolution ordinary differential equation, and extension methods at truncated ends with three filaments.

3 filaments with core size $\sigma = 0.4$, $t_0 = -0.1$, $C = 0.05$, $\Gamma = 5.0$ 200 time steps					
Methods	**Core**	**Extension Method at Ends**	**At the Last Step**		
			No. Seg.	**Time**	**Arclength**
Heun	1	period	1417	2.000	38.98212
		straight lines	1428	2.000	38.96558
	2	period	1348	1.860	35.99836
		straight lines	1362	1.885	36.36842
	3	period	1385	1.010	42.93497
		straight lines	1384	1.010	42.98206
	4	period	1179	0.710	36.72602
		straight lines	1179	0.710	36.72324
RK4	1	period	1385	2.000	37.75273
		straight lines	1391	2.000	37.78472
	2	period	1343	1.945	35.32752
		straight lines	1363	2.000	35.83455
	3	period	1390	1.015	42.82489
		straight lines	1387	1.015	42.85716
	4	period	1184	0.715	36.98255
		straight lines	1184	0.715	36.97923

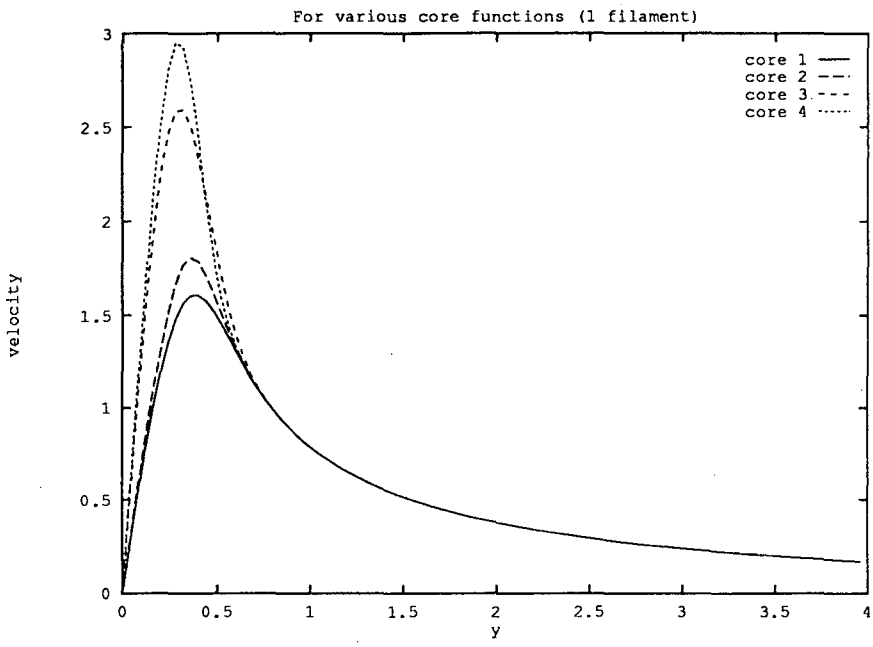

Figure 6.1. The velocity distribution on a plane perpendicular to a straight vortex tube for various core functions.

accurate solution because the behavior of a core function is governed by the core size. Each core function responds to a same value of core size differently, as can be seen from Figure 6.1.

From Table 6.2 we see that the treatment of the truncated ends makes very little difference to our computational results. However, different treatments at the ends will cause a great difference if the perturbation has traveled to the ends. In the runs made for Table 6.2, we did not compute long enough to see the difference in the results.

At the suggestion of Hald [36], we plot the relationship between arclength and computational step at a given elapsed time in Figure 6.2 for various numerical methods and core functions. The data are from the same runs that give the results presented in Table 6.1 and Table 6.2. With a given core function, the number of computational steps and the arclength produced by various numerical methods should be close to each other at the same elapsed time if all of the numerical methods give accurate solutions. Thus from Figure 6.2 (a), we can see immediately that results

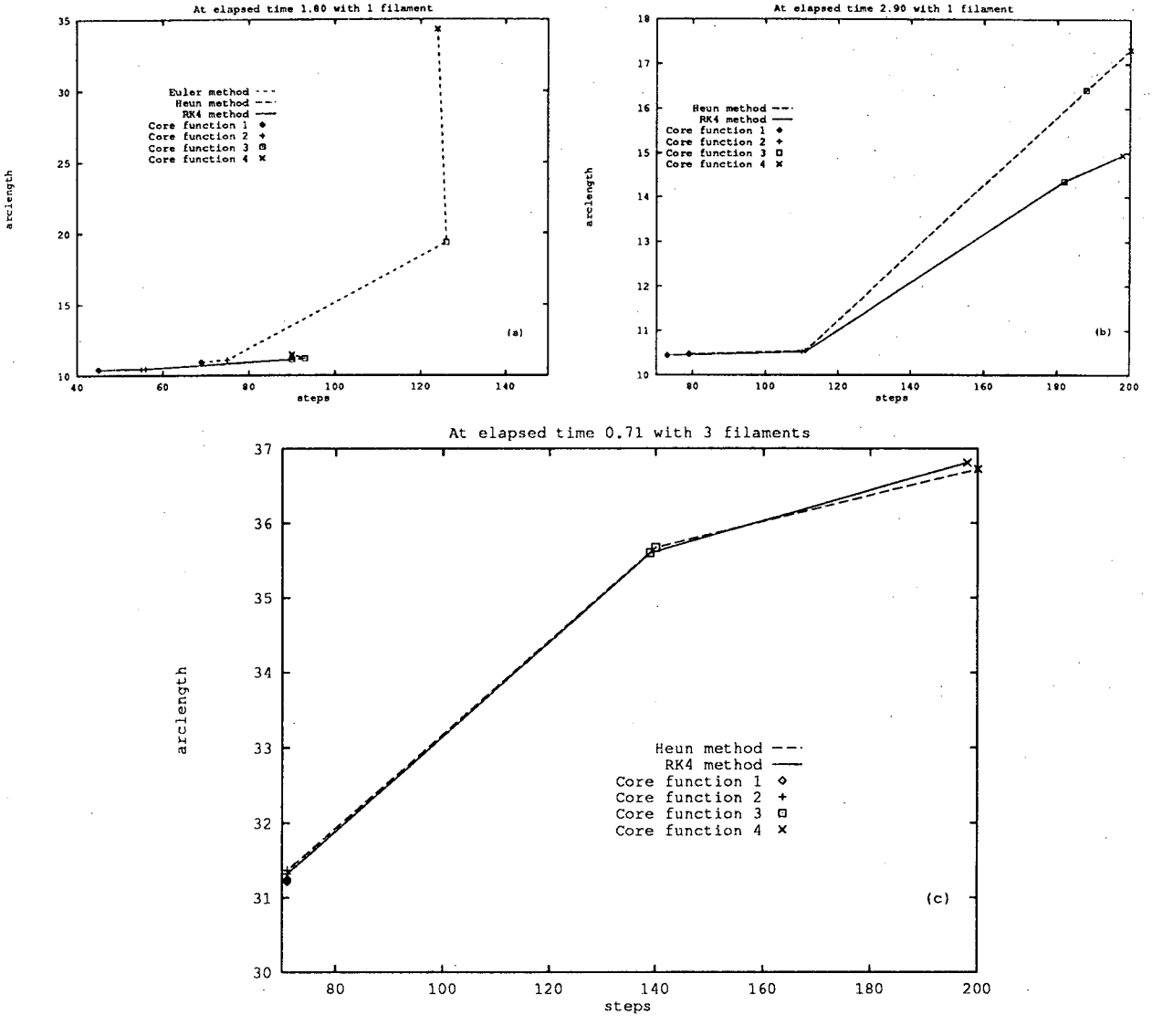

Figure 6.2. The relationships between arclength and computational steps at the given elapsed times for various numerical methods and core functions.

produced with the first-order Euler method are inaccurate. The core functions behave differently, as we expected, with one exception: in Figure 6.2 (c) the results with core function 1 and core function 2 are in good agreement because of the short time span. For shorter time span, the two method—the second-order modified trapezoidal method and the fourth-order Runge-Kutta method—give close agreement. Figure 6.2 (b) may indicate that the fourth-order Runge-Kutta method could be better than the second-order modified trapezoidal method for longer time spans.

The total kinetic energy is approximately conserved for all runs except for the runs made with the first-order Euler method. With the second-order and the fourth-order numerical methods, the percentages P of maximum variation from initial total kinetic energy, where

$$P = \frac{|maximum\ \ total\ \ energy - initial\ \ total\ \ energy|}{initial\ \ total\ \ energy} \times 100$$

are

$$\left.\begin{array}{ll} 6.2 \sim 6.5 & \text{for core 1 and 2,} \\ 13 \sim 14 & \text{for core 3,} \\ 18 \sim 19 & \text{for core 4,} \end{array}\right\} \text{with one filament computation}$$

$7.3 \sim 10$ for all four core functions with three filaments

With the first-order Euler method, the percentage is $20 \sim 30$. Similarly, to measure the variation of the total vorticity, we compute the percentages with the following formulations:

$$P_{total\ vorticity} = \frac{||total\ vorticity\ with\ max\ magnitude\ -\ initial\ total\ vorticity||}{||initial\ total\ vorticity||} \times 100$$

The percentages of variation for total vorticity are $0.02 \sim 0.1$ for all cases. Thus the total vorticity is well conserved. Figure 6.3 shows how the diagnostic quantities—the total kinetic energy and the total vorticity—typically behave in the computation.

From equation (2.39),

$$\Delta t \max_j |\mathbf{u}_j^n| \leq C$$

The time tolerance control constant C is one of the factors determining the accuracy of our computational results. However, if C is too small, the computational cost will

Table 6.3. The total number of computational steps, the total number of segments at the last computational step, the total arclength at the last computational step, and the elapsed time for various time tolerance control constants C.

4 filaments with core function 4, $\Gamma = 5.0$, the 4th order Runge-Kutta method, core size $\sigma = 0.2$, $t_0 = -0.2$, distance between filaments = 0.05, and periodic treatment at truncated ends				
C	Steps	At the Last Step		
		No. Seg.	Time	Arclength
0.02	250	1709	0.15750	64.04793
0.03	250	1778	0.24875	64.27265
0.04	250	1879	0.31375	65.23524
0.05	250	1934	0.33125	66.26626
0.06	250	3518	0.43500	119.03595
0.07	175	3624	0.43500	122.79700
0.10	162	3647	0.42500	124.47843
0.02	250	1709	0.15750	64.04793
0.03	132	1710	0.15750	64.04794
0.04	125	1709	0.15750	64.04791
0.05	111	1710	0.15750	64.04775
0.06	65	1710	0.15625	64.04724
0.07	63	1710	0.15750	64.04726
0.10	55	1713	0.15750	64.04207

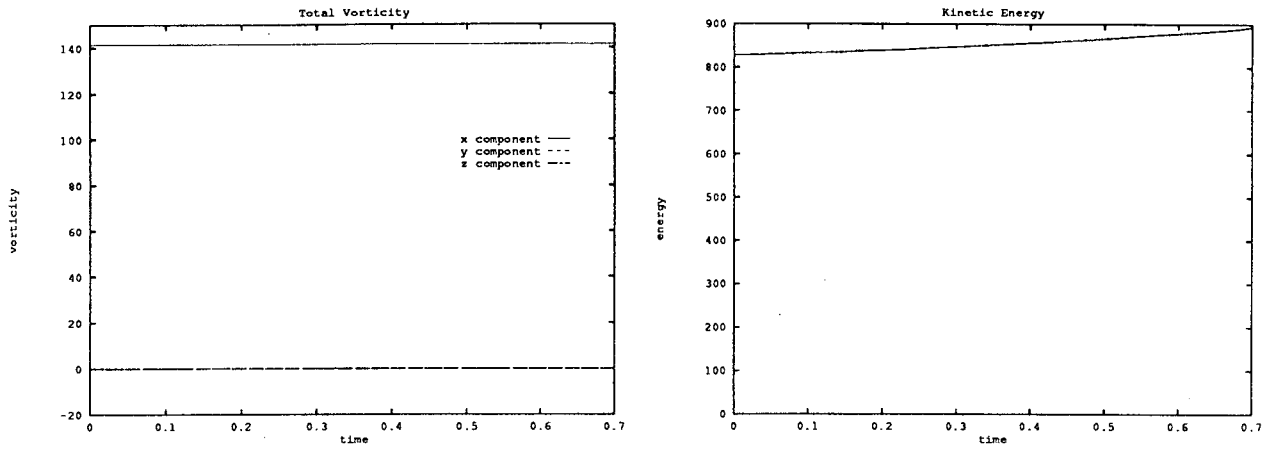

Figure 6.3. The diagnostics of computation for three filaments with RK4 and core function 4.

be quite high. In Table 6.3 we see that when we increase C, the elapsed time, the number of segments and arclength at the last computational step are increased, and the number of time steps to reach a given value of elapsed time is decreased. The dramatic increase in the number of segments and arclength at the last computational step and the decrease of the number of time steps to reach the elapsed time 0.1575 at $C = 0.06$ indicate that the computational results with the paramenters given at head of Table 6.3 are not accurate for $C > 0.05$. We should note that the choice of C depends on the maximum amplitude of the velocity on the filaments, and therefore depends on the circulation Γ.

6.3 The Circulation Γ and Factors Affecting the Placement of Filaments

The circulation Γ of a vortex tube is a physical factor. However, the circulation Γ for each filament used to simulate a given vortex tube is determined by the circulation of the vortex tube and the number of filaments used in the simulation. We should decrease the circulation Γ of each filament when we increase the number of filaments in the simulation to match the correct circulation of the simulated vor-

Table 6.4. The total number of computational steps, the total number of segments at the last computational step, the total arclength at the last computational step, and the elapsed time for various circulations Γ and distances between filaments.

4 filaments with core function 4, $C = 0.05$, the 4th order Runge-Kutta method, core size $\sigma = 0.2$, $t_0 = -0.2$, and periodic treatment at truncated ends					
Γ	Dist. between Filaments	Steps	At the Last Step		
			No. Seg.	Time	Arclength
1.0		250	2616	2.05500	90.07765
3.0	0.05	250	2163	0.62750	74.81861
5.0		250	1934	0.33125	66.26626
	0.01	250	2295	0.50375	78.91651
	0.02	250	2009	0.45000	68.28120
5.0	0.05	250	1934	0.33125	66.26626
	0.08	250	2027	0.31375	67.64354
	0.10	239	3337	0.29875	110.62826
	0.20	101	3261	0.17625	114.06007

tex tube. From Table 6.4 we see that with the other factors constant, the number of segments, the elapsed time, and arclength at the last step are increased when we increase Γ for each filament. This is understandable because, from equation (2.46), increasing Γ will increases the amplitude of velocity, whereas, from equation (2.39), increasing the amplitude of the velocity for given constant C will decrease the time-step tolerance Δt. Thus, one should choose the time-step tolerance control constant C after Γ is determined to get accurate results with lowest computational cost.

The change of distance between filaments (in multifilament simulations) could produce different velocity distribution, as illustrated in Figure 6.5 for four filaments and Figure 6.4 for two filaments. Table 6.4 shows that increasing the distance between filaments will decrease the elapsed time at the last step but will not give a monotonical variation of the number of segments and arclength at the last time step. For a thin vortex tube, with smaller distance between filaments, the results will be closer to the results obtained with a one filament simulation with the parameters

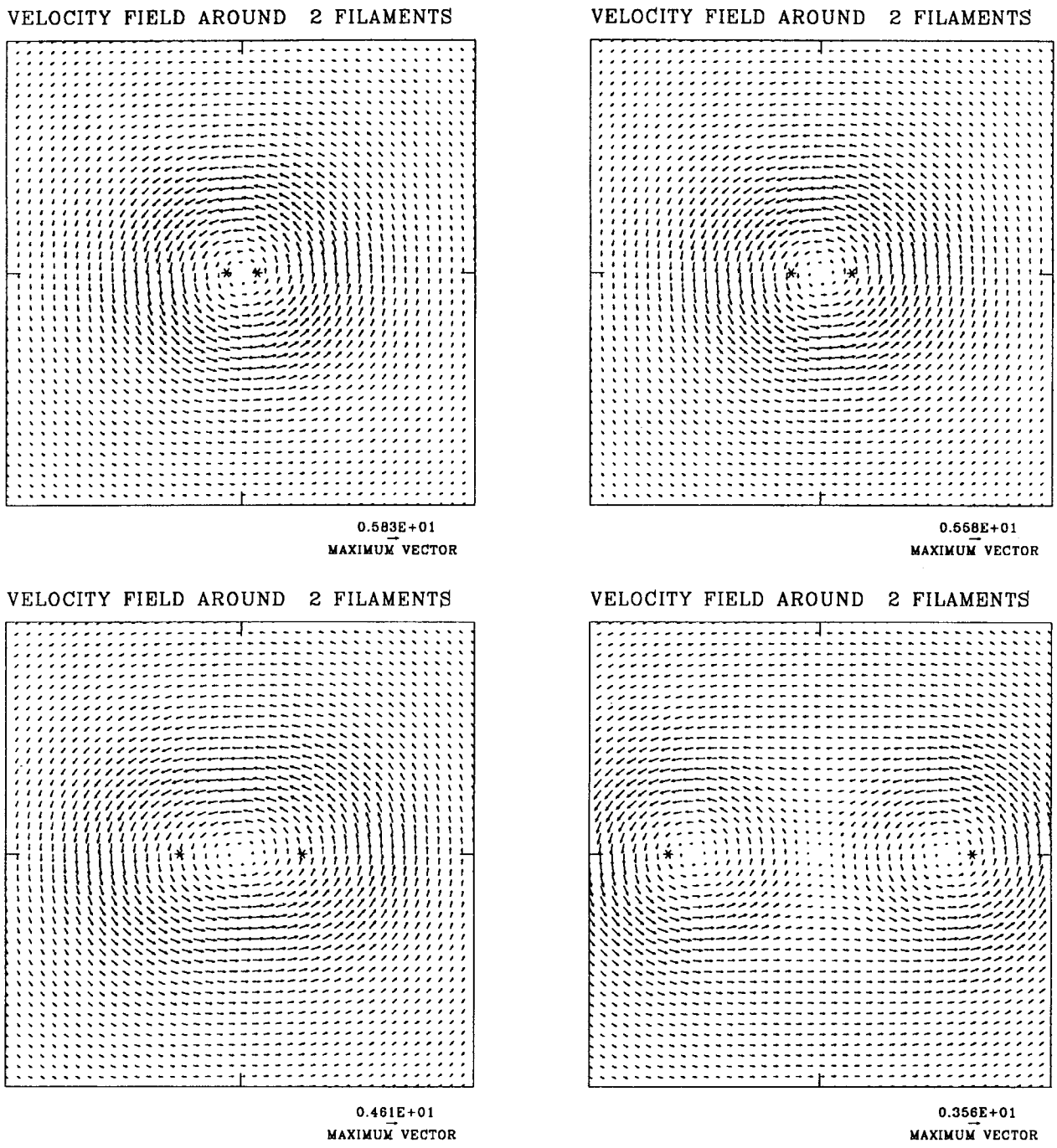

Figure 6.4. Cross-section velocity fields around 2 filaments with distances 0.1, 0.2, 0.4, and 1.0, respectively. The symbol "*" indicates the position at which a filament crosses the section plane.

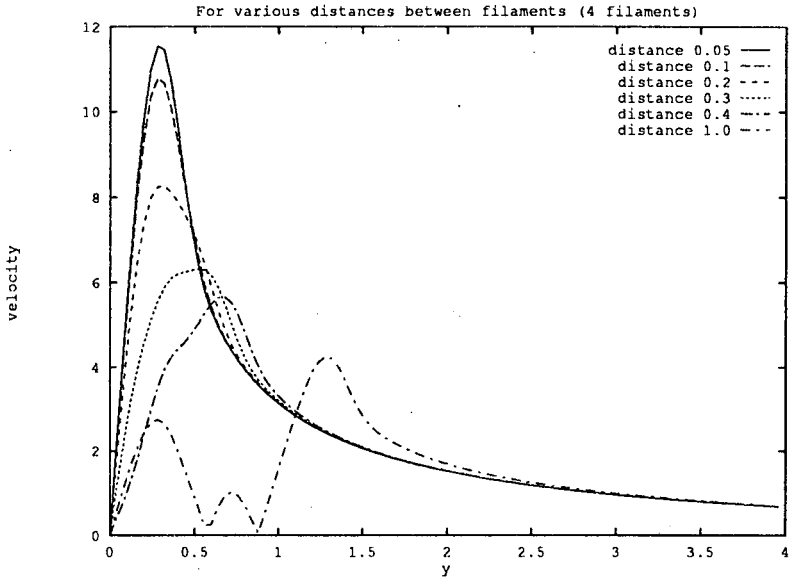

Figure 6.5. The velocity distribution on a plane perpendicular to a straight vortex tube changes as the distance between filaments increases, with other parameters constant.

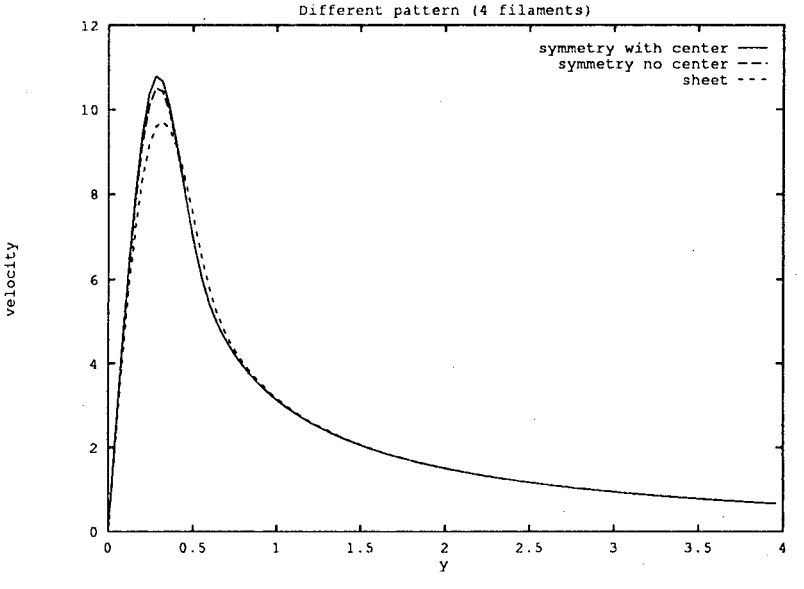

Figure 6.6. The velocity distribution on a plane perpendicular to a straight vortex tube for various placement partten of filaments.

describing the same simulated vortex tube. With the distance increasing and passing a certain limit, we find that, in the computational results, the vortex-line stretching happens sooner and more violently, as can be seen in Table 6.4. For each set of given parameters, there is a critical value for the distance between filaments at which the least stretching happens in the computational result. In Table 6.4, this value is obtained around 0.05. We should note that with the same set of parameters given in Table 6.4, for the one filament computation in Table 6.2, the higher stretching is seen from the computational result. Thus, with distance between filaments smaller than the critical value, 0.05, in Table 6.4, more stretching will be seen in a computational result because that the several filaments simulation behaves more like the one filament simulation with smaller distance between filaments. Therefore, to avoid higher stretching in a simulation of a vortex tube by a bundle of filaments, we should choose the distance between filaments close to certain critical value. Note that vortex stretching could be physical. Therefore, it may not be reasonable to put our effort into eliminating all stretching.

With fewer filaments in the simulation, a change in the placement partten of filaments does not have a strong impact on the velocity distribution, as shown in Figure 6.6. However, we should note that with many filaments, the placement partten of filaments does affect the velocity distribution; the pattern must match the vorticity field we wish to model.

6.4 Core Size

As discussed in Section 2 of this chapter, the core size should not be too large because of the mathematical unreasonableness to approximate the singular kernel $K(\mathbf{x})$ by $K_\sigma(\mathbf{x})$ with large core size σ. The core size is an important numerical factor. However, we could think of core size as the thickness of our filaments, and we could consider that the core size has real a physical meaning for a thin vortex filament. We would like to find the reasonable numerical range of choices of core size and the response of our computational results to these choices.

Figure 6.7 shows that, with various core sizes, the induced velocity distribu-

Table 6.5. The total number of computational steps, the total number of segments at the last computational step, the total arclength at the last computational step, and the elapsed time for increasing core size with one filament.

1 filaments with $\Gamma = 5.0$, $C = 0.05$, $t_0 = -0.2$, the 4th order Runge-Kutta method, and periodic treatment at truncated ends					
Core Functions	Core Size	Steps	At the Last Step		
			No. Seg.	Time	Arclength
core 1	0.05	88	878	0.3975	31.29
	0.08	237	963	1.785	34.16
	0.09	238	978	1.9025	33.67
	0.095	241	983	1.945	33.78
	0.10	240	972	1.975	33.34
	0.11	234	987	2.025	34.03
	0.15	193	979	2.03	34.50
	0.20	142	977	2.01	33.86
	0.25	146	993	2.22	34.41
	0.30	218	992	4.04	33.21
	0.35	250	636	5.34	19.03
	0.40	250	602	6.64	17.00
core 4	0.05	61	953	0.14063	33.90
	0.08	51	948	0.1725	33.27
	0.09	168	980	0.8175	32.02
	0.10	250	502	1.655	16.52
	0.15	250	512	1.99	16.70
	0.20	250	813	2.18	28.18
	0.25	213	991	2.16	34.12
	0.30	157	993	2.09	34.51
	0.35	149	982	2.15	34.09
	0.40	237	997	3.29	33.05
	0.45	250	685	4.23	21.47
	0.50	250	602	5.00	16.83
	0.55	250	575	5.20	16.56
	0.60	250	695	10.00	16.64

Table 6.6. The total number of computational steps, the total number of segments at the last computational step, the total arclength at the last computational step, and the elapsed time for increasing core size with four filaments.

4 filaments with core function 4, the 4th order Runge-Kutta method, $\Gamma = 5.0$, $C = 0.05$, $t_0 = -0.2$, distance between filaments $= 0.05$, and periodic treatment at truncated ends				
Core size	**Steps**	**At the Last Step**		
		No. Seg.	**Time**	**Arclength**
0.10	142	2798	0.08937	97.46644
0.15	250	2113	0.31250	69.65556
0.20	250	1934	0.33125	66.26626
0.25	250	2264	0.435	81.34734
0.30	236	3314	0.5975	113.05148
0.40	250	2519	0.7075	84.75277
0.50	250	2451	1.25	72.87434
0.55	250	2257	1.25	67.20053
0.60	250	2219	1.29	66.05207

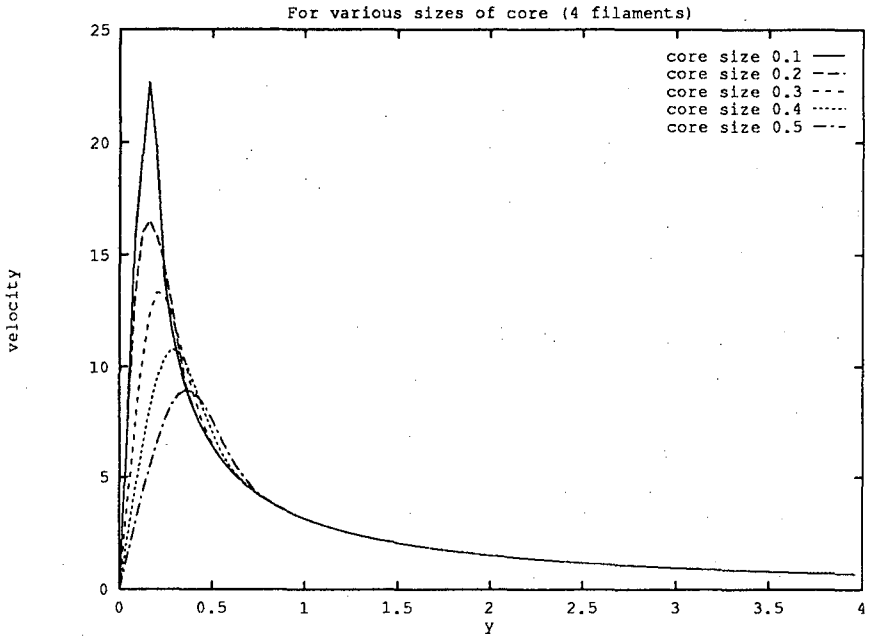

Figure 6.7. The velocity distributions on a plane perpendicular to a straight vortex tube for various core sizes.

tions vary. In Table 6.5 and Table 6.6, we display the results of the total number of time steps, the number of total segments at the last computational step, the elapsed time, and the total arclength at the last computational step for runs made with various core sizes. The maximum number of computational steps is 250 for each run. The maximum number of segments for each filament is 1000. Therefore, a run stopped with fewer than 250 computing steps indicates that a violent stretching occurred. The smaller the total steps for a run, the sooner a violent stretching occurs. If a run is stopped with a total of 250 computing steps, the total number of segments measures the degree and the rate of stretching for each run. The vortex stretching behavior can be better illustrated by figures (see Figure 6.8 for the one filament simulation). It is interesting to see from Tables 6.5 and 6.6 that the rate of stretching does not respond monotonically to the core size. Such a phenomenon is shown directly in Table 6.6 in terms of arclength for runs with core function 4 for a simulation with a single filament and for runs made with four filaments in Table 6.6. In Table 6.5, for core function 1 and a single filament, the arclengths at the last step are close to each

other for different cases because the violent stretchings occur before the 250th computational step for most runs. Krasny [50] has reported the nonmonotonical response to core sizes for a two-dimensional blob method with a different core structure from the one used here. In Table 6.5, for core function 4 with a single filament, we see that nonstretching wave propagation occurs with core sizes in two regions around 0.1 and 0.55. In Table 6.6, the nonstretching wave propagation occurs with core sizes in two other regions around 0.2 and 0.6. In Table 6.5, the values of arclength are close to each other for those runs terminated before the 250th step. Thus, the number of segments grows rapidly once stretching starts in a run. From both Tables 6.5 and 6.6, we see that the total elapsed time increases when we increase the core size. It means that the time tolerance Δt for each step determined by equation (2.39) is larger for larger core size; that is, the maximum amplitude of the velocity increases when we increase the core size, as shown by Figure 6.7.

Figure 6.8 shows the geometric shapes of waves propagating in one filament for various core sizes. The data correspond to the results in Table 6.5 with core function 4. In all the runs, the initial solitary wave can propagate without significantly changing shape for certain computational steps, then either splits into several waves for those no violent stretching runs or starts to stretch with different geometric shapes depending on the core sizes and other parameters. For smaller core size, the propagation of the initial solitary wave is closer the analytic solution of LIA in terms of the phase of the wave. For a core size equal to 0.55, we see a smaller wave split from the original one with a stable shape propagating in the positive direction on the x-axis. Later, several waves split from the original wave and move off. When the core size is 0.35, stretching happens soon after some perturbation appears in front of the initial wave. A similar phenomenon occurs in the run made with core size 0.2, but the geometric structure of the stretching is quite different. All stretching happens in a narrow region in the x-direction; that is, the stretching does not spread along the x-direction. In the case of a core size $\sigma = 0.2$, a long arm comes out from the filament and wraps around the axis on which the filament is lying. When we decrease the core size from 0.4 to 0.2, the geometric structure of the stretching varies from a spiral structure to a two-arm structure, at a core size of around 0.3, and changes back

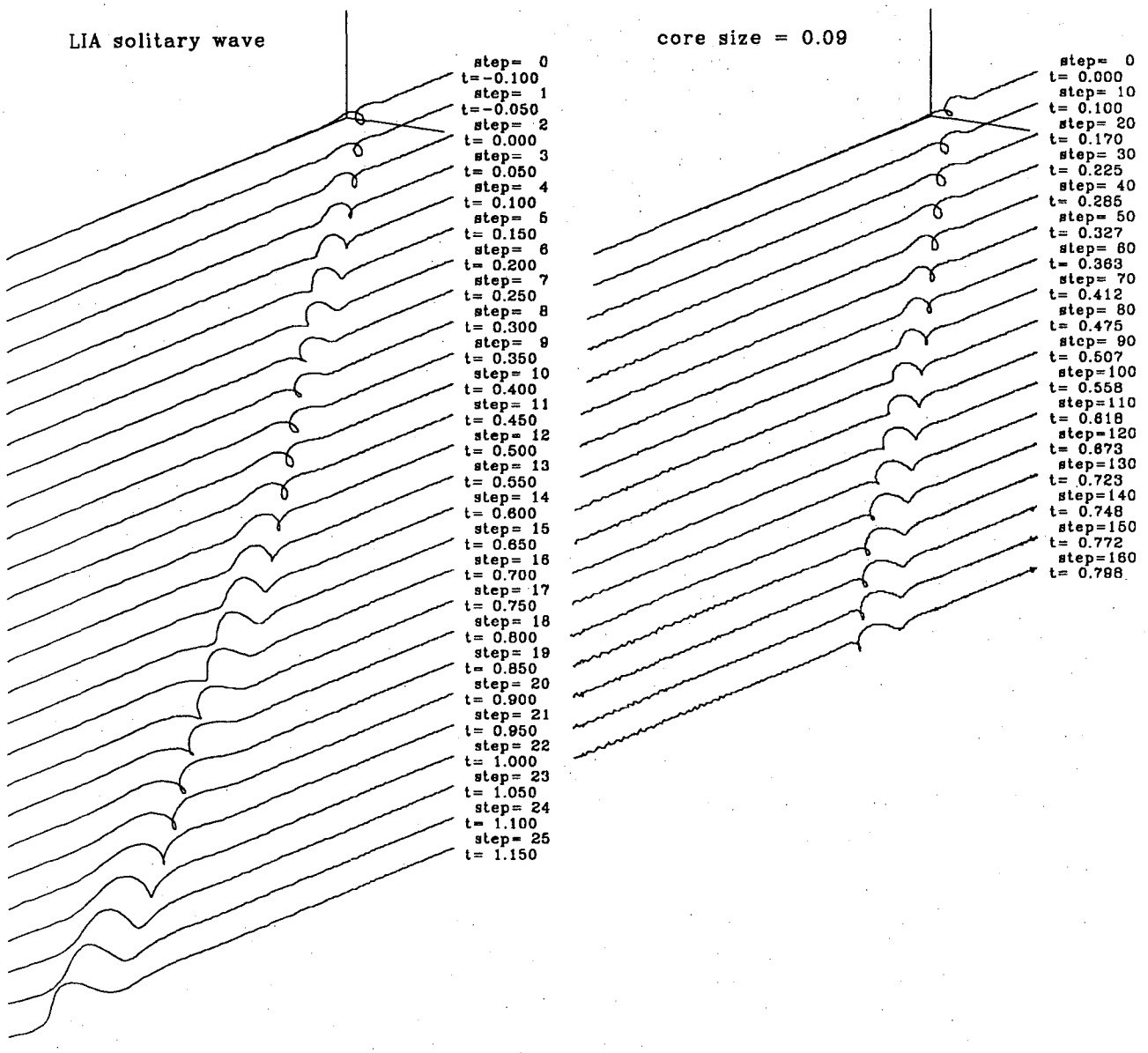
LIA solitary wave
step= 0
t=-0.100
step= 1
t=-0.050
step= 2
t= 0.000
step= 3
t= 0.050
step= 4
t= 0.100
step= 5
t= 0.150
step= 6
t= 0.200
step= 7
t= 0.250
step= 8
t= 0.300
step= 9
t= 0.350
step= 10
t= 0.400
step= 11
t= 0.450
step= 12
t= 0.500
step= 13
t= 0.550
step= 14
t= 0.600
step= 15
t= 0.650
step= 16
t= 0.700
step= 17
t= 0.750
step= 18
t= 0.800
step= 19
t= 0.850
step= 20
t= 0.900
step= 21
t= 0.950
step= 22
t= 1.000
step= 23
t= 1.050
step= 24
t= 1.100
step= 25
t= 1.150
core size = 0.09
step= 0
t= 0.000
step= 10
t= 0.100
step= 20
t= 0.170
step= 30
t= 0.225
step= 40
t= 0.286
step= 50
t= 0.327
step= 60
t= 0.363
step= 70
t= 0.412
step= 80
t= 0.475
step= 90
t= 0.507
step=100
t= 0.558
step=110
t= 0.618
step=120
t= 0.673
step=130
t= 0.723
step=140
t= 0.748
step=150
t= 0.772
step=160
t= 0.798

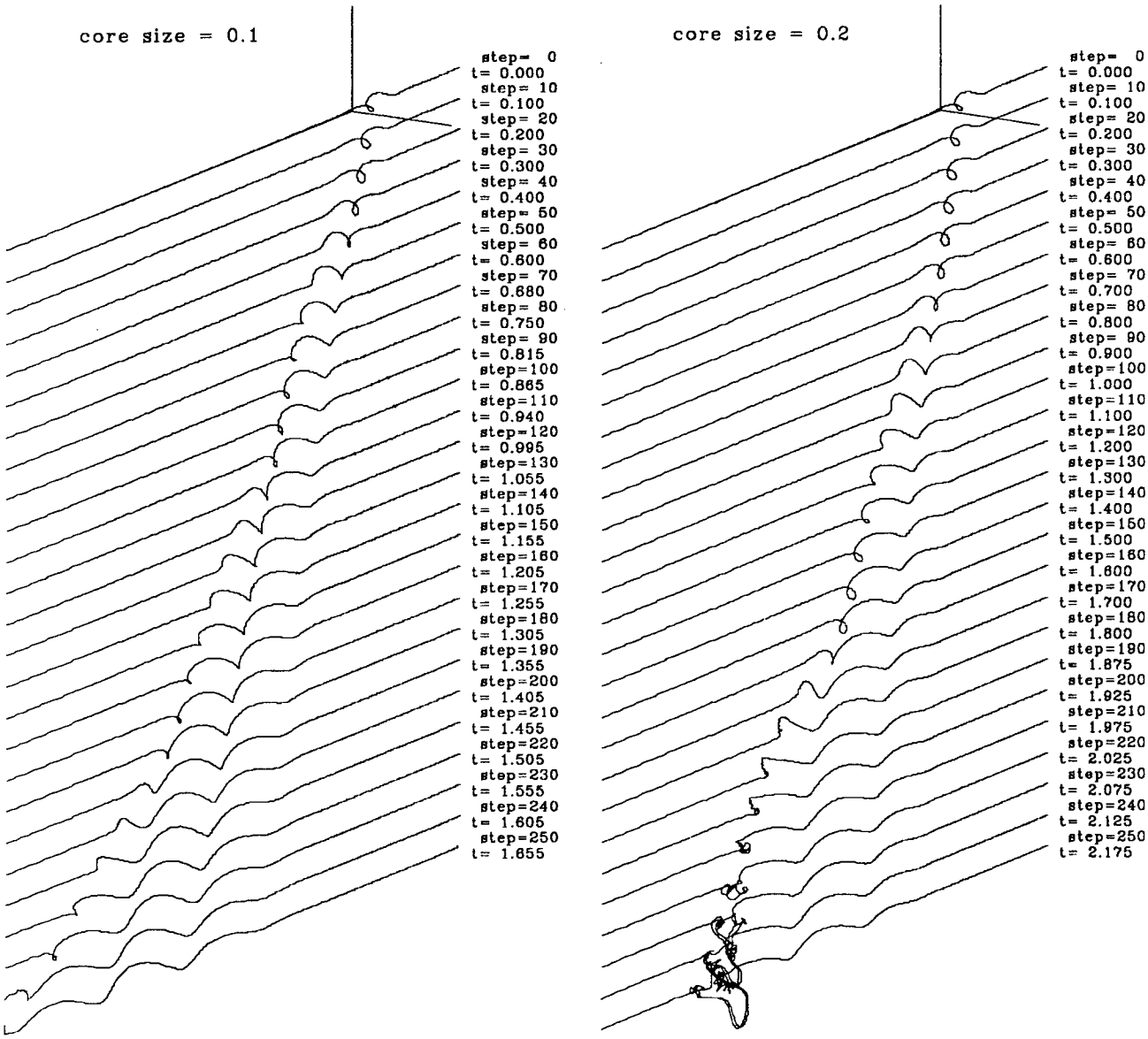
core size = 0.1
step= 0
t= 0.000
step= 10
t= 0.100
step= 20
t= 0.200
step= 30
t= 0.300
step= 40
t= 0.400
step= 50
t= 0.500
step= 60
t= 0.600
step= 70
t= 0.680
step= 80
t= 0.750
step= 90
t= 0.815
step=100
t= 0.865
step=110
t= 0.940
step=120
t= 0.995
step=130
t= 1.055
step=140
t= 1.105
step=150
t= 1.155
step=160
t= 1.205
step=170
t= 1.255
step=180
t= 1.305
step=190
t= 1.355
step=200
t= 1.405
step=210
t= 1.455
step=220
t= 1.505
step=230
t= 1.555
step=240
t= 1.605
step=250
t= 1.655
core size = 0.2
step= 0
t= 0.000
step= 10
t= 0.100
step= 20
t= 0.200
step= 30
t= 0.300
step= 40
t= 0.400
step= 50
t= 0.500
step= 60
t= 0.600
step= 70
t= 0.700
step= 80
t= 0.800
step= 90
t= 0.900
step=100
t= 1.000
step=110
t= 1.100
step=120
t= 1.200
step=130
t= 1.300
step=140
t= 1.400
step=150
t= 1.500
step=160
t= 1.600
step=170
t= 1.700
step=180
t= 1.800
step=190
t= 1.875
step=200
t= 1.925
step=210
t= 1.975
step=220
t= 2.025
step=230
t= 2.075
step=240
t= 2.125
step=250
t= 2.175

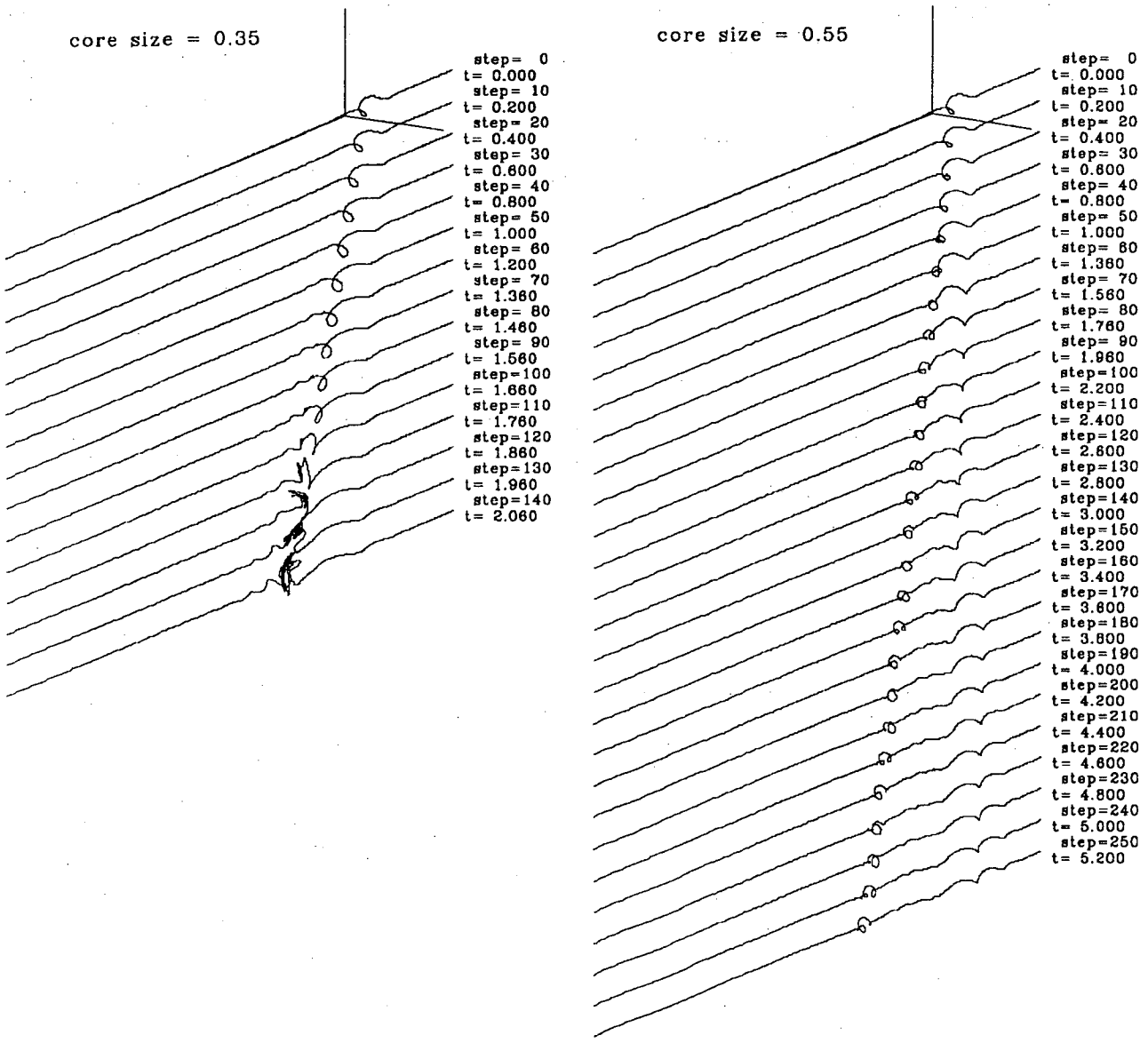

Figure 6.8. Perspective views of wave propagating in filaments with various core sizes

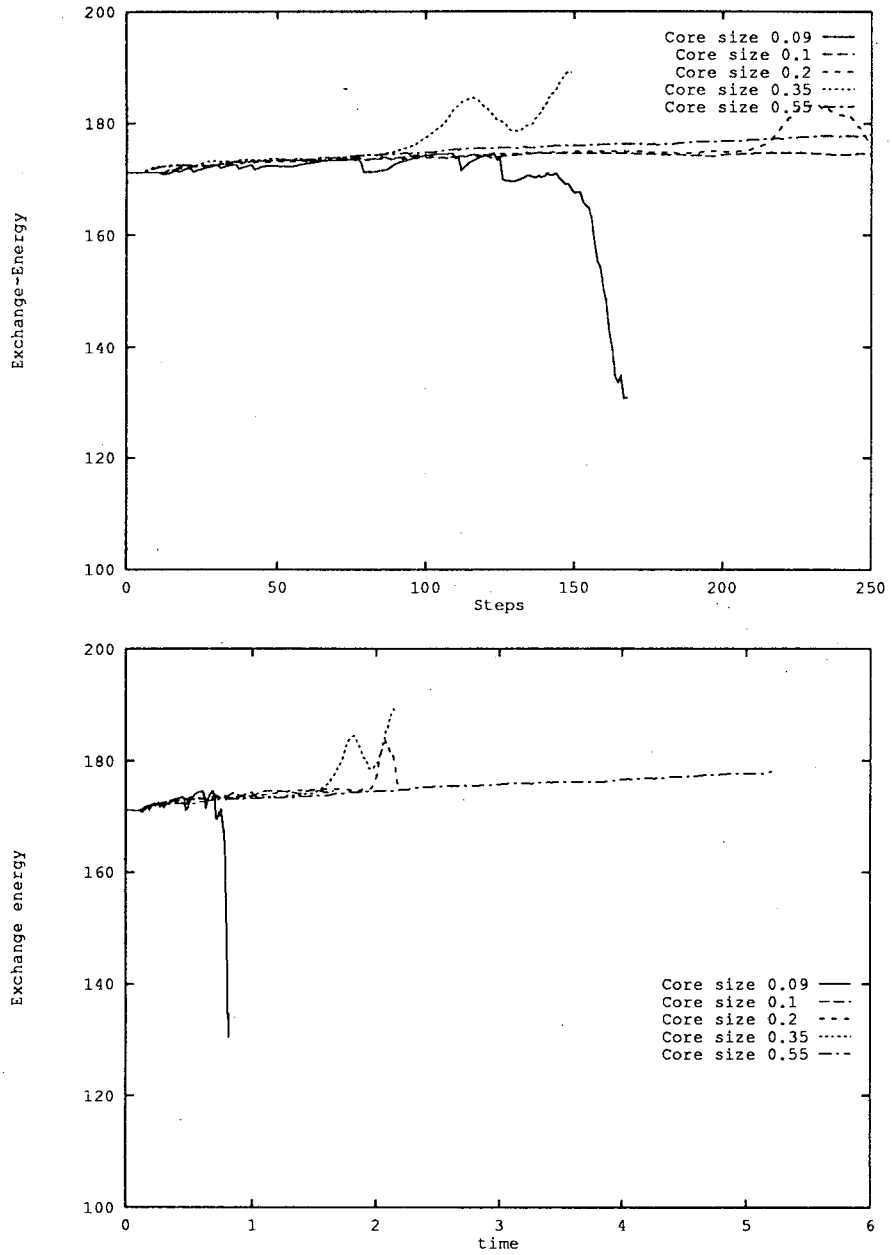

Figure 6.9. Plot of the total kinetic energies corresponding to 5 core sizes.

to a one-arm structure at a core size of around 0.2. For a core size equal to 0.1, we see a wave splitting from the original wave and propagating with a stable shape; this split wave has a longer wave length than the one seen in the case with a core size of 0.55. With a core size of 0.09 or smaller, the stretching starts at two truncated ends, then gradually affects the middle. We think that this may be caused by truncation error. However, the original solitary wave propagates with a better preserved shape and phase speed. These descriptions of the geometric structure and evolution of a wave propagating on one filament as a function of core size also apply to runs with core function 1 (Table 6.5) and to the simulation with three filaments (Table 6.6). For the simulation with a single filament, the one-arm structure appears whenever the stretching happens near the original wave and the core size is less than or equal to 0.15. For the simulation with three filaments, if an arm grows far from the center, it may spread along the filaments in the direction opposite to the direction of wave propagation. The physical explanation of this phenomenon is that for stretching, the near center part moves with a speed higher than the part far from the center in the x-direction because the induced velocity is smaller far from the center.

In Figure 6.9, we plot the total kinetic energies corresponding to the same five core sizes in Table 6.5, with core function 4. Figure 6.9 shows that the total kinetic energy is well conserved for various core sizes as long as there is no violent stretching. Figure 6.9 shows the nonmonotonical response of numerical results to core sizes. The result with core size 0.09 is physically unacceptable because the wide variation of kinetic energy. The total vorticity is well conserved.

Some authors vary core size in their version of vortex methods (see Leonard [54, 55], Siggia [66], Winckelmans [72], and Chorin [25]). We have examined this treatment of the core. The results produced by varying the core size are always worse than the results produced by constant core size; namely, the violent stretching always happens in fewer computational steps for a run made with varying core size.

Table 6.7. The total number of computational steps, the total number of segments at the last computational step, the total arclength at the last computational step, and the elapsed time for increasing wave torsion τ of initial data.

core function 4, $\Gamma = 5.0$, $C = 0.05$, $t_0 = -0.2$, the 4th order Runge-Kutta method, distance between filaments = 0.05, and periodic treatment at truncated ends

τ	one filament				four filaments			
	Step	At the Last Step			Step	At the Last Step		
		No. Seg.	Time	Arclength		No. Seg.	Time	Arclength
6.0	300	670	6.0000	16.15896	300	1950	0.75000	64.77505
5.0	300	647	6.0000	16.22601	300	1955	0.73125	64.38577
4.5	300	647	3.3400	17.03079	300	2605	0.60250	83.75597
4.0	234	988	2.4300	33.53885	300	2749	0.49125	92.79603
3.0	259	989	2.2200	34.90552	300	2335	0.39375	80.63711
2.5	300	512	2.6800	16.30441	300	2047	0.38625	70.28714
2.0	300	456	3.0000	16.23470	300	1860	0.38125	64.67449
1.0	90	968	0.5750	34.41537	118	3849	0.14750	136.68418
0.5	77	990	0.3925	34.96001	72	3677	0.09000	130.69027
0.0	67	992	0.2425	35.26452	70	3490	0.05313	125.24485

6.5 The Torsion τ in the Initial Solitary Wave and Vortex Stretching

The torsion τ of initial solitary wave is clearly a physical factor. We have mentioned at page 29, Chapter 3 that increasing $|\tau|$ will increase the speed and decrease the amplitude of the initial solitary wave. Geometrically, with smaller τ, a given curve will be closer to a plane curve. When $\tau = 0$, the given curve lies in a plane (see Spivak [67, p. 38]). In our computations, we find that vortex stretching always starts at a part of a wave whose curve is almost a plane curve; i.e., the curve has a small torsion. We consider this observation in this section and attempt to give an explanation.

Using Hasimoto's solitary wave as initial datum determined by the torsion τ and the curvature, we wish to see the effects of varying τ on the vortex stretching. The results are displayed in Table 6.7, which ahows that vortex line stretching does not respond to the initial wave torsion τ monotonically. However, if τ is small enough, for example, in Table 6.7 if $\tau \leq 1.0$, the vortex stretching does occur directly on the initial solitary wave, whereas if $\tau > 1.0$, the stretching only occurs if there is a new wave with small torsion produced from the original solitary wave. Thus we think that a perturbation wave with small torsion on a vortex tube may be one of most important causes of vortex tube stretching.

In Figure 6.10, we plot the y-z coordinate plane slice of the velocity distribution induced by initial solitary wave data with various torsions τ (the slice is taken where the wave amplitude is maximum). We can see that if τ is small the velocity will be distributed less evenly on the slice through the peak of the wave. However, such uneven velocity distributions on the slices do not necessarily cause vortex line stretching. This can be seen in Figure 6.10 and Table 6.7. In Figure 6.10, for $\tau = 2.0$, on the y-z coordinate plane slice through the wave peak, we have an uneven velocity distribution, whereas in Table 6.7 the corresponding computation shows no significant stretching.

In Figure 6.11, we plot the x-z plane slice (i.e., the plane in three-dimensional space with $y = 0$) of the velocity distribution induced by initial solitary wave data with various values of τ. In the cases $\tau = 2.0$ and $\tau = 4.0$, the horizontal component (i.e., x-component) of the velocity distribution on the whole wave points in the same direction, whereas in the case $\tau = 1.0$, the sign of the horizontal component of velocity at and near the peak changes, which causes stretching because the vortex filaments are bent at the middle of the wave. For the case $\tau = 0$, the velocity distribution on the x-z plane is symmetric, with the line of symmetry passing through the peak of the wave. On the line of symmetry, the velocity is vertical, which can be considered as a discontinuity of the horizontal component of the velocity field. Such a discontinuity causes violent stretching.

We now consider the stretching that happens after the initial wave propagates for a while along a vortex tube. In Figure 6.12 we plot the x-z plane slices of

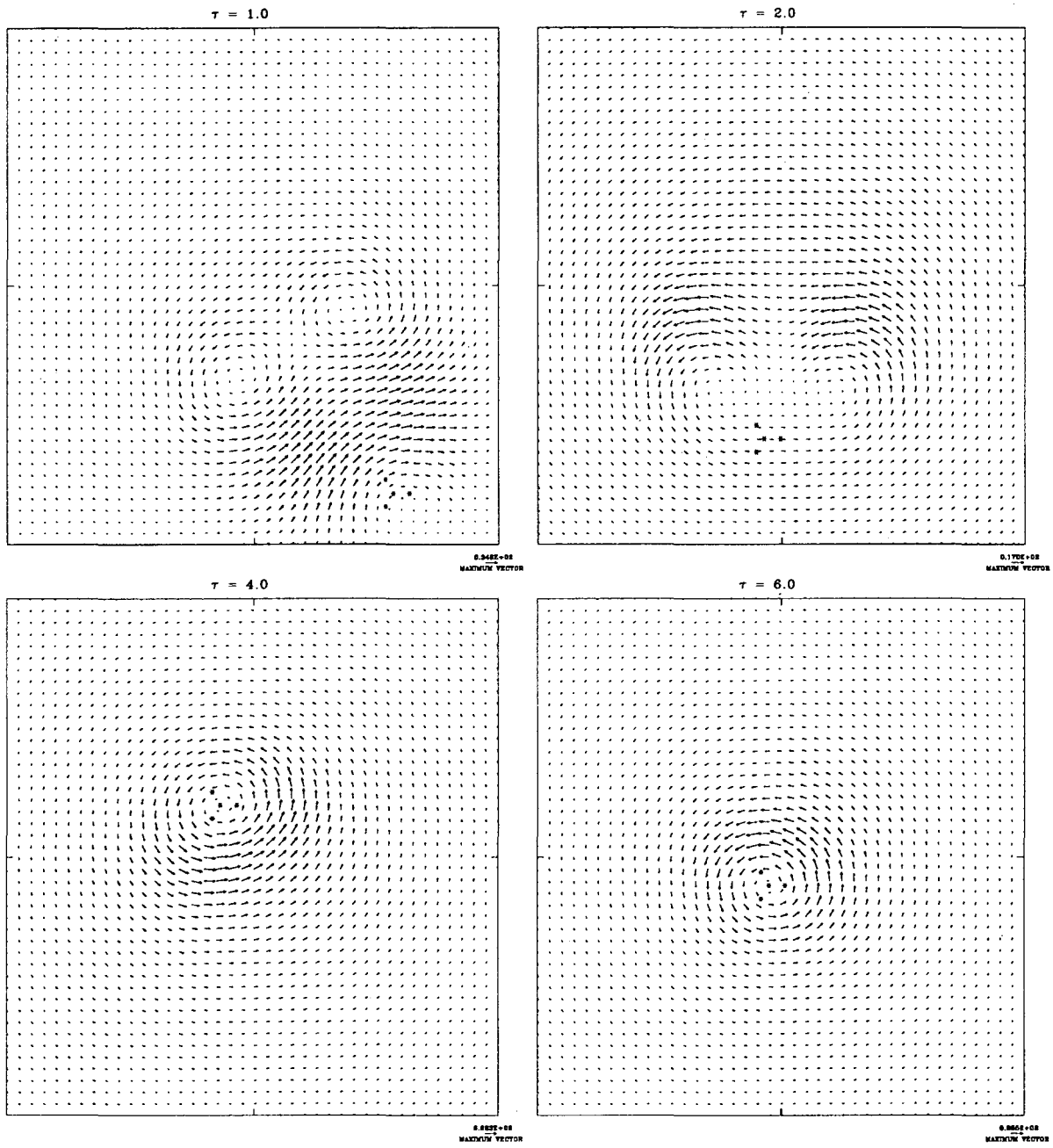

Figure 6.10. The y-z plane slice of velocity distribution induced by initial solitary wave data with various torsions τ. The slice is taken at the peak wave amplitude.

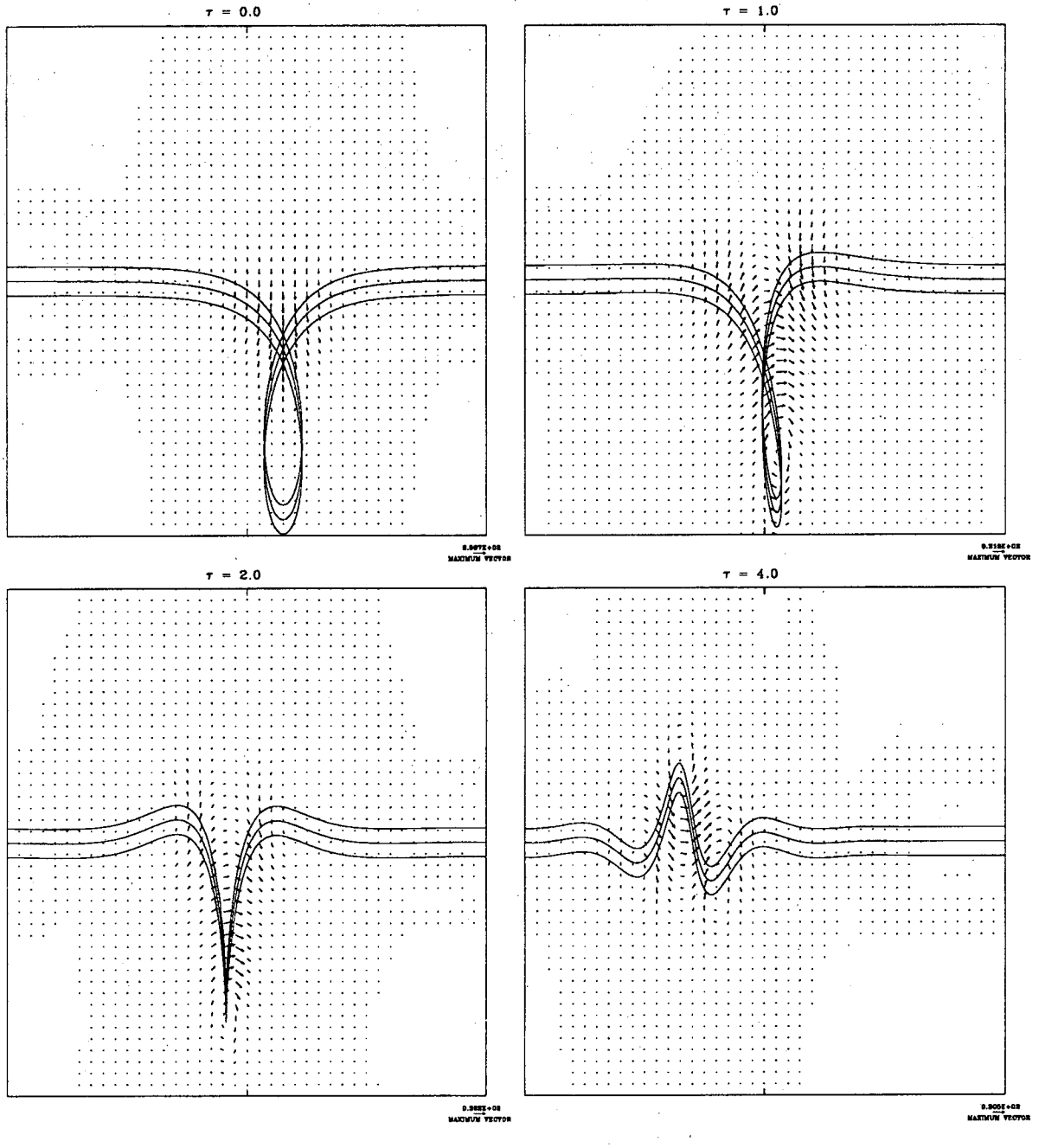

Figure 6.11. The $y = 0$ slice of velocity distribution induced by initial solitary wave data with various torsions τ.

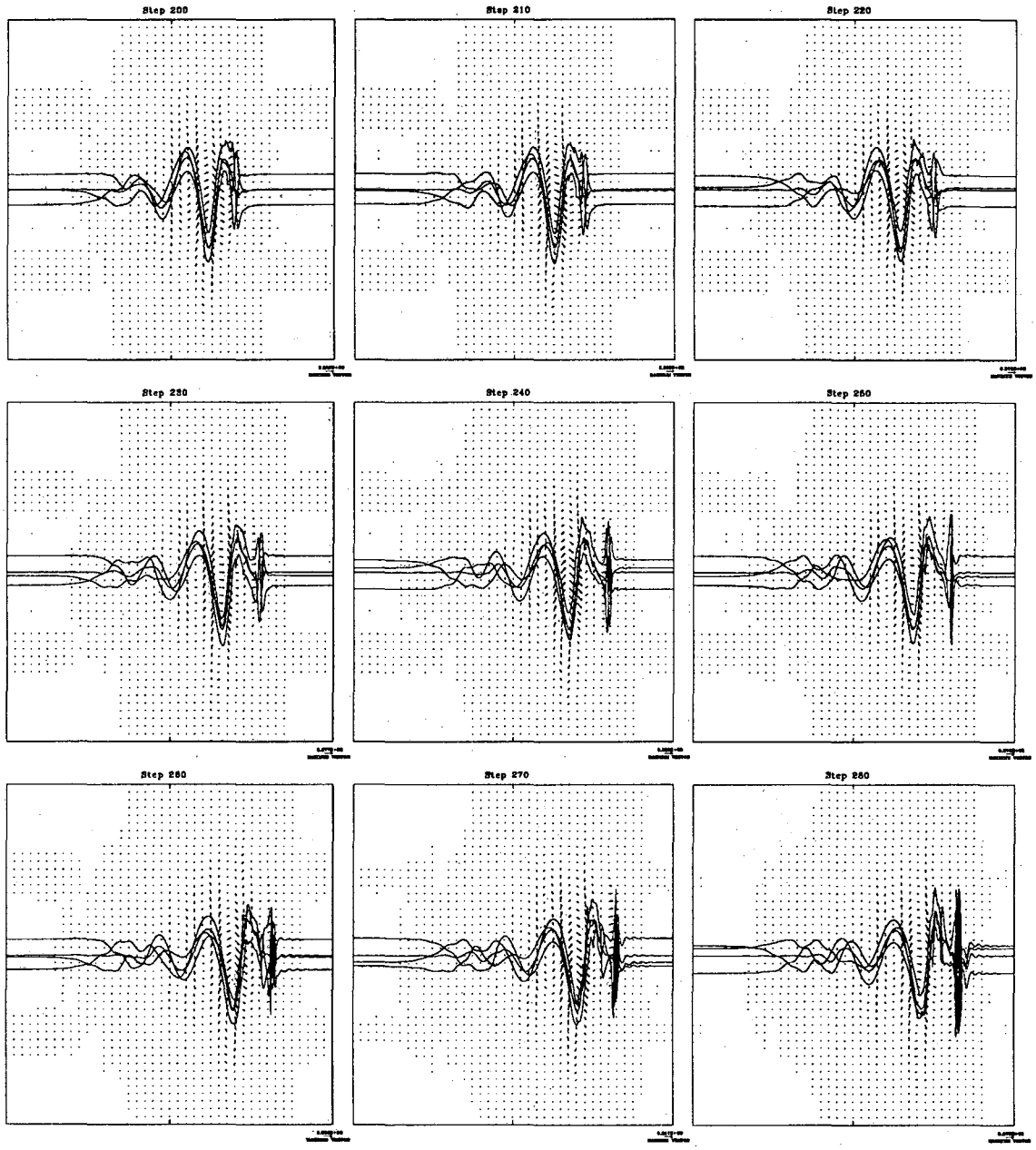

Figure 6.12. The $y = 0$ slice of velocity distribution induced by initial solitary wave data with torsion $\tau = 4.0$.

the velocity distribution for $\tau = 4.0$ at computational steps from 200 to 280, which illustrates the process of vortex stretching. One can see that from step 200 to step 240 the discontinuity of x-component velocity is developed at the right front of the wave, which has small torsion (on our two-dimensional projection pictures, this can be seen as a vertical or nearly vertical line). The stretching happens where an x-component velocity discontinuity is present. The figure clearly shows that the particles at the left side of the discontinuity move with much greater speed than the particles at the right side of the discontinuity; thus, the particles from the left side of the discontinuity will accumulate at the discontinuity. This accumulation of particles will increase the velocity in the y- and z-components and cause stretching.

We have also observed that, when stretching happens, there will be some vortex segments right on or over the maximum velocity region on the y-z plane. It is clear that once some vortex segments pass over the maximum velocity region on the y-z plane, the vortex lines will bend and stretch in the peak velocity area in the y-z plane, and form so-called "hairpin" or horseshoe structures because points at and near the velocity peak move faster than other points. These structures, of course, will change the local velocity distribution and cause more stretching. To illustrate our observation, in Figure 6.13, we plot the velocity distribution on the y-z plane at where the vortex lines stretches for step 230, 250, 280, and 300 with $\tau = 4.0$ for initial data. Figure 6.14 shows the two-dimensional projection views and three-dimensional perspective view at these computational steps. After the stretching starts, the analysis of the velocity distribution inside the stretching area can not provide too much information for studying the evolution of the stretching structure. One may need other physical tools such as statistical mechanics to understand the further developments of the vortex stretching (see Chorin [26]).

6.6 Summary and Discussion

We have investigated nine factors listed in the first section of this chapter. Most questions we posed at the beginning of this chapter have been answered at this point. We summarize these answers here.

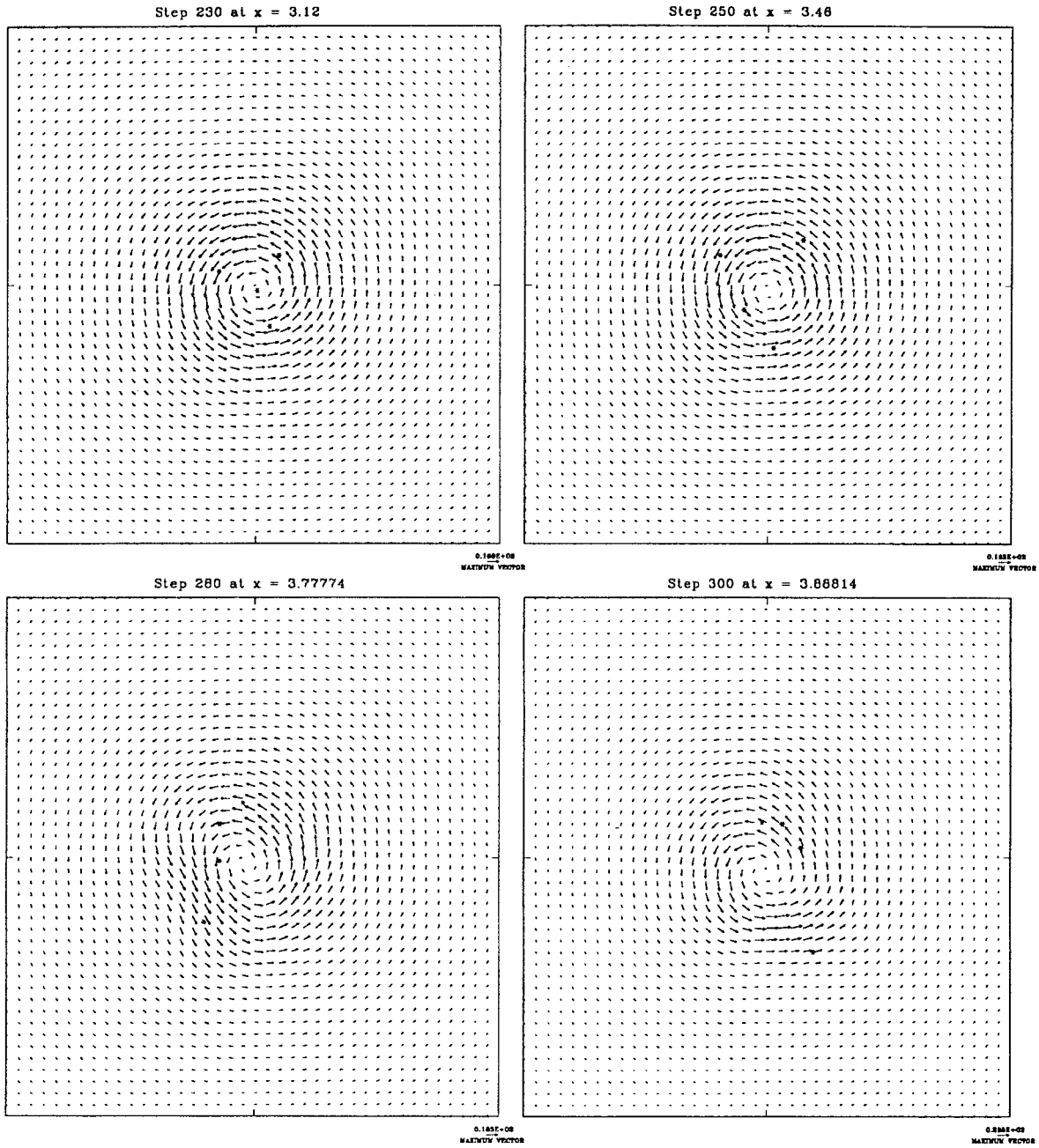

Figure 6.13. The y-z plane slice of velocity distribution induced by wave initially with torsion $\tau = 4.0$ where the vortex lines stretches.

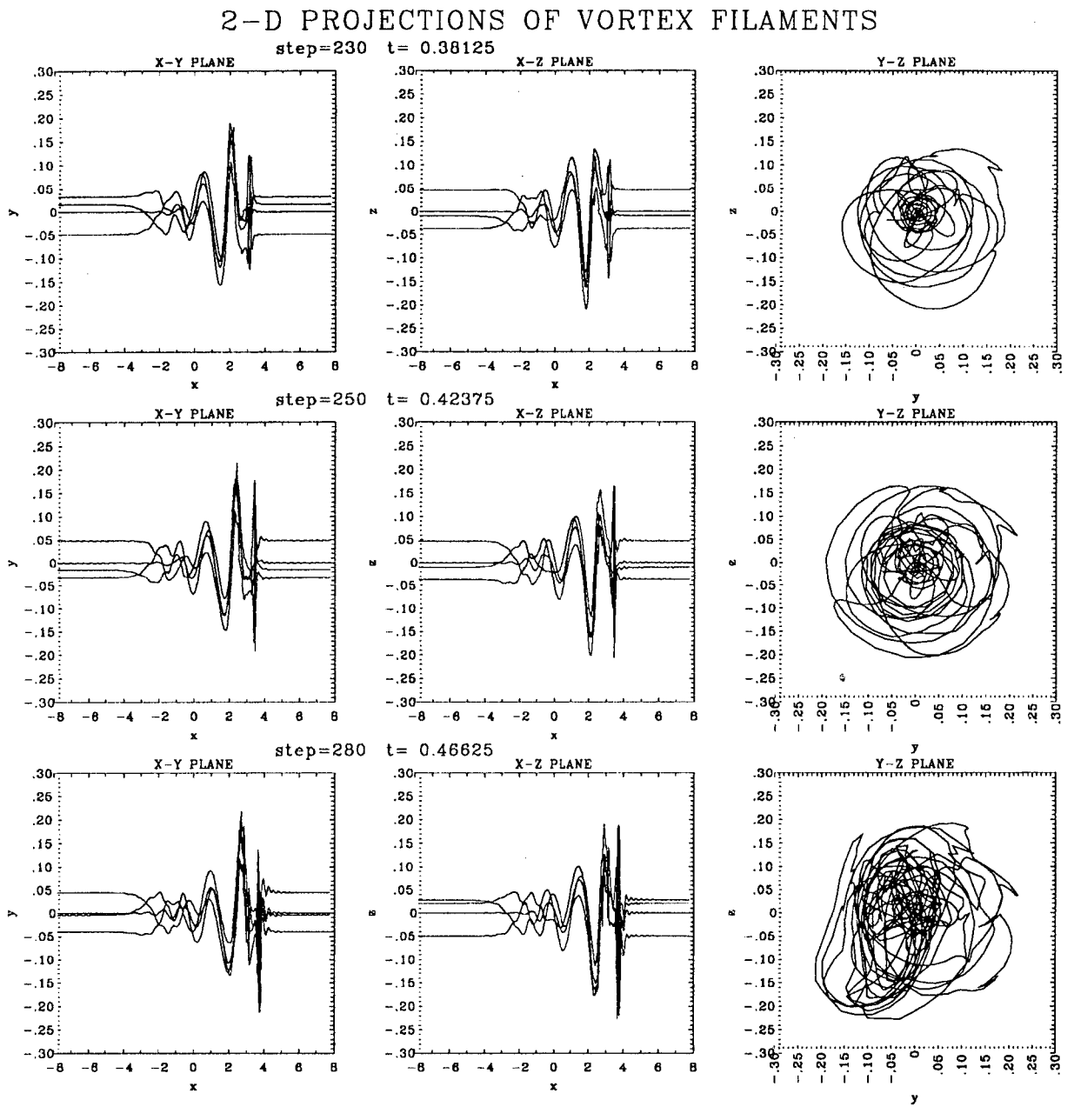
2-D PROJECTIONS OF VORTEX FILAMENTS
step=230 t= 0.38125
X-Y PLANE
X-Z PLANE
Y-Z PLANE
step=250 t= 0.42375
X-Y PLANE
X-Z PLANE
Y-Z PLANE
step=280 t= 0.46625
X-Y PLANE
X-Z PLANE
Y-Z PLANE

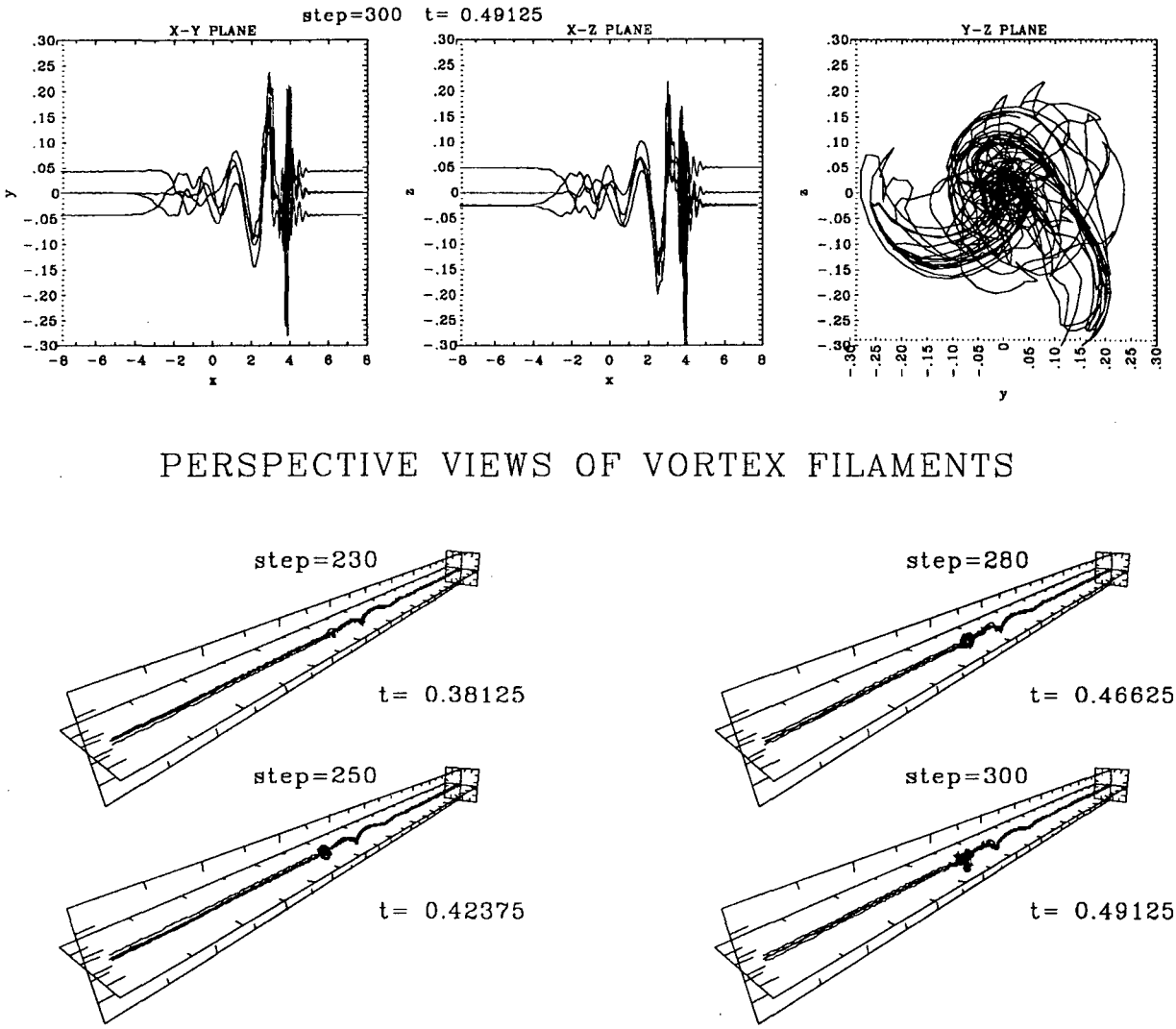

Figure 6.14. Two- and three-dimensional views of computation results for $\tau = 4.0$ at steps 230, 250, 280, and 300 as examples of vortex lines stretching.

A. In our study, the higher-order numerical methods used to solve the time evolution ordinary differential equation generally give us more accurate results. The vortex tube simulation becomes more accurate as the number of filaments increases. The time tolerance control constant C is important to obtain an accurate result. Generally speaking, the smaller C we use, the higher accuracy we obtain, but the computation become more expensive. The choice of C depends on the circulation Γ. The core function is core size dependent. Core sizes too big or too small give inaccurate results. With core size in a reasonable range, the vortex filaments behave differently for different choice of core sizes. With this information, for each numerical experiment, we can choose those parameters properly to avoid inaccuracy in our computation.

B. Core size and wave torsion are the two most sensitive factors in studying vortex stretching. We believe that a small torsion of a wave will cause a near discontinuity on the velocity component in the direction of wave propagation. This near discontinuity causes the violent stretching of the vortex tube.

Question C is equivalent to the question of whether a discontinuity in a certain velocity component must occur in the evolution of a vortex tube. We have not obtained enough evidence to answer this question fully. However, with periodic data, we observed that, with certain initial solitary wave data and proper choice of parameters, some wave shapes persist in the periodic computing box. This phenomenon, reported elsewhere (see Samuel and Donnelly [62]), indicates that a solitary wave can propagate along a vortex tube for a long time; otherwise, the shape should be destroyed soon after passing the boundary of the periodic computing box because of the nonsmooth connection at the boundaries. Research on this subject without a periodic assumption is in progress.

Chapter 7

Conclusions

We have presented three-dimensional vortex methods for unsteady, inviscid, incompressible flow. We have investigated the effects of various numerical parameters, core functions and numerical methods for solving the time evolution ordinary differential equation on the accuracy of the numerical scheme. Vortex stretching phenomena have been studied. We reviewed the localized induction approximation and its solitary wave solution. We have also studied some diagnostics such as conservation of energy, total vorticity, and linear impulse for our vortex filament scheme.

We have reviewed the localized induction approximation and given the detailed derivation. We have proved the equivalence of the Betchov intrinsic equations and the nonlinear Schrödinger equation. By solving the Betchov intrinsic equations under the assumption that torsion τ is constant, we obtained the same solution for curvature κ as Hasimoto [44]. Then, following a method introduced by Hasimoto [44], we translated the intrinsic solution to the solution in the Cartesian coordinate system. The resulting wave is a solitary wave, as first found by Hasimoto [44].

In the study of diagnostics, we have given the detailed derivation of numerical schemes for computing kinetic energy, total vorticity, and linear impulse. We have also studied the scaling property of energy conservation, and given some asymptotical properties of energy scaling formulation in a small cylindrical vortex segment. We have found that these diagnostics may not be suitable for the computation of part of a vortex tube because those quantities may not be conserved in the part.

To simulate a finite part of an infinitly long vortex tube, we must deal with two truncated ends. We have treated the truncated ends using two methods: a periodic extension of the data and an smooth extension of the ends by straight lines. The choice of method depends on the problem.

In the study of the effects of numerical parameters, core functions and numerical methods for solving the time evolution ordinary differential equation on accuracy, we have found that to obtain accurate results, the time tolerance control constant C must be chosen smaller than a certain bound, which can only be determined after other parameters are given; the circulation Γ is the most important parameter for the choice of C. The choice of core function has an effect on the accuracy of the computation, but the accuracy can be improved for each core function by adjusting other parameters, especially the core size. We have tested three numerical methods for solving the time evolution ordinary differential equation: the first-order Euler method, the second-order modified trapezoidal method, and the fourth-order Runge–Kutta method. The accuracy of computation increases as the order increases. There is significant improvement in the accuracy from the first-order method to the second-order method, but not much improvement from the second-order method to the fourth-order method. We found that vortex stretching and accuracy of computation are sensitive to core size. The stretching behavior of our results does not respond to the core size monotonically. However, it is generally true that too small a core size generates high-frequency perturbation waves at places far from the given initial perturbation wave. Such high-frequency perturbation waves most likely represent the computational error, and too large a core size gives us an inaccurate approximation of the singular kernel.

The simulation of a large diameter vortex tube by several filaments is natural. We believe that the computation will be more accurate with more filaments simulating a vortex tube. This conjecture comes from the observation that, even with straight filaments, the stretching may still occur on the plane perpendicular to the straight filaments, thus, more filaments will surely provide more detail of the stretching on that plane and make the simulation, especially the core structure, more accurate. The distance between filaments is important for obtaining accurate simula-

tions with several filaments. The computation is more accurate with filaments closer together, but the number of filaments must be increased to match the diameter of the simulated vortex tube; otherwise, for a fixed number of filaments, the computation results will be closer to the results from a one filament simulation. We should mention that with many filaments, we can simulate not only a large diameter vortex but also shear flows and tubes with noncircular vortex core structures.

We have studied the beginning stage of vortex tube stretching and have seen that violent stretching mostly occurs and remains in a plane perpendicular to the vortex lines. It appears that a small torsion of a perturbation wave is an important cause of vortex tube stretching. When stretching happens, there are always some points reaching the maximum velocity on a cross plane, which causes the formation of "hairpin" structures. Is there a properly constructed perturbation wave that can travel along a vortex tube simulated by vortex filaments without violent stretching? This question is associated with the question of whether a solitary wave can survive on a vortex tube for a long time, which remains open. But, with certain periodic data and properly chosen combinations of parameters, we have seen certain wave shapes persist in the periodic computing box.

Bibliography

[1] C. Anderson and C. Greengard. On vortex methods. *SIAM J. Numer. Anal.*, 22:413, 1984.

[2] H. Aref and E.P. Flinchem. Dynamics of a vortex in a shear flow. *J. Fluid Mech.*, 148:477–497, 1984.

[3] R.J. Arms and F.R. Hama. Localized-induction concept on a curved vortex and motion of an elliptic vortex ring. *Phys. Fluids*, 8:553–59, 1965.

[4] G.K. Batchelor. *An Introduction to Fluid Dynamics.* Cambridge University Press, 1967.

[5] J.T. Beale. A convergent 3-d vortex method with grid-free stretching. *Math. Comput.*, 46(174):401–424, 1986.

[6] J.T. Beale. On the accuracy of vortex methods at large times. In *Proceedings of the Workshop on Computational Fluid Dynamics and Reacting Flows, I.M.A.* University of Minnesota, 1986.

[7] J.T. Beale and A. Majda. Rates of convergence for viscous splitting of the Navier-Stokes equations. *Math. Comput.*, 37:243–59, 1981.

[8] J:T. Beale and A. Majda. Vortex methods, I: convergence in three dimensions. *Math. Comput.*, 39:1–27, 1982.

[9] J.T. Beale and A. Majda. Vortex methods, II: higher order accuracy in two and three dimensions. *Math. Comput.*, 39:29–52, 1982.

[10] J.T. Beale and A. Majda. High order accurate vortex methods with explicit velocity kernels. *J. Comput. Math. Phys.*, 58:188–208, 1985.

[11] R. Betchov. On the curvature and torsion of an isolated vortex filamnet. *J. Fluid Mech.*, 22:471–479, 1965.

[12] T.F. Buttke. A numerical study of superfluid turbulence in the Self-Induction Approximation. *J. Comput. Math. Phys.*, 76:301–326, 1988.

[13] A.J. Callegari and L. Ting. Motion of a curved vortex filament with decaying vortical core and axial velocity. *SIAM J. Appl. Math.*, 35(1):148–175, 1978.

[14] C. Chang. Random vortex methods for the Navier-Stokes equations. *J. Comp. Phys.*, 76:281–300, 1988.

[15] A.J. Chorin. Vortex models and boundary layer instability. *SIAM Sci. Stat. Comput.*, 1(1):1–24, 1980.

[16] A.J. Chorin. Estimates of intermittency, spectra, and blow-up in developed turbulence. *Commun. Pure Appl. Math.*, 34:853–866, 1981.

[17] A.J. Chorin. The evolution of a turbulent vortex. *Commun. Math. Phys.*, 83:517–535, 1982.

[18] A.J. Chorin. Turbulence and vortex stretching on a lattice. *Commun. Pure Appl. Math.*, 39:S47–S65, 1986.

[19] A.J. Chorin. Lattice vortex models and turbulence. In A. Chorin and A. J. Majda, editors, *Wave motion: theory, modelling, and computation—Proceedings of a conference in honor of the 60th birthday of Peter D. Lax.* Springer-Verlag, 1987.

[20] A.J. Chorin. Scaling laws in the vortex lattice model of turbulence. *Commun. Math. Phys.*, 114:167–176, 1988.

[21] A.J. Chorin. Spectrum, dimension, and polymer analogies in fluid turbulence. *Phys. Rev. Lett.*, 60(19):1947–1949, 1988.

[22] A.J. Chorin. Vortex stretching and the small-scale structure of turbulence. In C. Anderson and C. Greengard, editors, *Vortex Methods*, pages 37–41. Springer-Verlag, 1988.

[23] A.J. Chorin. Vortices, turbulence, and statistical mechanics. In K. Gustafson and J. Sethian, editors, *Vortex Methods*. SIAM publication, 1989.

[24] A.J. Chorin. Constrained random walks and vortex filaments in turbulence theory. *Comm. Math. Phys.*, 132:519–536, 1990.

[25] A.J. Chorin. Hairpin removal in vortex interactions. *J. Comp. Phys.*, 91:1–21, 1990.

[26] A.J. Chorin. Statistical mechanics and vortex motion. In *Vortex Dynamics and Vortex Methods—Proceedings of a conference 1990 AMS-SIAM Summer Seminar*. AMS, 1990.

[27] A.J. Chorin and J. Marsden. *A Mathematical Introduction to Fluid mechanics*. Springer, 1979.

[28] V. del Prete. Numerical simulation of vortex breakdown. LBL report LBL-8503, Lawrence Berkeley Laboratory, 1978.

[29] A. F. Ghoniem and Y. Cagnon. Vortex simulation of laminar recirculating flow. *J. Comp. Phys.*, 68:346–377, 1987.

[30] A. F. Ghoniem, D. Y. Chen, and A. K. Oppenheim. Formation and inflammation of a turbulent jet. *AIAA Journal*, 24(2):224–229, 1986.

[31] A. F. Ghoniem, A. J. Chorin, and A. K. Oppenheim. Numerical modeling of turbulent flow in a combustion tunnel. *Philos. Trans. Roy. Soc. Lond. A.*, 304:303–325, 1982.

[32] A. F. Ghoniem and P. Givi. Lagrangian simulation of a reacting mixing layer at low heat release. *AIAA Journal*, 26:690–697, 1986.

[33] A. F. Ghoniem and J. A. Sethian. Effect of Reynolds number on the structure of recirculating flow. *AIAA Journal*, 25:168–171, 1987.

[34] J. Goodman. Convergence of the random vortex method. *Comm. Pure. Appl. Math.*, 60:189–220, 1987.

[35] C. Greengard. Convergence of the vortex filament method. *Math. Comput.*, 47:387–98, 1986.

[36] O.H. Hald. Private communication.

[37] O.H. Hald. Convergence of vortex methods for Euler's equations, II. *SIAM J. Numer. Anal.*, 16(5):727–55, 1979.

[38] O.H. Hald. Convergence of random methods for a reaction-diffusion equation. *SIAM J. Sci. Stat. Comput.*, 2:85–94, 1981.

[39] O.H. Hald. Convergence of random methods with creation of vorticity. *SIAM J. Sci. Stat. Comput.*, 7:1373–1386, 1986.

[40] O.H. Hald. Convergence of vortex methods for Euler's equations, III. *SIAM J. Numer. Anal.*, 24(3):538–82, 1987.

[41] O.H. Hald and V.M. del Prete. Convergence of vortex methods for Euler's equations. *Math. Comp.*, 32:791–809, 1978.

[42] F.R. Hama. Progressive deformation of a curved vortex filament by its own induction. *Phys. Fluids*, 5(10):1156–62, 1962.

[43] F.R. Hama. Progressive deformation of a perturbed line vortex filament. *Phys. Fluids*, 6(4):526–34, 1962.

[44] H. Hasimoto. A soliton on a vortex filament. *J. Fluid Mech.*, 51(3):387–98, 1972.

[45] O. Inoue. Vortex simulation of turbulent mixing layer. *AIAA J.*, 23(3):367–73, 1985.

[46] O. Inoue and A. Leonard. Vortex simulation of forced/unforced mixing layer. *AIAA J.*, 25:1417–1418, 1987.

[47] Lord Kelvin. Vibrations of a columnar vortex. *Phil. Mag.*, 10:155–68, 1880.

[48] R. Klein and A.J. Majda. Self-stretching of a perturbed vortex filament I: the asymptotic equation for deviations from a straight line. Submitted to Physica D, February 1990.

[49] O.M. Knio and A.F. Ghoniem. Numerical study of a three-dimensional vortex method. *J. Comput. Math. Phys.*, 86:75–106, 1988.

[50] Robert Krasny. Desingularization of periodic vortex sheet roll-up. *J. Comput. Phys.*, 65:292–313, 1986.

[51] G.L. Lamb, Jr. *Elements of Soliton Theory.* John Wiley and Sons, 1980.

[52] H. Lamb. *Hydrodynamics.* Cambridge University Press, 6th ed., Reading, Massachusetts, 1932.

[53] S. Leibovich and H.Y. Ma. Soliton propagation on vortex cores and the Hasimoto soliton. *Phys. Fluids*, 26(3):3173–79, 1983.

[54] A. Leonard. Vortex method for flow simulation. *J. Comput. Phys.*, 37:289–335, 1980.

[55] A. Leonard. Computing three-dimensional incompressible flow with vortex elements. *Ann. Rev. Fluid Mech.*, 17:523–59, 1985.

[56] J.C. Neu. The dynamics of a columnar vortex in an imposed strain. *Phys. Fluids*, 27:2397–2402, 1984.

[57] J.C. Neu. The dynamics of stretched vortics. *J. Fluid Mech.*, 143:253–276, 1984.

[58] M. Perlman. On accuracy of vortex methods. *J. Comput. Phys.*, 59:200–223, 1985.

[59] D. I. Pullin and P. A. Jacobs. Inviscid envolution of stretched vortex arrays. *J. Fluid Mech.*, 171:377–406, 1986.

[60] S. Roberts. Accuracy of the random vortex method for a problem with non-smooth initial conditions. *J. Comput. Phys.*, 58:29–43, 1985.

[61] Walter Rudin. *Functional Analysis.* McGraw-Hill Book Company, 1973.

[62] D. C. Samuel and R. J. Donnelly. Sideband instability and recurrence of Kelvin waves on vortex cores. *Phys. Rev. Lett.*, 64(12):1385–1388, 1990.

[63] J. Sethian. Turbulent combustion in open and closed vessels. *J. Comput. Phys.*, 54:425–56, 1984.

[64] J. Sethian. On measuring the accuracy of vortex method: using a radom method to model stable and unstable flow. In C. Anderson and C. Greengard, editors, *Vortex Methods*, pages 83–95. Springer-Verlag, 1988.

[65] J. Sethian and A. F. Ghoniem. Validation study of vortex methods. *J. Comput. Phys.*, 74:283–317, 1988.

[66] E.D. Siggia. Collapse and amplification of a vortex filament. *Phys. Fluids*, 28(3):794–805, 1985.

[67] M. Spivak. *Differential geometry*, volume 2. Publish or Perish, Inc., 1979.

[68] J. Stoer and R. Bulirsch. *Introduction to numerical analysis.* Springer-Verlag, 1980.

[69] S. E. Widnall. The structure and dynamics of vortex filament. *Ann. Rev. Fluid Mech.*, 7:141–165, 1975.

[70] S. E. Widnall, D. B. Bliss, and A. Zalay. Theoretical and experimental study of the stability of a vortex pair. In *Aircraft wake turbulence and its detection*, page 305. Plenum, 1971.

[71] S. E. Widnall and C.-Y. Tsai. The instability of the thin vortex ring of constant vorticity. *Philos. Trans. Roy Soc. London Ser A*, 287:273–305, 1977.

[72] G.S. Winckelmans. *Topics in vortex methods for the computation of three- and two-dimensional incompressible unsteady flows.* PhD thesis, California Institute of Technology, 1989.

LAWRENCE BERKELEY LABORATORY
UNIVERSITY OF CALIFORNIA
INFORMATION RESOURCES DEPARTMENT
BERKELEY, CALIFORNIA 94720